Setup and proof-of-concept of a test stand for High Purity Germanium spectroscopy detectors

Dissertation

der Mathematisch-Naturwissenschaftlichen Fakultät

der Eberhard Karls Universität Tübingen

zur Erlangung des Grades eines

Doktors der Naturwissenschaften

(Dr. rer. nat.)

vorgelegt von

Lukas Ulrich Rauscher

aus Münsingen

Tübingen

2023

Gedruckt mit Genehmigung der Mathematisch-Naturwissenschaftlichen Fakultät der Eberhard Karls Universität Tübingen.

Tag der mündlichen Qualifikation:	17.11.2023
Dekan:	Prof. Dr. Thilo Stehle
1. Berichterstatter/in	Prof. Dr. Josef Jochum
2. Berichterstatter/in	Prof. Dr. Tobias Lachenmaier

Abstract

Background reduction is crucial for low background experiments as for example those searching for the neutrinoless double beta decay like the Large Enriched Germanium Experiment for Neutrinoless Double Beta Decay (LEGEND). A successful technique for background reduction is pulse shape discrimination, which can discriminate different kinds of radiation and therefore assort unwanted events. The events are categorized in desired single-site events (SSE) and unwanted multi-site events (MSE). This technique relies on a good understanding of how the pulse shapes are formed. A good proxy for SSEs in LEGEND is the double escape event from a γ ray with 2614.5 keV due to the decay of ^{208}Tl. Such an event starts with pair production inside of the detector. The electron causes an energy deposition of 1592 keV in the detector and the positron annihilates with another electron into two γ rays with energies of 511 keV. If both these γ rays leave the detector, a double escape event occurs and the electron is the only energy deposition in the detector. The energy deposition inside of the detector happens in a small volume due to the very short reach of the electron. This thesis covers the setup and use of a test stand to measure pulse shapes as a function of interaction region for such double escape events. This may lead to a better understanding of the pulse shapes and therefore a new kind of pulse shape discrimination in the future. Most importantly existing pulse shape simulations can be verified. For further background reduction this thesis also covers part of the commissioning of the Cherenkov muon veto for LEGEND-200.

Zusammenfassung

Eine Reduktion der natürlichen Hintergrundstrahlung ist notwendig für jedes Experiment auf der Suche nach seltenen Ereignissen, z.B. die Suche nach dem neutrinolosen doppelten Betazerfall wie es das Large Enriched Germanium Experiment for Neutrinoless Double Beta Decay (LEGEND) tut. Eine erfolgreiche Technik zur Reduktion der Hintergrundstrahlung ist die Pulsform-Diskrimination die verschiedene Arten von Strahlung unterscheiden und damit unerwünschte Ereignisse aussortieren kann. Ereignisse werden dabei in relevante Single Site Events (SSE) und irrelevante Multi Site Events (MSE) klassifiziert. Diese Technik basiert auf einem sehr guten Verständnis wie die Pulse im Detektor zustandekommen. Ein guter Vertreter der SSEs in LEGEND ist das Doppel-Austrittsereignis nach Paarbildung durch ein γ-Quant von z.B. der 2614 MeV γ Linie von ^{232}Th. Ein derartiges Ereignis beginnt mit Paarbildung im Detektor. Das Elektron und das Positron deponieren ihre kinetische Energie von gesamt 1592 keV im Detektor und anschließend annihiliert das Positron mit einem Elektron des Detektors. Dabei werden zwei γ Quanten mit einer Energie von jeweils 511 keV produziert, die entgegengesetzt voneinander emittiert werden. Verlassen beide Quanten den Detektor ohne Wechselwirkung, besteht das Signal im Detektor nur aus der Energiedeposition von Elektron und Positron in einem kleinen räumlichen Volumen. Eine solche Signatur hätte auch ein neutrinoloser doppelter Betazerfall. Diese Arbeit behandelt den Aufbau und Test eines Teststandes um das Interaktionsvolumen und die Pulsform solcher Doppel-Austrittsereignisse zu messen. Dies führt idealerweise zu einem besseren Verständnis der Pulsformen und damit vielleicht zu neuartigen Formen der Pulsform-Diskrimination. Insbesondere können damit bestehende Pulsform-Simulationen verifiziert werden. Zur weiteren Reduktion der natürlichen Hintergrundstrahlung behandelt diese Arbeit auch einen Teil der Inbetriebnahme des Cherenkov-Myon-Vetos für LEGEND-200.

Contents

List of Figures

List of Tables

1

Introduction

"The beginning is the most important part of the work."

- Plato, *Greek philosopher*

This work was carried out in order to measure the pulse shapes of energy depositions in High Purity Germanium (HPGe) detectors depending on the location of the deposition. In order to realize that the HPGe detector is irradiated by a collimated γ source and the events with pair production selected. The positron produced in the case of pair production thermalizes quickly with a short path (on the order of μm) inside of the detector and then annihilates with an electron present in the detector. The electron deposits its energy inside the HPGe detector and creates a pulse at its readout electronics. The γs emerging from the annihilation can be detected by a positron emission tomography (PET) scanner placed around the HPGe detector. Depending on the measurement interest (proof-of-principle vs. characterisation) the γ source is either non-collimated or collimated respectively. For the non-collimated measurements the PET scanner is

used in its γ escape mode and one can achieve a density map of the HPGe detector, since the reaction cross-section depends on the number of atomic nuclei and therefore the density of the material. In the collimated mode one can reconstruct the volume of the energy deposition as the intersection of the collimated beam and the trajectories of the γs from the annihilation. For both measurement modes the HPGe detector and the PET scanner are synchronised and read out together. The readout for the prototype PET scanner used was a major part of this thesis.
The goal in measuring position-dependent signal waveforms is to understand the pulse formation inside the HPGe detectors better. The pulse shapes produced in this fashion are so called single site events (SSE), since all the energy get deposited in a small volume. The electron deposits its energy quickly, the positron as well, and the γs cannot interact with the HPGe detector in order to be detected by the PET scanner. All free charges generated are generated in a small volume. Opposed to the SSEs multi site events (MSE) also exist. In these events there are multiple interaction points with the HPGE detector, typically by multi Compton scattering of a γ. SSEs and MSEs can be discriminated by their pulse shape. This is used as background reduction for example in the Large Enriched Germanium Experiment for Neutrinoless $\beta\beta$ Decay (LEGEND). The signature of neutrinoless $\beta\beta$ ($0\nu\beta\beta$) decay is a SSE, as it only produces two electrons which also deposit their energy in a small detector volume. For background radiation like naturally occuring γs, MSEs are expected.
The goal of this work is to characterize the pulse shape discrimination (PSD) for SSEs as a function of the position of the interaction inside of the HPGe detector.

2

Neutrino properties

"Mystery creates wonder and wonder is the basis of man's desire to understand."

- Neil Armstrong, *first person on the Moon*

One of the greatest achievements of humankind is the Standard Model of Particle Physics. The standard model does exceptionally well in describing the baryonic and leptonic matter surrounding us, by describing reality as fields and particles as excitations of said fields. Although it is a major success, there still are several shortcomings of the standard model. It does not account for any additional contents of the universe, such as dark matter or dark energy. More important for this work, it describes neutrinos as massless Dirac-like particles. They do however in fact have mass, which can be proven by neutrino oscillations. Their Dirac nature is not so clear, which can be tested by searching for particle reactions forbidden for Dirac particles, like the neutrinoless double beta decay. Such a decay would produce more matter than anti-matter, violating the lepton number conservation. Such processes can be important to explain the matter

asymmetry, another shortcoming of the Standard Model.
This chapter will give a brief overview about the standard model, followed by a brief overview of known neutrino properties and of neutrino masses. This will be concluded by an overview of the neutrinoless double beta decay and the Seesaw mechanism.

2.1 The standard model of particle physics

The standard model classifies all elementary particles into two classes, fermions and bosons. Fermions make up the matter around us and have half-integer spin (like $-\frac{1}{2}$, $\frac{1}{2}$ or $\frac{3}{2}$). They are further separated into quarks and leptons. The quarks (and their antiparticles) are the constituents of all baryons and mesons. They are classified into three families of quarks, each family heavier than the one before. The lightest family of quarks consists of the up quark and the down quark, which have an electric charge of $+\frac{2}{3}e$ and $-\frac{1}{3}e$ respectively. The next is the charm and strange quark, which are heavier but with the same respective charges. Finally the third known family are the top and bottom quark, even heavier but still with the same respective charges. Additional to their electric charges, the quarks also carry color charge which consists of the three colors red, green and blue (and their anti-colors anti-red, anti-blue and anti-green). Due to their charges quarks can react via the strong interaction and the electromagnetic interaction as well as the weak interaction with which every lepton can interact.
The leptons also have three families, the next one heavier than the one before. Each family consists of a charged lepton and the corresponding neutrino. The lightest family is the electron with electric charge $-e$ and the electron neutrino with electric charge 0. The next heavier family consists of the muon with electric charge $-e$ and the muon neutrino with charge 0. The heaviest family is made up by the tau with electric charge $-e$ and the tau neutrino with electric charge 0. Leptons do not carry color charge and do therefore not react via the strong interaction. The electrically charged leptons react via the electromagnetic interaction and all leptons react via the weak interaction.
The bosons are the carriers of the interactions between particles, for every interaction of strong, weak and electromagnetic at least one boson representing the interaction exists. Bosons have integer spins like -2, 0 or $+1$. Additionally, the Higgs boson was included in the standard model after its discovery. It represents the mass generation for all massive particles, except for neutrinos which are massless in the standard model.
The carriers of the electromagnetic interactions are the photons, massless particles with a spin of

+1. The photons themselves also carry no electric or color charge, they only react with electric charges. The photons have infinite reach, matching the early findings of Maxwell regarding the electromagnetic force.

The weak interaction is mediated by the $W^{\pm}$ and Z^0 bosons. These are massive ($80 - 90\,\mathrm{GeV}$) and for the case of W^+ and W^- carry an electric charge of $+e$ and $-e$ respectively. They all have a spin of 1 and no color charge. Reactions with the W bosons are those weak interactions which do not conserve particle flavor, e.g. can turn an up quark into a down quark. These interactions can even change the flavor across families, e.g. turn an up quark into a strange quark. These interactions can only happen with left-handed fermions, where spin and momentum point in opposite directions. This is what is meant when referring to the parity violation of the weak interaction to maximum extent. The relative strengths of these reactions are combined into Cabbibo-Kobayashi-Maskawa (CKM) matrix, which then yields a matrix equation like the following for flavor change in one of the positively charged quarks:

$$\begin{pmatrix} \langle u|U_{\mathrm{end}}\rangle \\ \langle c|U_{\mathrm{end}}\rangle \\ \langle t|U_{\mathrm{end}}\rangle \end{pmatrix} = \begin{pmatrix} V_{\mathrm{ud}} & V_{\mathrm{us}} & V_{\mathrm{ub}} \\ V_{\mathrm{cd}} & V_{\mathrm{cs}} & V_{\mathrm{cb}} \\ V_{\mathrm{td}} & V_{\mathrm{ts}} & V_{\mathrm{tb}} \end{pmatrix} \cdot \begin{pmatrix} \langle c|U_{\mathrm{init}}\rangle \\ \langle s|U_{\mathrm{init}}\rangle \\ \langle b|U_{\mathrm{init}}\rangle \end{pmatrix} \tag{2.1}$$

The opposite equation is valid for a flavor change of a negatively charged quark. The Z^0 boson can mediate interactions between any two leptons with no limitations by particle properties like charge, but does not change flavors or charges whatsoever. The characteristics is instead like a generic elastic scattering process. The effective reach of the weak interaction is very short with $10^{-16}\,\mathrm{m}$, it is often described as a point-like interaction.

The strong interaction is mediated by the so-called gluons, massless particles with a spin of 1. They carry no electric charge, but always a combination of color and anti-color charge (like red and anti-green). This yields 9 different gluons in total, but the colorless gluons (e.g. red and anti-red) do not exist, making it 8 in total. Despite being massless, the gluons do not have infinite reach, because they can interact with one another (photons cannot). This explains why the colorless gluons are ruled out, they would not interact with other gluons and therefore have infinite reach which cannot be observed. Another property of the strong interaction is the confinement, which means that free color charge can be observed. Protons and neutrons in total are colorless, since (by construction of the color charge) red and green and blue total to colorless. If one would now try to remove one of the quarks from a proton, the force between the

quarks stays constant (opposed to e.g. $\frac{1}{r^2}$ for electromagnetic forces). The potential energy of the system therefore increases linearly beyond the energy needed for a quark anti-quark pair to be created. This creation results in a more favorable energy state since the proton is complete again and what one removed from the proton has effectively become a meson, both colorless with no force between them at sufficient distance. The efficient reach of the strong interaction is several fm, about the size of an atomic nucleus. For short distances the strong interaction becomes weaker, so that e.g. the nuclei in an atomic nucleus are bound to the nucleus but can move relatively free inside of the nucleus. This is what is known as asymptotic freedom.
Due to local symmetries in the standard model bosons must be massless, which is not true for the bosons of the weak interaction. To account for their mass a "mass term" has to be added to the equations of the standard model. This mass term describes the interaction of particles with the so-called Higgs field and is what generates the masses of the particles in the standard model. This interaction is mediated by the Higgs boson, a boson with a spin of 0 and a mass of around 125 GeV. While the effective reach of the interaction is very short, the field is present in the entire universe since its vacuum expectation value is different from 0. With this description the mass of a particle in the standard model becomes a measure for the interaction strength with the Higgs field.

2.2 Neutrino properties

The neutrino was first postulated by Wolfgang Pauli in 1930 [29] as a measure to fulfill energy and momentum conservation for β decays which follow the reaction equations

$$ {}^{A}_{Z}\mathrm{X} \longrightarrow {}^{A}_{Z+1}\mathrm{Y} \; + \; \mathrm{e}^{-} \; + \; \bar{\nu}_{\mathrm{e}} \quad \text{and} \quad {}^{A}_{Z}\mathrm{X} \longrightarrow {}_{Z-1}{}^{A}\mathrm{Y} + \mathrm{e}^{+} + \nu_{\mathrm{e}}. \tag{2.2} $$

The only particles detectable at that time were the produced electron (or positron) and the atomic nucleus. The energy transferred to the atomic nucleus is negligible due to its high mass compared to the electron, so as a good estimate the electron could be considered to carry the entire energy of the decay. With momentum conservation, the energy should be split between nucleus and electron with the same proportion for every decay of the same isotope. This would lead to a monoenergetic line at the Q value of the decay as the energy spectrum of the electron. In reality what can be observed is a continuous energy spectrum from 0 to the Q value of the decay. This violates the energy and momentum conservation looking only at the particles observable at

that time. Pauli suggested an additional product particle which cannot be detected and therefore can carry away the missing energy and momentum. This would make the β decay a 3-body-decay where energy and momentum can be distributed arbitrarily as long as energy and momentum are conserved. This assumption was compatible with the observed spectra and investigated further. The particle could not be completely undetectable as it took part in at least one interaction, the β decay. A very similar reaction was used for its initial detection, the inverse β decay. The experiment was carried out by Cowan and Reines in 1956 [11] and resulted in the detection of the electron anti-neutrino. In an inverse β decay a (anti-) neutrino reacts with a neutron (proton) transforming it into a proton (neutron) and an electron (positron):

$$ {}^{\mathrm{A}}_{\mathrm{Z}}\mathrm{X} + \nu_{\mathrm{e}} \longrightarrow {}^{\mathrm{A}}_{\mathrm{Z+1}}\mathrm{Y} + \mathrm{e}^{-} \quad \text{and} \quad {}^{\mathrm{A}}_{\mathrm{Z}}\mathrm{X} + \bar{\nu}_{\mathrm{e}} \longrightarrow {}^{\mathrm{A}}_{\mathrm{Z-1}}\mathrm{Y} + \mathrm{e}^{+}. \tag{2.3} $$

If this reaction happens on a hydrogen nucleus, the result is a free neutron and a positron. The positron annihilates, producing two characteristic γs with $m_{\mathrm{e}} = 511\,\mathrm{keV}$. The neutron thermalises and is then captured by another nucleus, releasing at least some of the difference binding energy as one or more γs. If the neutron is captured on a hydrogen nucleus, a single characteristic γ with 2.2 MeV is emitted. The detection signature for an inverse beta decay is therefore a delayed coincidence between between the annihilation γs and the neutron capture γ, all with characteristic energies. After the detection of the electron neutrino, the existence of neutrinos for the other charged leptons was expected and they were detected over the course of the next 30 years. The muon neutrino was detected in a beam experiment at the Brookhaven National Laboratory in 1962 [12]. For the detection a pion beam was produced by shooting protons on a beryllium target, the produced pions decaying in-flight via

$$ \pi^{+} \longrightarrow \mu^{+} + \nu_{\mu} \text{ and } \pi^{-} \longrightarrow \mu^{-} + \bar{\nu}_{\mu}. \tag{2.4} $$

The beam was pointed onto a heavily shielded spark chamber, so that mostly neutrinos could get into the spark chamber. The signature then was a muon track originating inside of the spark chamber. With this experiment it was also concluded that the muon neutrino was in fact different from the electron neutrino, since only muons were produced in the spark chamber. Electrons and muons could be discriminated by their different kinematics due to their very different masses. The tau neutrino was discovered by the DONUT experiment in 2001 with a principle similar to the muon neutrino [15]. Protons were shot onto a tungsten target, producing charmed mesons.

The main production channel for τ neutrinos is the decay of the D_S meson:

$$D_S \longrightarrow \tau^- + \nu_\tau. \tag{2.5}$$

These neutrinos were shot onto four heavily shielded modules of emulsion plates which allow to reconstruct particle tracks. Due to the heavy shielding only neutrinos could make it to the modules with a significant flux. The signature for an interaction of a tau neutrino was again a track of a tau starting only somewhere inside of the shielded volume. The leptons can again be discriminated by their kinematics.

A notable property of the neutrinos and the weak interaction can be observed with the aforementioned pion decay

$$\pi^- \longrightarrow \mu^- + \bar{\nu}_\mu \text{ and } \pi^- \longrightarrow e^- + \bar{\nu}_e. \tag{2.6}$$

Naively one would expect that the pion decay into electron and anti electron neutrino is greatly enhanced due to the large phase space volume the lighter electron covers compared to the much heavier muon. What can be observed in reality is the opposite, the decay into an electron is greatly suppressed and most pions decay into muons. This can be explained with parity violation of the weak interaction to its maximum extent. This means that the weak interaction only couples to left-handed particles and right-handed anti-particles, where the handedness or the helicity is defined as

$$H = \frac{\vec{p} \cdot \vec{s}}{|\vec{p}| \cdot |\vec{s}|}. \tag{2.7}$$

The helicity is a measure for how much momentum and spin of a particle are aligned (or anti-aligned). It is a good quantum number only for massless particles, as these move with the speed of light. For slower particle another system of inertia can always be found in which the direction of the momentum is opposite and the helicity flips in the other direction. This is what governs the counter-intuitive decay scheme of the (charged) pions. The charged pions have spin 0 and therefore the produced particles need to have opposite spin directions so they cancel out in total. The neutrino is basically always left-handed due to its very low mass and the weak interaction only coupling to it left-handed. Since not only the spin but also the momentum of the anti particle has to be the opposite of the neutrino, the anti-particle is also left-handed (just with the vectors pointing in the opposite direction respectively). So what needs to be produced by the weak interaction is a left-handed anti particle which is forbidden. Due to the larger mass of the anti muon, there are more systems of inertia in which the anti muon is right-handed (momentum

points in the other direction) than there are for the positron and therefore the decay into (anti) electrons is suppressed compared to that into (anti) muons.

As mentioned before, the neutrinos do have masses despite being described as massless in the standard model. The discovery has its foundation in the solar neutrino problem. In the late 1960s, Raymond Davis Jr. and John Bahcall wanted to measure the solar neutrino flux with the Homestake experiment to test their model of the fusion processes taking place in the sun [33]. Compared to the other neutrino detection principles before, the Homestake experiment employs a radio chemical detection mechanism. (Anti) neutrinos with sufficient energy can perform an inverse beta decay where the (anti) neutrino interacts with the atomic nucleus and transforms a neutron (proton) into a proton (neutron) and an electron (positron). The specific reaction used in Homestake was

$$\nu_\mathrm{e} + {}^{37}\mathrm{Cl} \longrightarrow {}^{37}\mathrm{Ar} + \mathrm{e}^- \tag{2.8}$$

taking place on 380 cubic meters of perchlorethylene stored roughly 1500 m underground in the Homestake gold mine. The argon atoms were extracted and counted every couple of weeks and the neutrino flux estimated from the number of produced atoms. Despite reasonable assumptions for their model of the nuclear reactions in the sun, the measured flux was only one third of their expectations. This discrepancy between well-motivated expectation and measurement of the solar neutrino flux is known as the solar neutrino problem. This problem was resolved over the course of the next 30 years. The proposed solution that came out to be correct came from Bruno Pontecorvo in 1968 [17]. His idea was that if neutrinos have mass, which was still unknown at that point, could transform from one flavor into another. This would be made possible by the flavor eigenstates in which neutrinos are produced are different from the mass eigenstates which are those that propagate, so move through the universe. In mathematical terms that means that the orthogonal axes making up the space of the flavor eigenstates $|\nu_\mathrm{e}\rangle$, $|\nu_\mu\rangle$ and $|\nu_\tau\rangle$ are rotated relative to the orthogonal axes making up the space of the mass eigenstates $|\nu_1\rangle$, $|\nu_2\rangle$ and $|\nu_3\rangle$. This is also visualised in figure 2.1. In this mathematical description the rotation can be described by seeing the flavor eigenstates as superposition of the mass eigenstates and vice versa:

$$|\nu_\alpha\rangle = \sum_i U^*_{\alpha i} |\nu_i\rangle \text{ and } |\nu_i\rangle = \sum_\alpha U_{\alpha i} |\nu_\alpha\rangle \tag{2.9}$$

where U is the Pontecorvo-Maki-Nakagawa-Sakata matrix (PMNS matrix) describing the angles. The entries of the PMNS matrix can be calculated by multiplying the contributions of the of the

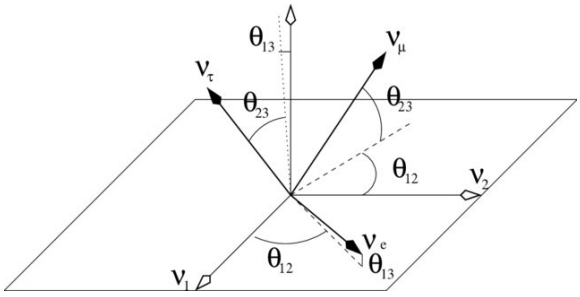

Figure 2.1: Visualisation of the rotation of the orthogonal axes of the flavor eigenstates relative to the mass eigenstates of the neutrinos. The rotation angles of the mixing matrix are also inscribed in the figure.

different eigenstates to the mixing:

$$U = \begin{pmatrix} U_{e1} & U_{e2} & U_{e1} \\ U_{\mu 1} & U_{\mu 2} & U_{\mu 3} \\ U_{\tau 1} & U_{\tau 2} & U_{\tau 3} \end{pmatrix} = \begin{pmatrix} 1 & 0 & 0 \\ 0 & \cos(\theta_{23}) & \sin(\theta_{23}) \\ 0 & -\sin(\theta_{23}) & \cos(\theta_{23}) \end{pmatrix} \cdot \begin{pmatrix} \cos(\theta_{13}) & 0 & \sin(\theta_{13})\, e^{-i\delta} \\ 0 & 1 & 0 \\ -\sin(\theta_{13})\, e^{-i\delta} & 0 & \cos(\theta_{13}) \end{pmatrix}$$
$$\cdot \begin{pmatrix} \cos(\theta_{12}) & \sin(\theta_{12}) & 0 \\ -\sin(\theta_{12}) & \cos(\theta_{12}) & 0 \\ 0 & 0 & 1 \end{pmatrix} \cdot \begin{pmatrix} 1 & 0 & 0 \\ 0 & e^{i\alpha} & 0 \\ 0 & 0 & e^{i\beta} \end{pmatrix}, \tag{2.10}$$

where the angles are named according to figure 2.1, α and β are phases only relevant if neutrinos are Majorana particles and δ is the CP violating phase. The timely evolution of a neutrino mass eigenstate is given as

$$|\nu_k(t)\rangle \approx e^{-iE_k t + ip_k L} |\nu_k\rangle \tag{2.11}$$

with k naming a mass eigenstate and with some relativistic approximations. The transition amplitude for a neutrino of flavor α to a flavor β is given as

$$\langle\nu_\beta|\nu_\alpha(t)\rangle = \langle\nu_\beta| \sum_{\gamma=(\mathrm{e},\mu,\tau)} \sum_{k=1}^{3} U_{\alpha k} e^{-iE_k t + ip_k L} U^*_{\gamma k} |\nu_\gamma\rangle \tag{2.12}$$

$$= \sum_{\gamma=(\mathrm{e},\mu,\tau)} \sum_{k=1}^{3} U_{\alpha k} e^{-iE_k t + ip_k L} U^*_{\gamma k} \langle\nu_\beta|\nu_\gamma\rangle \tag{2.13}$$

$$= \sum_{\gamma=(\mathrm{e},\mu,\tau)} \sum_{k=1}^{3} U_{\alpha k} e^{-iE_k t + ip_k L} U^*_{\gamma k} \cdot \delta_{\beta\gamma} \tag{2.14}$$

$$= \sum_{k=1}^{3} U_{\alpha k} U^*_{\beta k} e^{-iE_k t + ip_k L}. \tag{2.15}$$

The probability to detect a particle emitted in flavor eigenstate α in flavor eigenstate β is then given as the square of the absolute value of the transition amplitude:

$$P(\alpha \to \beta) = |\langle\beta|\alpha\rangle|^2 = \left| \sum_{k=1}^{3} U_{\alpha k} U^*_{\beta k} e^{-iE_k t} \right|^2 = \left(\sum_{k=1}^{3} U_{\alpha k} U^*_{\beta k} e^{-iE_k t} \right) \cdot \left(\sum_{j=1}^{3} U^*_{\alpha j} U_{\beta j} e^{+iE_j t} \right) \tag{2.16}$$

$$= \sum_{k=1}^{3} \sum_{j=1}^{3} U_{\alpha k} U^*_{\alpha j} U^*_{\beta k} U_{\beta j} e^{-i(E_k - E_j)t} e^{i(p_k - p_j)L} \tag{2.17}$$

$$= \sum_{k=j} |U_{\alpha k}|^2 |U_{\beta k}|^2 + \cdot\mathrm{Re}\left(\sum_{k<j} U_{\alpha k} U^*_{\alpha j} U^*_{\beta k} U_{\beta j} e^{-i(E_k - E_j)t} e^{i(p_k - p_j)L} \right) \tag{2.18}$$

$$+ \cdot\mathrm{Re}\left(\sum_{j<k} U_{\alpha k} U^*_{\alpha j} U^*_{\beta k} U_{\beta j} e^{-i(E_k - E_j)t} e^{i(p_k - p_j)L} \right) \tag{2.19}$$

$$= \sum_{k=j} |U_{\alpha k}|^2 |U_{\beta k}|^2 + 2 \cdot \mathrm{Re}\left(2 * \sum_{k<j} U_{\alpha k} U^*_{\alpha j} U^*_{\beta k} U_{\beta j} e^{-i(E_k - E_j)t} e^{i(p_k - p_j)L} \right) \tag{2.20}$$

$$\approx \sum_{k=j} |U_{\alpha k}|^2 |U_{\beta k}|^2 + 2 \cdot \mathrm{Re}\left(2 * \sum_{k<j} U_{\alpha k} U^*_{\alpha j} U^*_{\beta k} U_{\beta j} \exp\left(-i \frac{\Delta m^2_{kj} L}{2E} \right) \right). \tag{2.21}$$

with $\Delta m^2_{kj} = m^2_k - m^2_j$. By measuring the transition probability for different energies and neutrino flavors, the entries of the PMNS matrix can be calculated [14]. The currently best

measurements of the magnitudes of the entries of the PMNS matrix are

$$|U| = \begin{pmatrix} |U_{e1}| & |U_{e2}| & |U_{e1}| \\ |U_{\mu 1}| & |U_{\mu 2}| & |U_{\mu 3}| \\ |U_{\tau 1}| & |U_{\tau 2}| & |U_{\tau 3}| \end{pmatrix} = \begin{pmatrix} 0.803\ 0.845 & 0.514\ 0.578 & 0.142\ 0.155 \\ 0.233\ 0.505 & 0.460\ 0.693 & 0.630\ 0.779 \\ 0.262\ 0.525 & 0.473\ 0.702 & 0.610\ 0.762 \end{pmatrix}. \tag{2.22}$$

What is still left to find out is the so-called mass hierarchy, finding out whether $m_3 > m_2, m_1$ or $m_3 < m_2, m_1$. This can be achieved by measuring the transition probabilities with unprecedented precision, since the signs of the mass differences Δm_{kj} have an effect on the exact shape of the transition probability spectrum as can be seen in equation 2.21.

2.3 $0\nu\beta\beta$ decay and the Seesaw mechanism

In cases for which the discussed β decay is energetically forbidden, the double beta decay $\beta\beta$ may occur. For a constant number of nuclei A, the masses of the isobarics can be plotted as a function of the atomic number Z. For an even A these masses follow two parabolas, the even-even and the odd-odd parabola. The difference in the masses mainly stems from the pairing term in the Bethe Weizsäcker formula for nuclei masses. An example for these parabolas can be seen in figure 2.2. From a given starting point, a β^- decay goes one element to the right (increasing the number of protons by 1), a β^+ goes one element to the left (decreasing the number of protons by 1). The decays happen towards the lower mass, releasing the difference in energy. When one starts from ^{76}Ge shown in the aforementioned figure, the nucleus sits in a local minimum with the neighbouring nuclei being heavier. No energy can be freed up in a β decay, so it does not occur. However, the next to next neighbour, ^{76}Se has lower mass, which means energy can be freed up when moving from ^{76}Ge to ^{76}Se. In order to make this transition, two β decays have to happen at the same time, a $\beta\beta$ decay. The reaction equation is then given as

$$^{76}\mathrm{Ge} \longrightarrow {}^{76}\mathrm{Se} + 2\,\mathrm{e}^- + 2\,\bar{\nu}_e. \tag{2.23}$$

Note that 2 $\bar{\nu_e}$ are produced in order to conserve the lepton number L with the two produced electrons. This double beta decay $2\nu\beta\beta$ decay has been observed e.g. in ^{76}Ge by the GERDA collaboration with a half-life of $T^{2\nu}_{1/2} = (1.926 \pm 0.094) \cdot 10^{21}$ yr [2].

One of the key properties of the weak interaction is the parity violation, meaning it couples only to left-handed ν and right-handed $\bar{\nu}$. Since these still have the weak iso-spin as a quantum

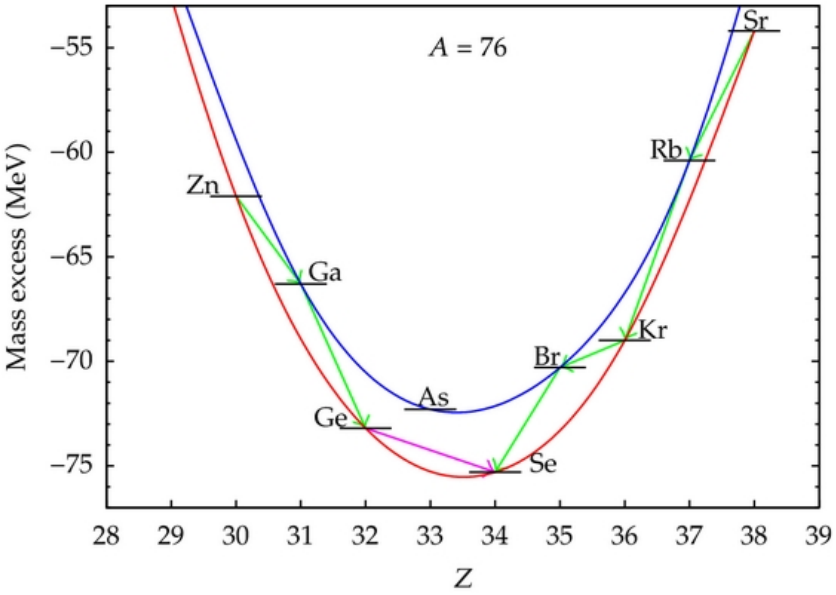

Figure 2.2: Even-even and odd-odd mass parabolas for $A = 76$, the nucleon masses as function of the atomic number for fixed number of nuclei. The green arrows symbolize β decays, with arrows to the right being β^- and arrows to the left being β^+ decays. The purple arrow shows a $\beta\beta$ decay happening where β decays are energetically forbidden. Taken from [16].

number, they can be discriminated. On the other hand, potential right-handed ν and left-handed $\bar{\nu}$ are truly neutral. Therefore it is possible that these are the same particles. The idea of neutral particles being their own anti-particles was first introduced by Ettore Majorana [23], after whom such particles are called Majorana particles. If these sterile ν are indeed their own anti-particles and they follow the seesaw mechanism, all neutrinos would be at least partially Majorana particles.

This derivation closely follows the one found in [7].

Using the formulation of quantum field theory, more exactly the Dirac equation

$$(i\hbar\gamma^\mu\partial_\mu - mc)\,\psi(x) = 0, \tag{2.24}$$

the neutrinos and anti-neutrinos (sterile and not sterile) can be represented as spinors.

The spinors of the not sterile left-handed neutrino and right-handed anti-neutrino can be expressed as

$$\psi_\mathrm{L} = \left(\frac{1-\gamma^5}{2}\right)\psi \text{ and } (\psi^c)_\mathrm{R} = \left(\frac{1+\gamma^5}{2}\right)\psi^c \tag{2.25}$$

with the solutions of the Dirac equations ψ and ψ^c. The spinors of the sterile left-handed neutrino and right-handed anti-neutrino can be expressed as

$$\psi_{\mathrm{R}} = \left(\frac{1+\gamma^5}{2}\right)\psi \text{ and } (\psi^c)_{\mathrm{L}} = \left(\frac{1-\gamma^5}{2}\right)\psi^c. \tag{2.26}$$

The most general expression for the Hamiltonian of a neutrino with field $\psi = \psi_{\mathrm{L}} + \psi_{\mathrm{R}}$ is then given as

$$H = M_{\mathrm{D}}\bar{\psi}_{\mathrm{R}}\psi_{\mathrm{L}} + \frac{1}{2}M_{\mathrm{L}}(\bar{\psi^c_{\mathrm{L}}})\psi_{\mathrm{L}} + \frac{1}{2}M_{\mathrm{R}}\bar{\psi}_{\mathrm{R}}(\psi_{\mathrm{R}})^c + \mathrm{h.c.} \tag{2.27}$$

with the couplings M_{D}, M_{L} and M_{R}. This formulation is only valid for particles with charge $q = 0$, so i.e. Majorana particles. The couplings do not represent the physical masses, for these one has to find the eigenstates and eigenvalues of the Hamiltonian. For that one can define the two fields

$$f = \frac{\psi_{\mathrm{L}} + (\psi^c)_{\mathrm{L}}}{\sqrt{2}} = \frac{\psi_{\mathrm{L}} + (\psi^c)_{\mathrm{R}}}{\sqrt{2}} \text{ and } F = \frac{\psi_{\mathrm{R}} + (\psi^c)_{\mathrm{R}}}{\sqrt{2}} = \frac{\psi_{\mathrm{R}} + (\psi^c)_{\mathrm{L}}}{\sqrt{2}}, \tag{2.28}$$

again only valid for charge $q = 0$. Using these fields and only keeping the terms with opposite chiralities the Hamiltonian can be rewritten as

$$H = M_{\mathrm{L}}\bar{f}f + M_{\mathrm{R}}\bar{F}F + M_{\mathrm{D}}(\bar{f}F + \bar{F}f) = (\bar{f}, \bar{F})\begin{pmatrix} M_{\mathrm{L}} & M_{\mathrm{D}} \\ M_{\mathrm{D}} & M_{\mathrm{R}} \end{pmatrix}\begin{pmatrix} f \\ F \end{pmatrix}. \tag{2.29}$$

The attempt to diagonalize the matrix leads to the secular equation

$$(M_{\mathrm{L}} - m)\dot{(}M_{\mathrm{R}} - m) - M_{\mathrm{D}}^2 = 0 \tag{2.30}$$

with the solutions

$$m_{1,2}\frac{M_{\mathrm{R}} + M_{\mathrm{L}}}{2} \mp \sqrt{\frac{(M_{\mathrm{R}} - M_{\mathrm{L}})^2}{4} + M_{\mathrm{D}}^2}. \tag{2.31}$$

If now one considers the case of $M_{\mathrm{L}} = 0$ and $M_{\mathrm{R}} >> M_{\mathrm{D}}$ the solutions for m_1 and m_2 become

$$m_1 \approx \frac{M_{\mathrm{R}}}{2} - \frac{M_{\mathrm{R}}}{2}\left(1 + 2\frac{M_{\mathrm{D}}^2}{M_{\mathrm{R}}^2}\right) = -\frac{M_{\mathrm{D}}^2}{M_{\mathrm{R}}} \tag{2.32}$$

and

$$m_2 \approx \frac{M_{\mathrm{R}}}{2} + \frac{M_{\mathrm{R}}}{2}\left(1 + 2\frac{M_{\mathrm{D}}^2}{M_{\mathrm{R}}^2}\right). \tag{2.33}$$

The corresponding eigenstates in the base of (f, F) are then given by

$$\nu \approx f + \frac{M_{\mathrm{D}}}{M_{\mathrm{R}}} F \approx f \tag{2.34}$$

and

$$N \approx F - \frac{M_{\mathrm{D}}}{M_{\mathrm{R}}} f \approx F. \tag{2.35}$$

Using these results the following relation can be found:

$$m_1 \cdot m_2 = M_\nu \cdot M_{\mathrm{R}} \approx M_{\mathrm{D}}^2. \tag{2.36}$$

The mass eigenstates are therefore a superposition of the left-handed Dirac neutrino and the right-handed Dirac anti-neutrino (ν) and a superposition of the right-handed Dirac neutrino and the left-handed Dirac anti-neutrino. Additionally, since $m_1 \cdot m_2$ is constant, very light left-handed reactive (anti-)neutrinos can be compensated by very heavy sterile (anti-)neutrinos. Additionally, the reactive neutrino and anti-neutrino correspond to the same mass eigenstate, describing the popular $\nu = \bar{\nu}$ equation often seen in conjunction with the Seesaw mechanism.

3

The LEGEND-200 experiment

"The charm of fishing is that it is the pursuit of what is elusive but attainable, a perpetual series of occasions for hope."

- John Buchan, *Scottish politician*

The largest effort in the search of a possible $0\nu\beta\beta$ decay in ^{76}Ge so far is the LEGEND collaboration. It was formed from the members of the GERDA and MAJORANA collaborations to combine the experience and techniques of the similar experiments. The first iteration, LEGEND-200 is set up at the Laboratori Nazionali del Gran Sasso (LNGS) below the Gran Sasso massive in Italy. The detection medium is the same as for GERDA and MAJORANA: high purity germanium (HPGe) spectroscopy detectors made from germanium enriched in ^{76}Ge from the natural level of about 8 % to over 90 %. The decay, should it exist, can then take place directly in the detector volume and a high detection efficiency is achieved. The high detection efficiency has to go hand in hand with a low background index (BI) in the region of interest (ROI). Otherwise

even a relatively large amount of candidate events for the $0\nu\beta\beta$ decay can easily be attested to the background events. If the experiment is background free, meaning $BI = 0$ the sensitivity for a half-life is given as

$$T_{1/2} = \epsilon \frac{\ln(2) \cdot f \cdot N_{\mathrm{A}}}{M_{\mathrm{Ge}}} \frac{\sum_{i=\mathrm{detector}} m_i \cdot T_i}{N_{\mathrm{S}}} \tag{3.1}$$

where ϵ is the detection efficiency, f is the enrichment factor, N_{A} is the Avogadro number, M_{Ge} is the atomic mass of ^{76}Ge, m_i and T_i are the respective detector masses and livetimes and N_{S} is the amount of signal events. For a realistic case where $BI \neq 0$ the sensitivity is described by

$$T_{1/2} = \epsilon \frac{\ln(2) \cdot f \cdot N_{\mathrm{A}}}{M_{\mathrm{Ge}}} \sqrt{\frac{\sum_i m_i \cdot T_i}{BI \cdot \Delta E}} \tag{3.2}$$

where BI is the background index at $Q_{\beta\beta}$ and ΔE is the energy resolution at $Q_{\beta\beta}$. Various graphs visualizing the sensitivity as function of exposure for different BIs are shown in figure 3.1. To reduce the BI as much as possible, multiple strategies for background reduction are employed

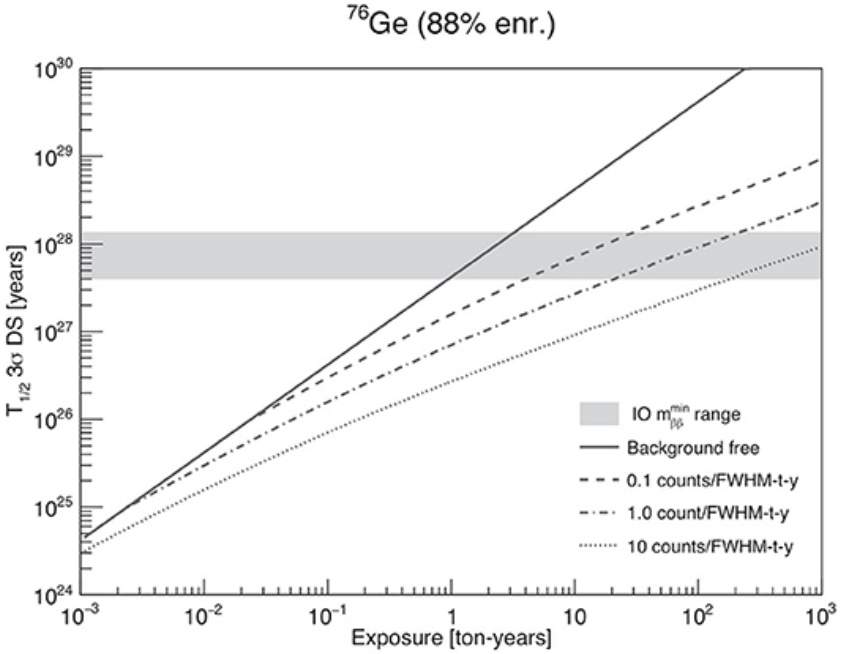

Figure 3.1: Sensitivity for discovery with different half-lifes for different background indices. The enrichment fraction for these numbers is $f = 88\,\%$ as inscribed in the graph. Taken from [4].

in multiple layers. A sketch of these layers can be seen in figure 3.2. The innermost method is the pulse shape discrimination (PSD) of the HPGe detectors used in the event selection. More details of this strategy will be discussed in the chapter regarding HPGe detectors. The next

layer for background reduction is the cryostat filled with liquid argon (LAr) in which the HPGe detectors are operated cryogenically. The LAr is equipped with an array of light guide fibers ending at silicon photo multipliers (SiPM) which together form the LAr veto. In the event of external ionizing radiation entering the cryostat an energy deposition in the LAr produces light via scintillation. The light gets captured in the fibers and guided to the SiPMs. For a sufficient amount of light detected in a short time window, the LAr veto sends an electronic signal to the central data acquisition (DAQ) of the experiment signalling external radiation. The next layer of background reduction consists of the water tank surrounding the cryostat equipped with roughly 60 photo multiplier tubes (PMT), together forming the water Cherenkov muon veto (muon veto). As contributions to the muon veto will be discussed in a later chapter, the geomety of the muon veto will be discussed here in more detail than the other systems. The water tank surrounding the cryostat has a diameter of about 10 m and a height of about 9 m. It includes a circular wall at the bottom with two manholes to support the cryostat. This volume between in the water tank under the cryostat is called the pillbox due to its shape being that of a flat cylinder. The PMTs are distributed on the inner wall and floor of the water tank and also in the pillbox. 10 PMTs are distributed throughout the pillbox, 20 PMTs are distributed on the floor surrounding the pillbox and 23 PMTs are mounted on the inner wall of the water tank. In the transition from GERDA to LEGEND the topmost PMTs on the water tank wall were moved to the floor and into the pillbox to increase the sensitivity there. Sketches of the old as well as the new PMT distribution can be seen in figure 3.3. The entire inner surface of the water tank is covered in VM 2000 foil, a highly reflective foil manufactured by 3M. The only surface not covered is the top of the water tank, due to it not being reachable with the manlift fitting just through the manhole in the water tank. The calibration system of the muon veto consists of five balls distributed throughout the water tank that can produce short pulses of light which can be in turn recorded with the PMTs. The final and only passive layer of background reduction is the location of the experiment. LEGEND-200 is located at the LNGS which features roughly 1200 m of rock overburden, amounting to 3400 m w e of shielding. This reduces e.g. cosmogenic muons considerably, making it even viable to conduct the experiment. Without this passive shielding the experiment would be vetoed by the active components basically the entire time, resulting in an effective livetime of 0. The LEGEND experiment is planned in multiple stages, the first one being LEGEND-200 with 200 kg of active detector mass. The follow-up stage LEGEND-1000 will feature 1000 kg of active detector mass and is currently under conceptional design review. Additional to the increased mass for LEGEND-1000 the BI will be further reduced, potentially

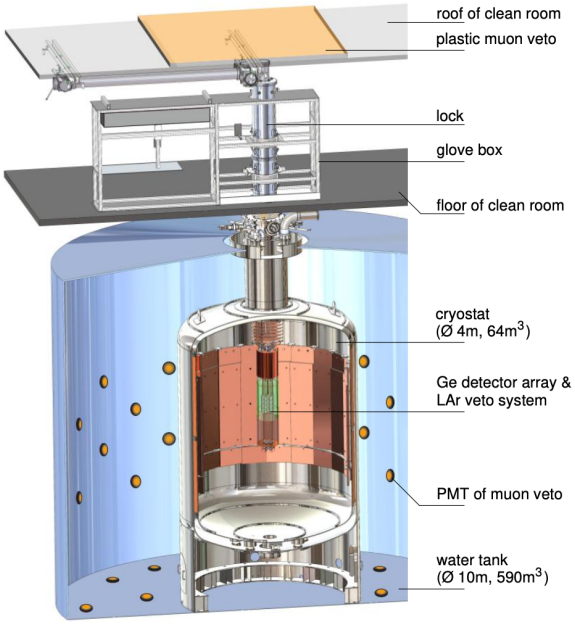

Figure 3.2: Sketch of a cross section of LEGEND-200. The plastic muon veto had to be removed due to increased height of the cleanroom compared to GERDA, the rest of the labels are accurate. Image courtesy of the LEGEND collaboration.

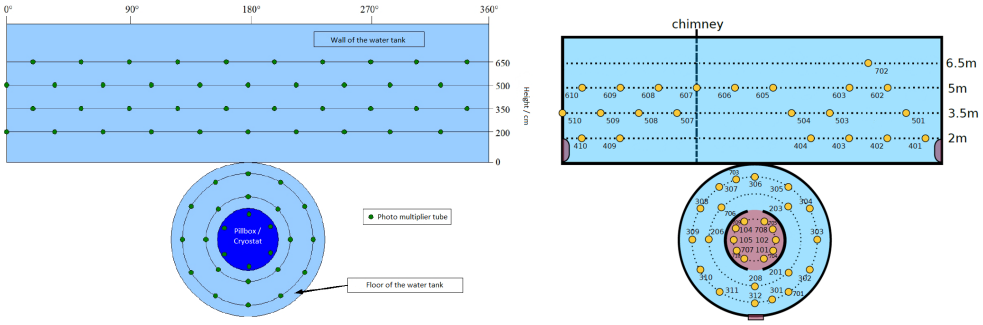

Figure 3.3: Left: Distribution of the PMTs in the muon veto of GERDA. Taken from [22]. Right: Distribution of the PMTs in the muon veto of LEGEND. The missing PMTs have not been removed from the tank but are broken or have been relocated from the top of the wall to the floor and into the pillbox. Taken from [18].

by more sophisticated PSD techniques among other measures. These techniques can be based on a better understanding of pulse formation in different regions of the detector. For example the outer volume of the detector could be used as shielding as well by rejecting any event coming

from these regions. The location could be recovered from the pulse shape if the dependence on the interaction location is known well enough. The test stand presented in this work can be used for measurements suitable do measure the dependence of the pulse shape on the location of the energy deposition and thereby, in extension of this knowledge, help to further reduce the BI in LEGEND.

4

High purity germanium detectors

"Say "hello" to my little friend!"

- Tony Montana, *Scarface (1983)*

HPGe detectors are the detectors used by LEGEND in the search for the $0\nu\beta\beta$ decay and are the target of the presented test stand. These detectors are also commonly used in X ray and γ spectroscopy for various appliances. This chapter will give a brief overview about the working principles of the detectors. Since the signals in these detectors is produced by ionization in the detector, the interaction of ionizing radiation with matter will also be discussed.

4.1 HPGe detector properties

As a semiconductor, a germanium crystal has two energy bands for its electrons, the valence band and the conduction band. The electrons in the conduction bands are able to conduct

electric currents, the valence band electrons are not. In a perfect crystal at $0K$ the conduction band is empty and germanium non-conducting, which is never the case for real setups. In the case of ionizing radiation interacting with germanium, a free electron with kinetic energy of deposited energy minus binding energy is produced. This electron interacts with the electrons in the valence band and can elevate these to the conduction band. The holes in the valence band are then considered positive charges, since negative charge is missing there. The amount of electrons elevated to the conduction band $N_{\text{e-h pair}}$ is given as

$$N_{\text{e-h pair}} = \frac{E_{\text{e}}}{E_{\text{e-h pair}}} \tag{4.1}$$

with the energy of the free electron E_{e} and the energy to create a single electron hole pair $E_{\text{e-h pair}}$. This amount is therefore proportional to the deposited energy. In realistic cases with many electrons populating the conduction band, these newly added electrons are very hard to detect over the background. In order to be able to detect these electrons, the conduction band has to be emptied. To realize that, the crystal is cooled to usually liquid nitrogen temperature ($\approx 96\,\text{K}$) to prevent too many thermal excitations from valence band to conduction band. Additionally high voltage (HV) is applied to opposing surfaces of the crystal. This makes all charges in the conduction band move to the according electrode and further empties the conduction band. The result is a depleted germanium crystal in which newly produced electron hole pairs are well above the background. The electrons and holes can then move to their respective electrode. The current in the electrodes is however not produced with the arrival of the charges at the electrodes but by the motion of the charges according to the Shockley Ramo theorem [31]. It states that the current at the electrodes comes from the movement of the charges relative to the electrodes. The total charge Q that can be readout at the electrodes is then given as

$$Q = -q\phi_0(\vec{x}) \tag{4.2}$$

with the moving charge q and the so called weighting potential $\phi(\vec{x})$ at the position of the production of the charge $\vec{x}$. The weighting potential is a dimensionless scalar in every point. Similar to that the current i instantaneously induced in the electrodes can be calculated as

$$i = q\vec{v} \cdot E_0(\vec{x}) \tag{4.3}$$

with the instantaneous velocity $\vec{v}$ of the charge and the weighting field $E_0(\vec{\ })$ at the instantaneous position of the charge. The weighting field relates to the weighting potential via $E_0(\vec{x}) = -\vec{\nabla}\phi_0$. The weighting potential and field can be calculated as the electric potential and field if the observed electrode was at unit potential, the other electrode grounded and all charges were removed. The velocity of the charge can be calculated using the electric field $E(\vec{x})$ and the mobility μ:

$$v(\vec{x}) = \mu\vec{E}(\vec{x}). \tag{4.4}$$

Therefore the knowledge of electric and weighting field for a detector is sufficient to describe the pulse formation (i.e. i and Q) inside the detector. With measurements of the pulse shapes for charges created in a specific location in the detectors, the calculations can be verified and the understanding of the detectors improved.

4.2 Interactions with matter

As the pulse shape in the HPGe detectors is used to discriminate between different classes of events produced by different kinds of radiation, a quick overview of potential interactions is given.

4.2.1 α particles interacting with matter

α radiation consists of completely ionized ^{4}He nuclei emitted by heavy nuclei in α decays. Therefore they are massive and have a charge of +2e. Their energy loss when passing through matter is described by the Bethe [9] formula for the stopping power

$$-\frac{\mathrm{d}E}{\mathrm{d}x} = \frac{4\pi n Z^2}{m_e c^2 \beta^2} \cdot \left(\frac{e^2}{4\pi\epsilon_0}\right) \cdot \left(\ln\left(\frac{2m_e c^2\beta^2}{I\cdot(1-\beta^2)}\right) - \beta^2\right) \tag{4.5}$$

with the number density of electrons n, the atomic number Z, the electron mass m_e, the speed of light in vacuum c, the velocity of the particle in natural units β, the electric constant ϵ_0 and the mean excitation energy I. The formula describes the mean energy loss per unit of length travelled in a medium for fast charged particles. The energy is lost due to interaction with the atomic shells of the material, exciting or ionizing the atoms. For α particles "fast" means energies of $\sim 100\,\mathrm{keV}$. An example for the range of alpha radiation at different energies is shown in figure 4.1.

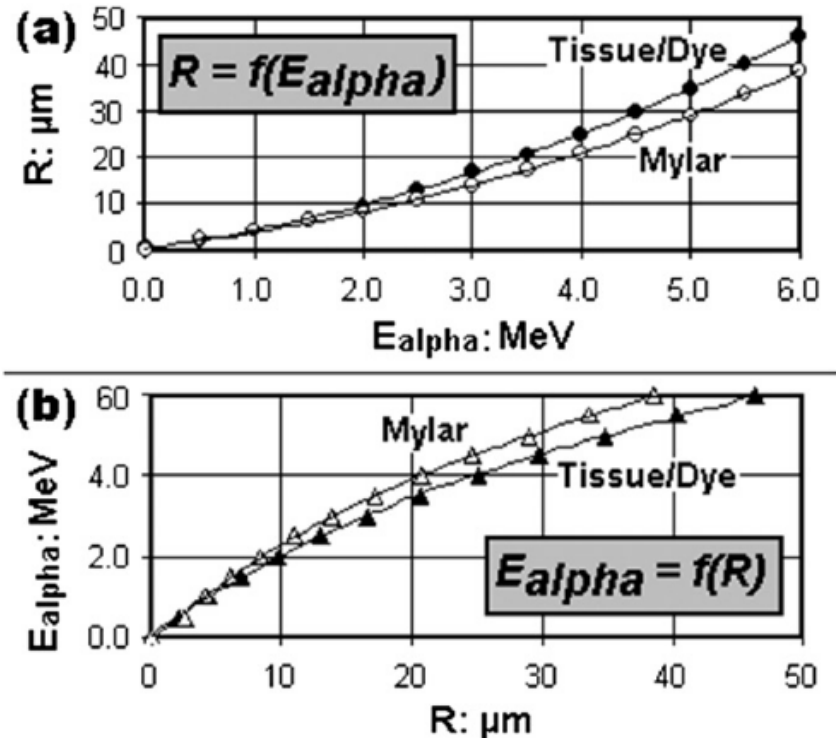

Figure 4.1: Range of alpha particles in body tissue and mylar. The range of the particles is on the order of several 10 μm. Taken from [27].

4.2.2 β particles interacting with matter

For β radiation additional effects compared to α radiation have to be considered. Due to its much lower mass, more Bremsstrahlung is produced and the relativistic terms are relatively more important. Additionally, the indistinguishability of the e^- makes a difference in the interactions compared to the α particles. This leads to the Berger Seltzer [8] formula for the stopping power

$$\frac{\mathrm{d}E}{\mathrm{d}x} = \frac{2\pi r_e^2 m_e c^2 n}{\beta^2} \cdot \left(\ln\left(\frac{2(\gamma+1)}{\left(\frac{I}{mc^2}\right)^2} \right) + F^{\pm}\left(\tau, \tau_{\mathrm{up}}\right) - \delta \right) \tag{4.6}$$

with the classical electron radius r_e, the electron mass m_e, the electron density n, the velocity of the particle in natural units β,the Lorentz factor γ, the mean excitation energy I, the functions $F^{\pm}$ for electron and positron of the reduced kinetic energy $\tau = \frac{T}{m_e}$ and the reduced maximum

energy transfer τ_{up} and the density effect function δ. The function F^+ is given as

$$F^+(\tau,\tau_{\text{up}}) = \ln(\tau\cdot\tau_{\text{up}}) - \frac{\tau_{\text{up}}^2}{\tau}\cdot\left(\tau + 2\tau_{\text{up}} - \frac{3\tau_{\text{up}}^2 y}{2} - \left(\tau_{\text{up}} - \frac{\tau_{\text{up}}^3}{3}\right)\cdot y^2 - \left(\frac{\tau_{\text{up}}^2}{2} - \tau\cdot\frac{\tau_{\text{up}}^3}{3} + \frac{\tau_{\text{up}}^4}{4}\right)\cdot y^3\right) \tag{4.7}$$

and the function F^- as

$$F^-(\tau,\tau_{\text{up}}) = -1-\beta^2+\ln((\tau-\tau_{\text{up}})\cdot\tau_{\text{up}}) + \frac{\tau}{\tau-\tau_{\text{up}}} + \frac{1}{\gamma^2}\cdot\left(\frac{\tau_{\text{up}}^2}{2} + (2\tau+1)\cdot\ln\left(1-\frac{\tau_{\text{up}}}{\tau}\right)\right), \tag{4.8}$$

where for both functions $y = \frac{1}{\gamma+1}$. The energy loss of the e^- and e^+ is due to ionization of atoms in the medium. The range of electrons for different energies in different materials is shown in figure 4.2. For condensed matter and energies of several MeV, the range is on the order of several mm.

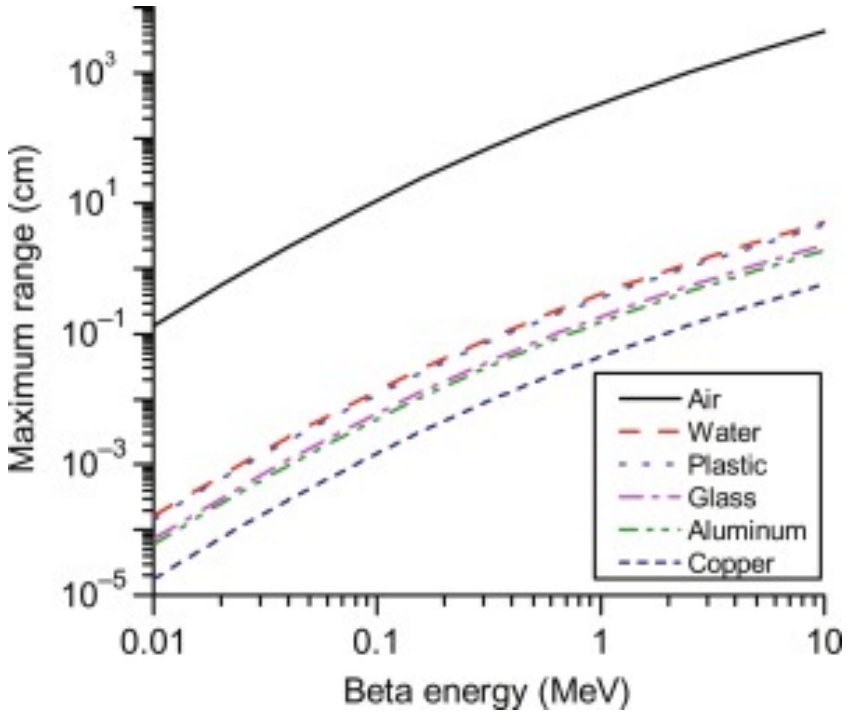

Figure 4.2: Range of electrons in different materials for different energies. For condensed matter the range is significantly less than for gaseous materials. Taken from [28].

4.2.3 Photons interacting with matter

Photons have several distinct ways of interaction with matter. These differ in their kinematics and the potential particles produced. Which interaction is the most probable depends on the energy of the photon.

The photoelectric absorption is dominant for the lower ionizing energies up to several hundred keV. In the photoelectric effect the photon is absorbed by an electron of the inner shell with the photon having enough energy to remove the electron from its bound state. The photoelectric absorption can only occur on bound electrons due to kinematics. The energy of the newly freed electron is therefore $E_{\text{electron}} = E_{\text{photon}} - E_{\text{binding}}$ and the probability for this interaction is $\propto \frac{Z^3}{E^3_{\text{photon}}}$. In figure 4.3 that shows the mass attenuation of photons for iron due to different interactions a resonance can be observed for energies just above the binding energy of the k-shell. The absorption of photons of about the binding energy is greatly increased. After the

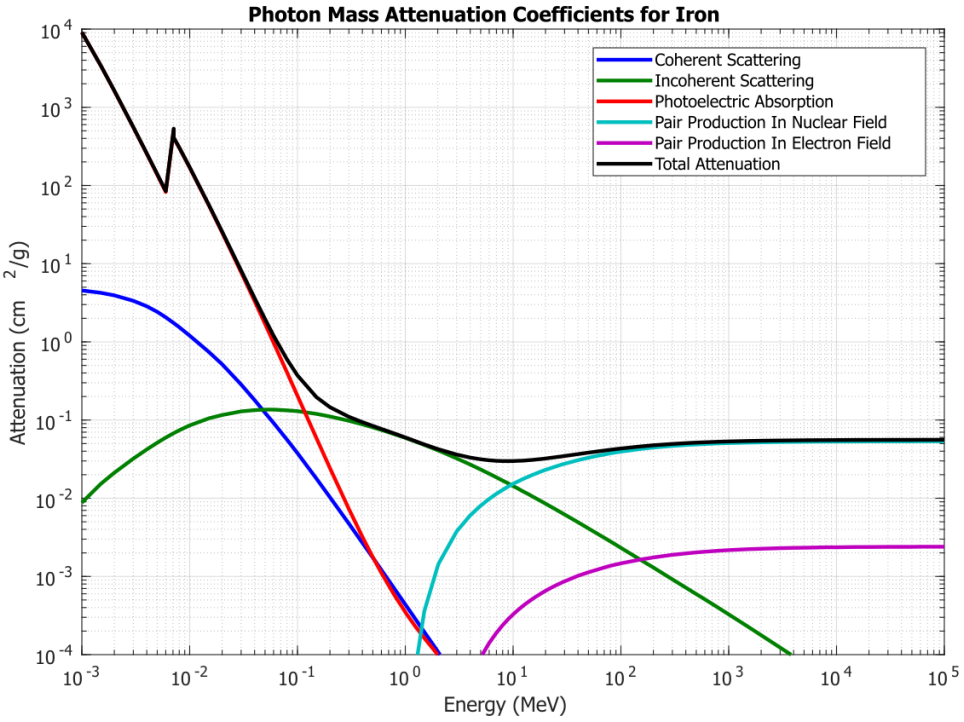

Figure 4.3: Mass attenuation coefficient for iron due to different types of photon interactions. Taken from [34].

electron is removed from the atomic shell by the photoelectric absorption, another electron from

a higher shell replaces the removed electron. In doing that it emits a photon with the difference in the binding energies between the shells, more specifically $E_{\text{X ray}} = E_{\text{vacant shell}} - E_{\text{outer shell}}$. This is dubbed a characteristic X ray since its energy depends on the respective shells between which the transision happens. This characteristic X ray can be absorbed by another electron of an outer shell (the inner ones can't be ionized because of the higher binding energy), removing that electron from its bound state as well. This is a so called Auger electron with an energy of $E_{\text{Auger}} = E_{\text{X ray}} - E_{\text{binding}}$.

Next in the energy hierarchy for photon interactions is the Compton scattering. It is the dominant photon interaction mechanism for several hunder keV up to 10 MeV. In Compton scattering, the photon transfers some of its energy onto an electron bound in an atomic shell (it also works on free electrons, but matter which surrounds us consists of mostly bound electrons). The energy transferred onto the electron can be calculated from the scattering angle of the photon as $E_{\text{photon}} - E'_{\text{photon}}$ where E'_{photon} is the energy of the photon after the interaction. This can be calculated as

$$E'_{\text{photon}}(\Phi) = \frac{E_{\text{photon}}}{1 + \frac{E_{\text{photon}}}{m_e c^2}\left(1 - \cos(\Phi)\right)} \tag{4.9}$$

with the scattering angle of the photon Φ and the electron mass m_e. The energy of the electron after scattering can then finally be calculated as $E'_{\text{electron}} = \Delta E_{\text{photon}} - E_{\text{binding}}$. The probability for this interaction is $\propto \frac{1}{E_{\text{photon}}}$.

Beginning at even higher photon energies there is the pair production, where the photon transforms into an electron positron pair. Similar to the photoelectric absorption, a massive particle is necessary to absorb the recoil of the photon. The necessary energy for this interaction is $E_{\text{thr}} = 2\dot{m}_e = 1022\,\text{keV}$, so the mass of the particles to be produced. Excess energy is shared between the recoil particle, the electron and the positron, but its total amount is given as $E_{\text{kin, tot}} = E_{\text{photon}} - E_{\text{thr}}$. In figure 4.3 it can be seen that the interaction happens for lower energies already if a nucleus is the recoil particle. This is due to the heavy mass of a nucleus, making the energy needed for recoil in the process negligible. Pair production becomes the dominant mechanism of interaction for photon energies above 10 MeV. The interaction probability is $\propto Z \ln(E_{\text{photon}})$.

The photon interaction with matter with the highest necessary energy is the photodisintegration, in which the photons break up bound states in a nucleus splitting it into protons, neutrons, α particles or heavier nuclides depending on the initial nucleus. This starts to happen at around 10 MeV.

4.3 Pulse shape discrimination

Depending on the topology of an event, the pulse shapes look very different. This allows the classification of SSEs and MSEs. A single site event is, as the name implies, formed by a charge cloud generated closely around a single point of the detector. As described by the Shockley Ramo theorem this charge cloud drifts to the the readout electrodes of the HPGe detector. The drift produces a single current pulse, resulting in a step shape of the total charge over time as the integral of this current. For a multi site event on the other hand multiple of these charge clouds are produced around different points in the HPGe detector. This results in multiple charge clouds drifting, producing multiple current pulses at the readout. For the same total charge (or energy) the amplitude of the highest current pulse of a MSE has to be smaller than the amplitude of the current pulse of a SSE. This is true since the same current has to be split into two pulses. Examples for both SSE and MSE can be seen in figure 4.4. The neutrinoless

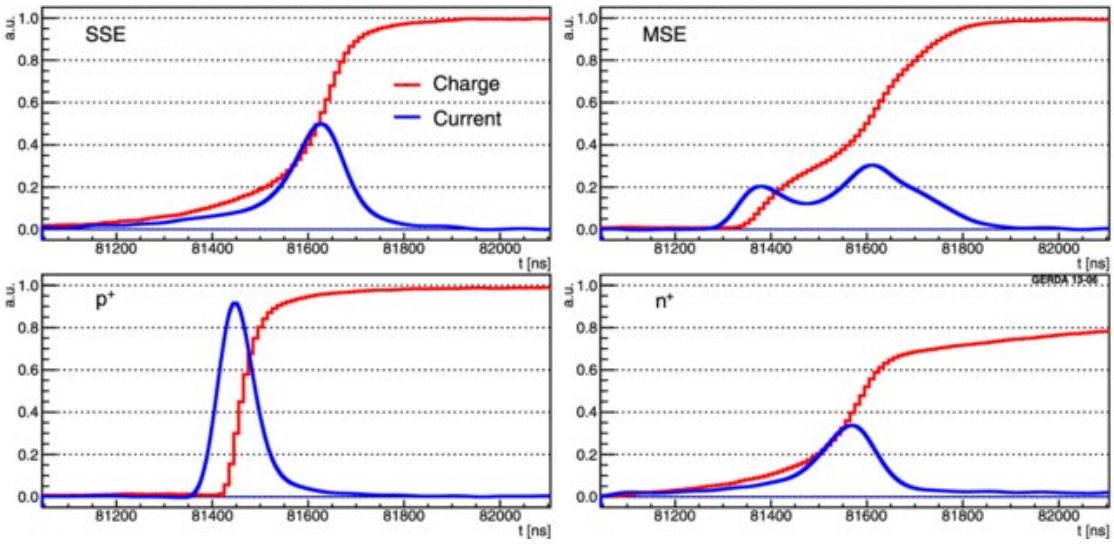

Figure 4.4: Examples of pulse shapes for SSEs and MSEs as well as events close to the n^+ and p^+ electrodes of a Broad Energy Germanium (BEGe) detector as used in GERDA. Taken from [3].

double beta decay would produce two electrons with very short reach (several 10 μm) in the HPGe detector. The free charges produced in this short range can be considered a single charge cloud, making the neutrinoless double beta decay in fact a SSE. To filter out some background events for the decay (MSE), the ratio between amplitude of the current pulse and the energy can be exploited. The ratio A/E between current amplitude A and total energy E can be calculated

and the result can be displayed in a 2D histogram, as is shown for example in figure 4.5. The horizontal line around the value of 1 is the SSE band, made from e.g. single Compton events. A double escape line from the 2.6 MeV γ line of Th as the perfect SSE can be seen as a bright dot in the band around 1592 keV. For the other γ lines a considerable leakage below the SSE band can be observed. This leakage stems from absorption in the detector in multiple locations, as in a multi Compton scattering. Events above the SSE band are considered to be from α radiation as the ionization behaves different for α particles than for electrons (both from β radiation and Compton scattering). To reduce the background in an actual neutrinoless double beta decay experiment, one considers only the events lying in the SSE band. This technique can reduce external backgrounds like α and γ radiation considerably. To further improve the knowledge about this method, an increasing number of pulse shape simulations for HPGe detectors are used. To further validate these simulations, pulse shape measurements with known location of interaction can play a crucial role.

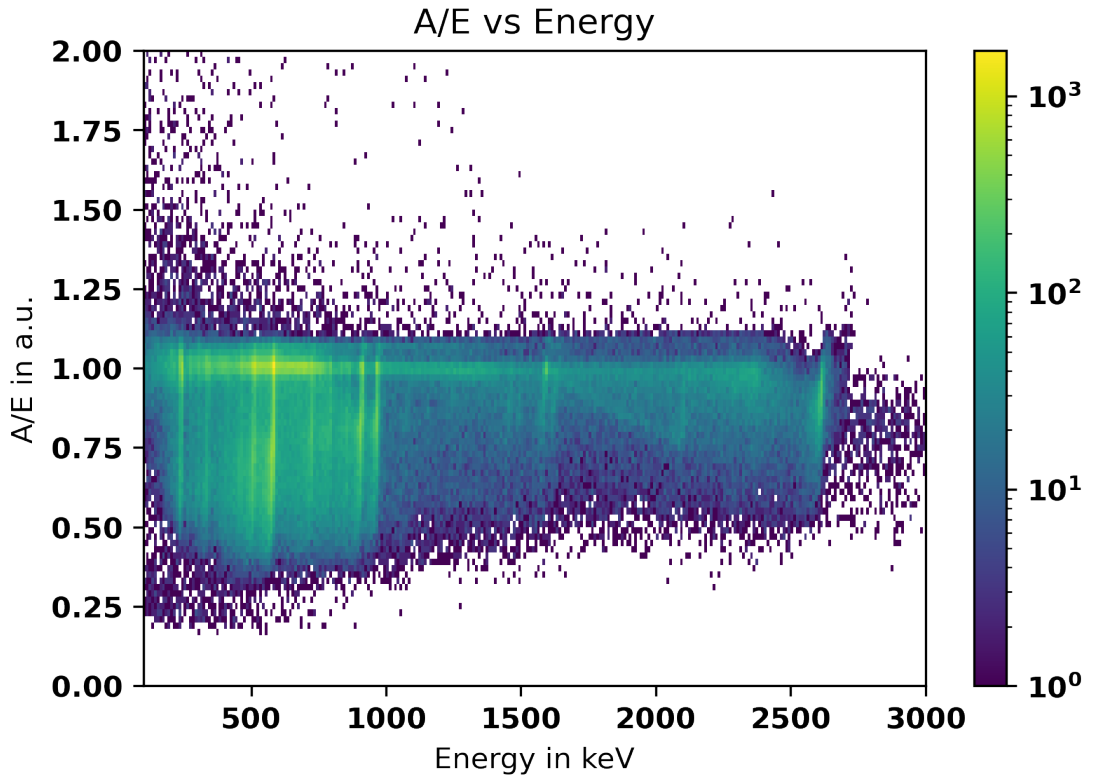

Figure 4.5: A/E distribution of a calibration measurement performed with a ^{232}Th source using a ICPC HPGe detector.

5

Positron emission tomography

"I'm taking all the negatives in my life, and turning them into a positive."

- Pitbull, *American singer*

Opposed to other medical imaging methods, like magnetic resonance imaging (MRI) or computer tomography (CT), positron emission tomography (PET) visualizes not the tissue and bones but the metabolism of the tomographed organism. PET relies on radioactive tracers decaying via a β^+ decay, producing a positron e^+ (and also a electron neutrino ν_e which is irrelevant in this case). This radioactive tracer is chemically attached to energy suppliers for metabolism like glucose and will therefore spread in the body proportional to the energy consumption of the tissue. This is useful for example in the imaging of cancer, which often has increased energy consumption compared to the surrounding tissue. This chapter will cover the physical properties of the detector elements of a PET scanner and the image reconstruction separately.

5.1 Physical properties of PET detector elements

The signature for a single event in PET are two γs with an angle of 180° between them and an energy of 511 keV each. These γs emerge from the annihilation of the e^+ with a e^- from the bodily tissue. Between its production and its annihilation the positron can only travel on the order of μm depending on its energy [26] as can be seen in figure 5.1. As soon as the e^+ thermalizes, it annihilates with a e^- of the body producing the two characteristic back-to-back γs with energies of 511 keV each. These two gammas are then detected by an arrangement of

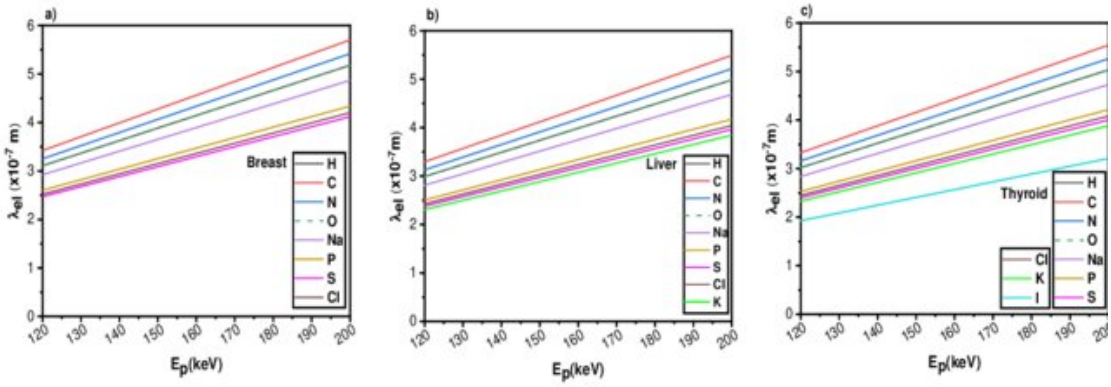

Figure 5.1: Mean free path of positron as function of energy for several bodily tissues. Taken from [26].

scintillation detectors around the tomographed body or body part. These detector elements need to fulfill several requirements in order to be suitable for usage in PET. Firstly they have to have good efficiency in γ detection, meaning high atomic number Z and high mass density are necessary. The interaction cross section for γs strongly depends on Z and the density measures how tightly packed the protons in the scintillator volume is. Also the energy of the γ has to be recorded with a certain precision to make sure the γs did not scatter beforehand, which would eliminate the 180° angle between them. This translates to a high light yield for the scintillator, since for Poissonian processes like scintillation the uncertainty in the number of produced photons produced for a given deposited energy N_γ is given as $\sigma_{N_\gamma} = \sqrt{N_\gamma}$. Because of the proportionality between deposited energy and number of produced scintillation photons this translates directly to the energy resolution.The energy resolution ΔE is proportional to $\frac{\sigma_{N_\gamma}}{N_\gamma} = \frac{\sqrt{N_\gamma}}{N_\gamma} = \frac{1}{\sqrt{N_\gamma}}$ which becomes smaller as N_γ increases. Another important property of the scintillator material is the

attenuation coefficient μ used in Lambert-Beer's law

$$I(x) = I(0) \cdot e^{-\mu \cdot x}. \tag{5.1}$$

$I(x)$ denotes the intensity left of a starting γ radiation intensity $I(0)$ after passing through matter with a linear attenuation coefficient μ for a distance x. A small attenuation coefficient means that only a small fraction of γ radiation will be absorbed per unit of length while a large attenuation coefficient means a large fraction of γ radiation will be absorbed. For compact PET setups (required for e.g. PET-MRI inserts for simultaneous PET and MRI) scintillators with higher attenuation coefficient can be built thinner while still absorbing most of the produced γs. To record an entire PET event, both produced γs have to be recorded, being flagged as related to each other by their coincidence in time. To be able to achieve high rates to minimize the measurement times for patients, the light in the scintillator should be produced with a small decay time. This way the probability of two events overlapping in time is greatly reduced. Overlapped events cannot be resolved properly and often render all events involved useless because their energy and timing cannot be properly determined. This is sketched in figure 5.2. In order to keep this advantage of short decay time constants, the photodetectors used to measure the light need to have fast response times. Otherwise the signals overlap each other again due to the long decaying tail of the electrical signals coming from the photodetectors. These requirements for the individual elements of the detectors elements are collected in table 5.1. The best scintillation crystal with these requirements for usage in PET scanners is a still evolving topic. Since in the PET scanner concerned in this work the used scintillator is lutetium oxyorthosilicate (LSO), the properties of LSO will be compared to those of sodium iodide (NaI) as a very common scintillator and bismuth germanate (BGO) as a scintillator used previously in PET scanners. The results of this comparison is shown in table 5.2 and the values are collected from [25, 24, 20]. As can be seen in the table, LSO is about the double density of NaI and about the same as BGO. The atomic numbers for all scintillators are comparable, with LSO being in the middle of the other two in this regard. NaI has the lowest attenuation coefficient with LSO only being shortly behind BGO. LSO has by far the fastest decay constant producing by far the shortest light pulses. Regarding relative emission intensity LSO is a bit lower than for NaI but still significantly higher than for BGO. The emission wavelenghts are very similar for NaI and LSO, BGO is a bit further off. In total LSO is a suitable material for the use in PET scanners.

One detector element in a PET scanner consists of a scintillator block and several photodetectors.

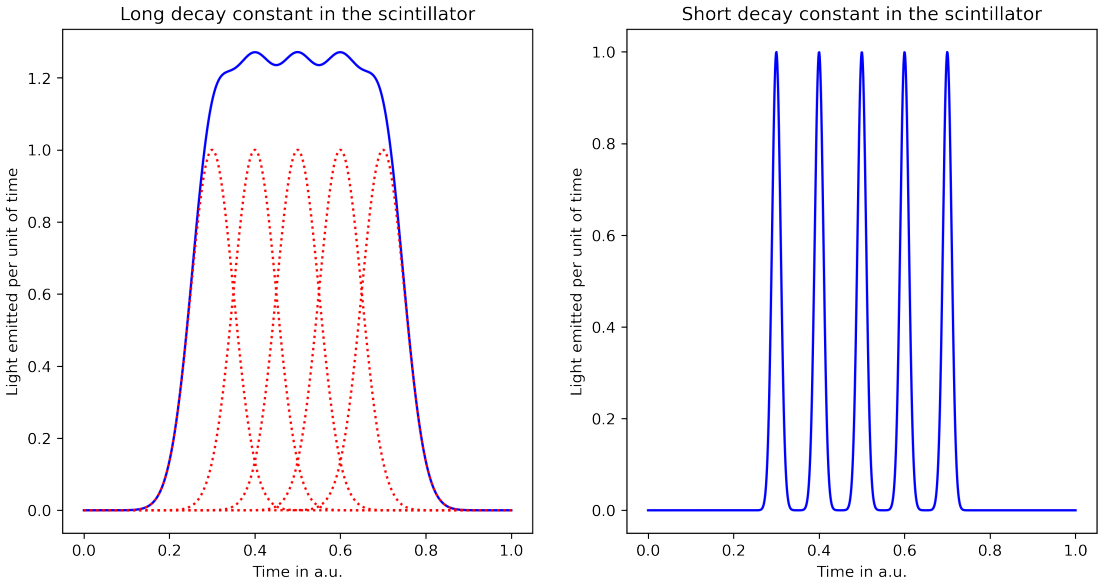

Figure 5.2: Left: Train of scintillator light pulses with long decay constant. The individual pulses are plotted as red dotted lines and sketch the individual energy depositions of multiple events happening shortly after another. The blue line is the sum of the individual light pulses and sketchs what a photo detector coupled to the scintillator would see. Right: Train of scintillator light pulses with short decay constant. Opposed to the case for long decay constants, the pulses are clearly separable in time and can therefore be accredited to different events happening one after another.

The scintillator block has several cuts of varying depths. The entire crystal and also the cuts are covered in reflective foil to increase the effective light yield. On one side the scintillator block is coupled to multiple photodetectors, in the easiest setup four detectors with one in each corner. The coupling happens via a light guide to compensate for a possible mismatch between scintillator size and photodetector surface area. The cuts together with the multiple photodetectors allow for a spatial resolution of the photon interaction smaller than the scintillator block size. This scheme is known as an Anger camera or Anger logic invented by Hal Anger [1]. The cuts into the scintillator blocks make them pseudo-pixelized as sketched in the left part of figure 5.3. The depth of the cuts is selected so that light produced in the scintillator part opposite to the photodetectors is shared by the photodetectors dependent on the pseudo pixel in which it was created. Relative x and y coordinates of the hit pseudo pixel are calculated by weighting positive and negative directions with the amount of light in the detectors of the respective direction. Considering the coordinate system and labeling in figure 5.3, the x and y coordinates of the hit pseudo pixel can

Table 5.1: Collection of the requirements on the individual components of a PET detector element.

Detector element requirement	**Reason for the requirement**
High Z and high density of scintillator	Interaction cross section for γs strongly dependent on Z, improves detection efficiency
High light yield of the scintillator	Good intrinsic energy resolution of the scintillator, makes sure only un-scattered γs are considered, using an energy cut
High linear attenuation coefficient of scintillator	Detector elements can be built thinner with same detection efficiency, makes scanner usable in small volumes as inside of an MRI
Short decay time of the scintillator	Light pulses from scintillation should be short, making it possible to resolve multiple pulses occuring in a short time for higher fraction of usable events
Fast response with short decay tail of the photodetector	Slow photodetector is not able to take advantage of the previous requirement of only short light pulses

Table 5.2: Collection of porperties of the common scintillator NaI and BGO which was used in early PET scanners, as well as LSO which sees increasing use in PET scanners. Data taken from [25, 24, 20].

Crystal	**Density** ($\frac{g}{cm^3}$)	**Effective atomic number**	**Linear attenuation coefficient** ($\frac{1}{cm}$)	**Decay constant** (ns)	**Relative emission intensity (% NaI)**	**Emission wavelength**
NaI	3.67	51	0.34	230	100	410
BGO	7.13	75	0.91	300	15	480
LSO	7.40	65	0.82	40	75	420

be calculated as

$$x = \frac{(A+B)-(C*D)}{A+B+C+D} \text{ and} \tag{5.2}$$

$$y = \frac{(B+D)-(A+C)}{A+B+C+D}, \tag{5.3}$$

with A, B, C and D denoting the amount of photons recorded by the respective photodetector. The depth of the cuts for the pesudo-pixelization is empirically determined by the crystal

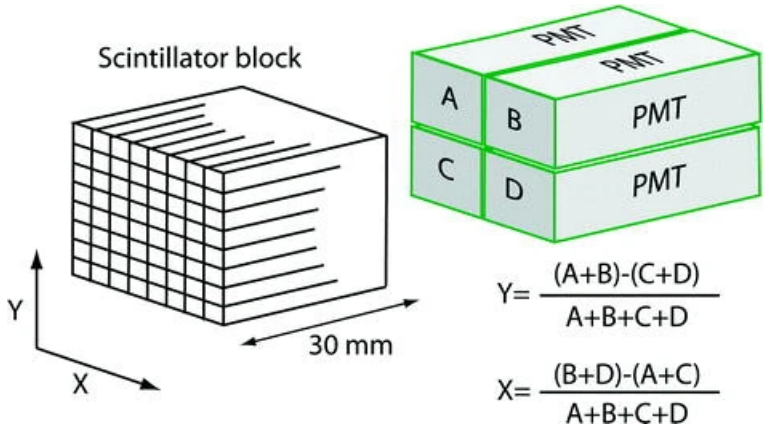

Figure 5.3: Sketch of the coupling of a pseudo-sliced scintillation crystal to four PMTs. The scintillation crystal is pseudo-sliced so that the light is distributed to the four PMTs proportional to the respective relative distances. The coordinates of the hit pixel are then calculated by weighting the PMT positions with the light intensity they recorded as is described by the inscribed equations in the sketch. Taken from [32].

manufacturers for optimal position resolution. For the PET scanner used in this work a grid of $15 \cdot 15 = 225$ pixels can be used with only 4 readout channels for the entire array.

To maximize the coverage of solid angle with detectors PET scanners for e.g. small rodents, the detector elements are arranged in multiple rings on a cylindral shape with the scintillators looking inward. This way the animal or person can be introduced into the sensitive volume via the top or bottom of the cylinder. Different arrangements for single body parts like a sphere for head or breast are also possible, although more complicated in the image reconstruction. A 3D model of a ring of a PET scanner can be seen in figure 5.4.

5.2 Image reconstruction

Events in a PET scanner consist of two energy depositions in different scintillators with respective energies close to 511 keV. The connecting line between the hit pseudo pixels marks the region where the event can have happened. A single event is of course not enough to produce an image of the metabolism, so patients get injected with high activities of radioactive tracer, producing millions of events in a short time. These events emit their γs isotropically, hitting all the detectors around the body. When looking at the source distribution in a given angle relative to a defined

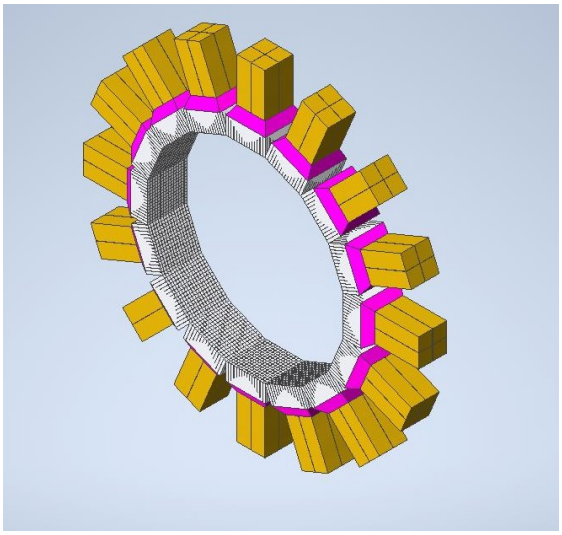

Figure 5.4: 3D model of a ring of detector blocks for a PET scanner. The ring consists of 16 detector blocks with 15×15 pseudo pixels each. Shown in white are the scintillator blocks with the partial slices visible. The lightguide between scintillator and photomultiplier is shown in magenta. The four PMTs for each scintillator block are shown in gold.

0° axis, the amount of all events with connecting lines between detectors perpendicular to the projection axis can be plotted as a function of distance from the origin of the tilted axis. If this is repeated for multiple angles, it produces a set of intensity projections along different angles. This set can be combined into a so called sinogram, a figure containing the intensity projections along the axis in the form of a two-dimenstional histogram (with the intensity as the number of events recorded). The name stems from the sine-like shape of this distribution for a point-like source (it is still called a sinogram for more complicated distributions). The generation of one slice of a sinogram can be seen in figure 5.5. The product of making the projection for a more complicated source distribution can be seen in figure 5.6. The procedure generating the sinogram is the so-called Radon transform in mathematics. The Radon transform is reversible, so the original source distribution can be recovered by the inverse Radon transform. The quality of the reconstructed source distribution depends on the number of projections onto tilted axes performed since it is continuous in reality but only a limited number of projections can be performed. An example for the differences of results from different numbers of projections can be seen in 5.7. The number of projections that can be reasonably made is governed by the event statistics and the spatial resolution. For low statistics there may be "holes" in the sinogram, i.e. angles for which no projection exists because of low total number of events. This yields a limit

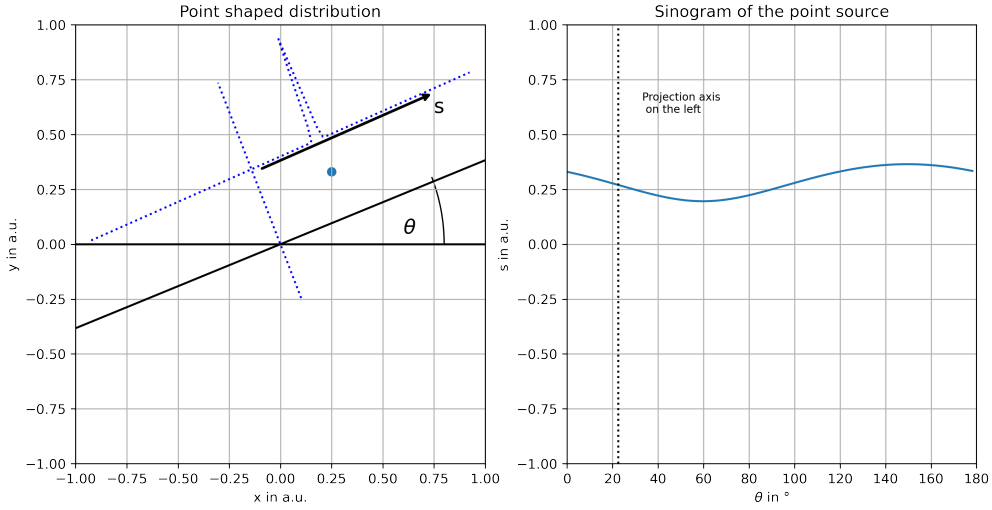

Figure 5.5: Left: Single point source distribution. One observation axis x' with angle θ relative to the x axis is sketched together with the axis along which the projection happens. Right: Sinogram for the point source. This sinogram is obtained by performing the measurement sketched on the left for many angles. The position of the measurement shown in the left is marked by the dotted line.

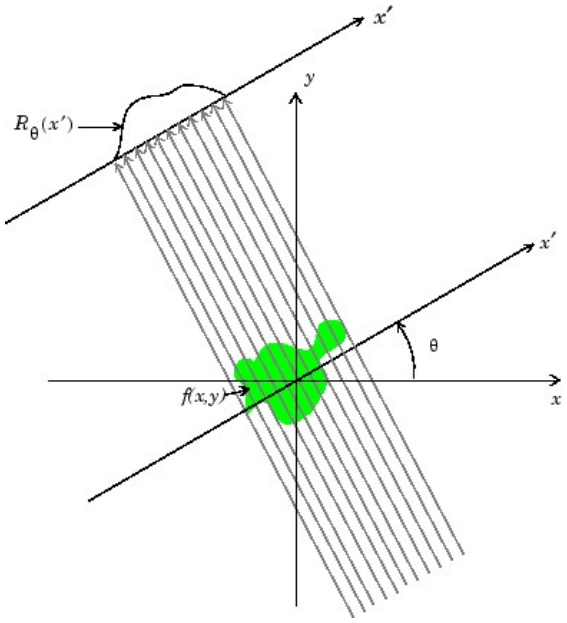

Figure 5.6: Generating the intensity projection for more complicated source distribution. The sinogram is again obtained by repeating this projection procedure for many angles. Taken from [37]

for number of sensible projections by requiring there to be no holes in the sinogram. The spatial resolution has the same effect in an opposite way. For lower spatial resolution, events with a wider possible spread of angles are recorded in the same pixels. This again limits the number of sensible projections because too fine angle granulation consider the same events for adjacent angles.

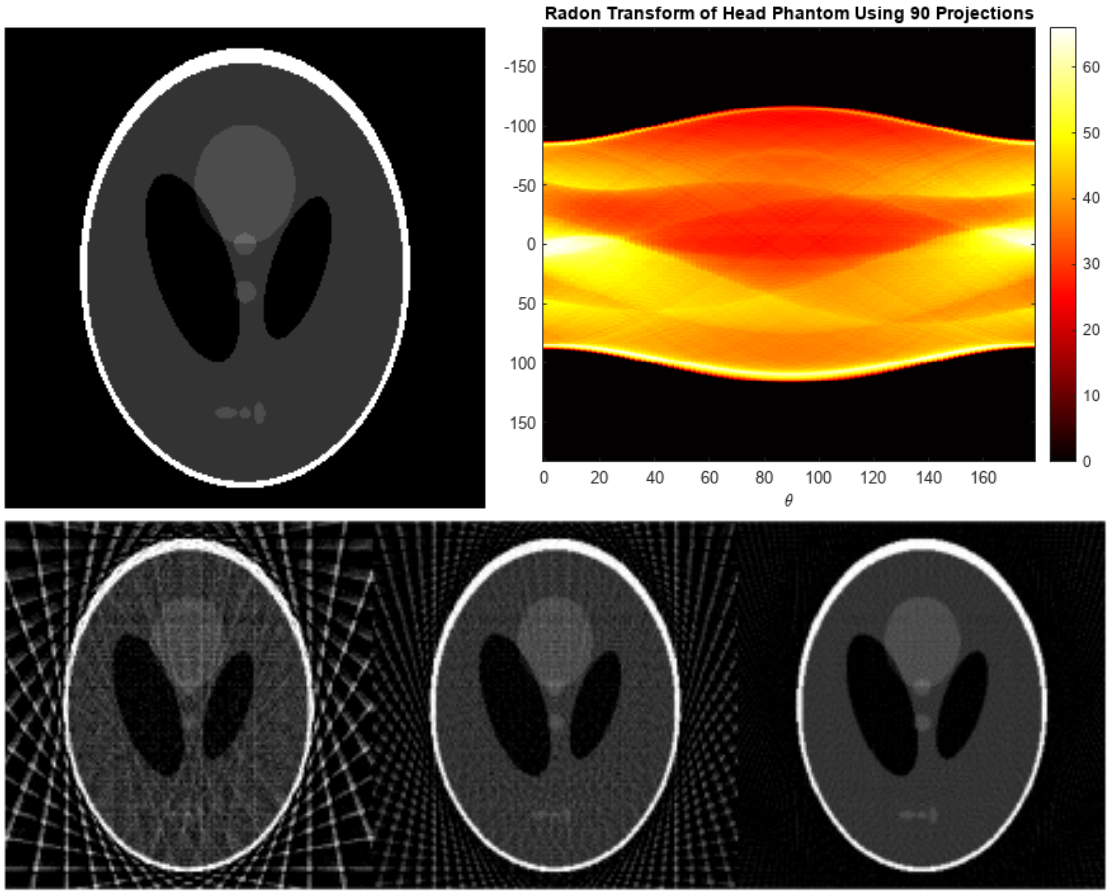

Figure 5.7: Top left: Calibration phantom from which a sinogram is constructed. Top right: Sinogram built from the phantom with 90 projections. Bottom: Reconstruction of the initial image via inverse Radon transfrom. The reconstructions from left to right are performed with 18, 36 and 90 projections. All taken from [13].

6

Setup of the test stand

"It's alive! It's alive!"

- Dr. Frankenstein, *Frankenstein (1931*

The base of the test stand is a prototpype of a PET-MRI insert for small rodents like rats and mice. It was built and evaluated over the course of a PhD thesis at the Werner Siemens Imagin Center in Tübingen and was generously offered for this work. A brief overview of the PET scanner will be given here while a more detailed description can be found in the respective thesis [19]. Also the properties of the used HPGe detector will be briefly discussed.

6.1 The PET scanner

The PET scanner consists of 3 such rings as are sketched in 5.4, with 16 detector blocks per ring. Each of the detector blocks made from LSO with a square front has a size of 24 mm × 24 mm and a

thickness of 10 mm. The pseudo pixels cut into each block have a front size of 1.51 mm × 1.51 mm without pitch and 1.58 mm × 1.58 mm with the pitch of 0.75 mm. The exit surface (towards the photodetector) is polished, while the other are diffused. The blocks are wrapped with Vikuiti™ Enhanced Specular Reflector made by 3M. Each detector block is coupled via a lightguide to its own APD array with an active area size of roughly 19 mm × 19 mm. A picture of a scintillator block coupled to an APD array can be seen in figure 6.1. Opposed to the most simple case discussed in 5, the array consists of 3×3 photodetectors instead of 2×2 photodetectors. To still use the Anger logics as described, the APDs are grouped into 4 groups as shown in figure 6.1. The intensities A, B, C and D as described are then calculated as

$$A = A1 + 0.5 \cdot A2 + 0.5 \cdot B1 + 0.5 \cdot B2, \tag{6.1}$$

$$B = A3 + 0.5 \cdot A2 + 0.5 \cdot B3, \tag{6.2}$$

$$C = C1 + 0.5 \cdot B1 + 0.5 \cdot C2 \text{ and} \tag{6.3}$$

$$D = C3 + 0.5 \cdot B2 + 0.5 \cdot B3 + 0.5 \cdot C2, \tag{6.4}$$

with the intensities of the single APD elements named according to the labels of 6.1. With these definitions the locations of the energy depositions can be calculated as discussed. The APDs are connected to dedicated front-end electronics, including a preamplifier. A picture of the assembled PET scanner can be seen in figure 6.2. For use in medical environments, the PET scanner is

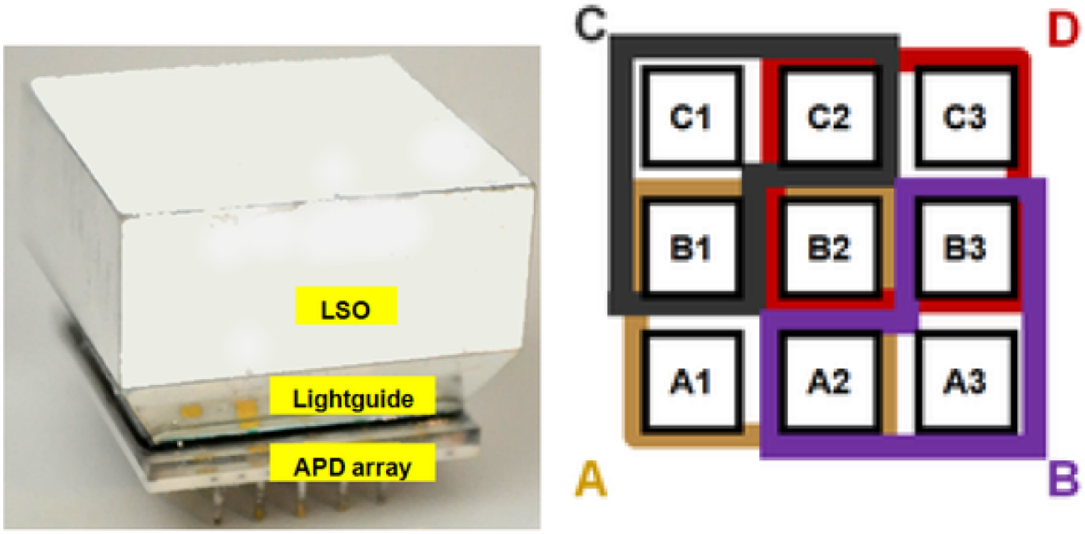

Figure 6.1: Left: Picture of a scintillator block coupled to an APD. Right: Sketch of the grouping of the APDs in the array. Both taken from [19].

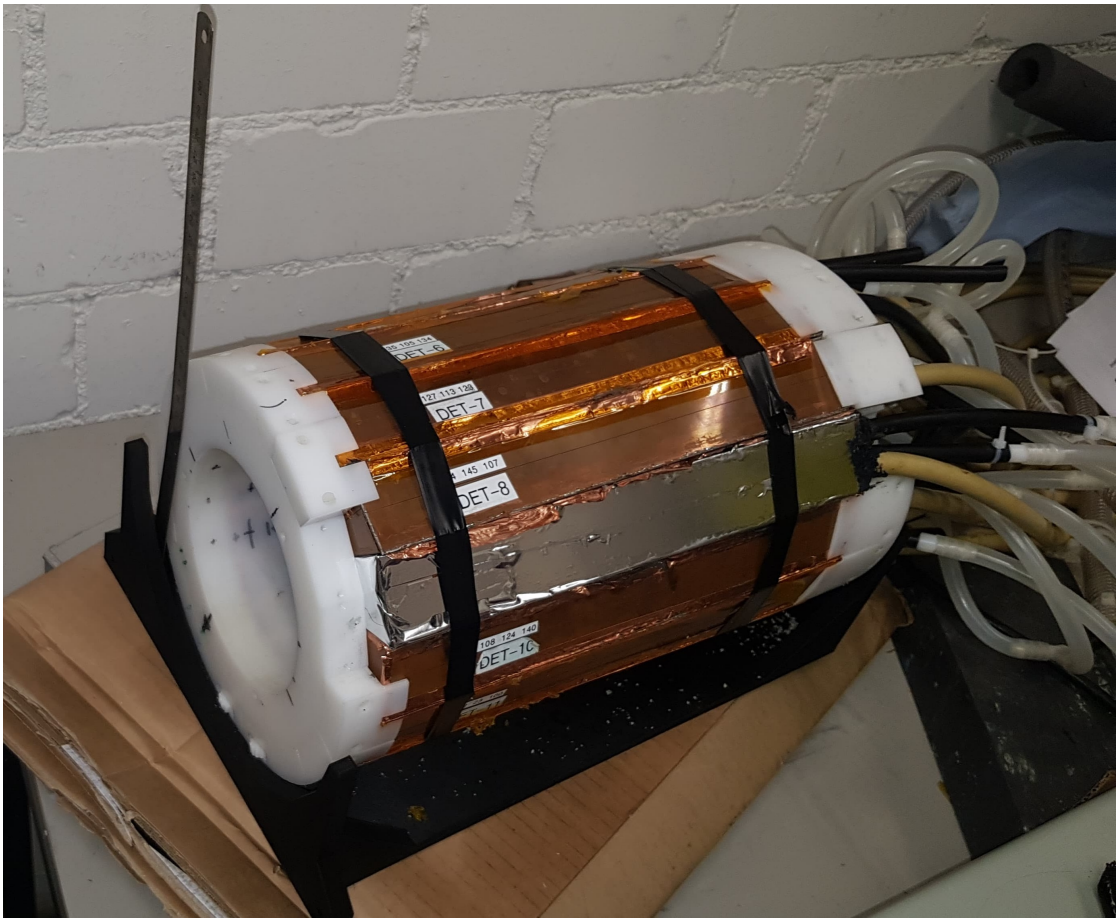

Figure 6.2: Picture of the PET scanner. The metal ruler inserted for scale has a length of 30 cm.

connected to dedicated readout electronics (Quicksilver made by Siemens). This unit carries out the digital pulse processing and produces a list of events meeting given energy and timing limits. Every event consists of the hit detector blocks, the respective intensity distributions and a timestamp. With dedicated readout software sinograms are produced from this data as described before. The downside of these dedicated electronics however is that it produces no trigger signal if an event meets the specifications. The readout of the HPGe detector can therefore not be triggered by a PET scanner event. The events could still be reconstructed if the readout of the HPGe detector is self-triggered and then events are connected via the timestamps. This however would still rely on the processing of the Quicksilver electronics which are a black box due to being a trade secret of Siemens. To overcome both of these issues at once, the decision was made to use the PET scanner with its built-in preamplifier with a CAEN V1740D digitizer with 64

input channels (matching 16×4 channels from one ring of the PET scanner). To optimize the use of the dynamic range of the digitizer, the signals of the grouped APDs are amplified using a OPA4820ID quad operational amplifier by Texas Instruments. This part is used throughout the front-end electronics of the PET scanner, so it was used to not introduce further systematics. A wiring diagram as well as a picture of the amplifier circuit can be seen in figure 6.3. With

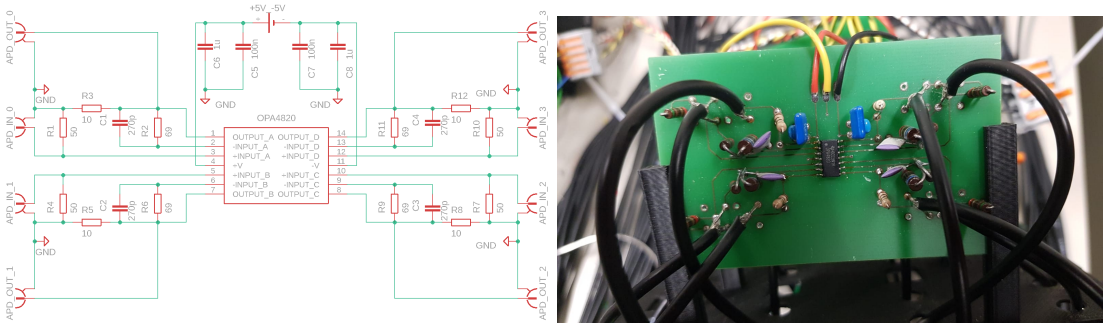

Figure 6.3: Left: Wiring diagram of the used amplifier circuit. The gain of the circuit is $g = 1 + \frac{69\,\Omega}{10\,\Omega} \approx 8$. Right: Picture of a finished amplifier circuit. The empty board was manufactured by Multi Circuit Boards and then assembled at the University of Tübingen.

the electronics in place, a calibration of the single detector blocks was carried out. For that a ^{22}Na source was positioned in front of each detector block and data was recorded for 10 minutes. A picture of the source can be seen in figure 6.4. To determine the intensity from a waveform,

Figure 6.4: Picture of the point-like ^{22}Na source. It has an activity of about 33 kBq and was manufactured by Eckert und Ziegler.

several operations are performed on the recorded waveforms. First, the baseline of the waveform

is determined as the mean of the first 100 samples of the waveform made from 384 samples. The determined baseline is then subtracted from the waveform, as shown in an example in figure 6.5. The next step to calculate the energy contained in the waveform is to restore the

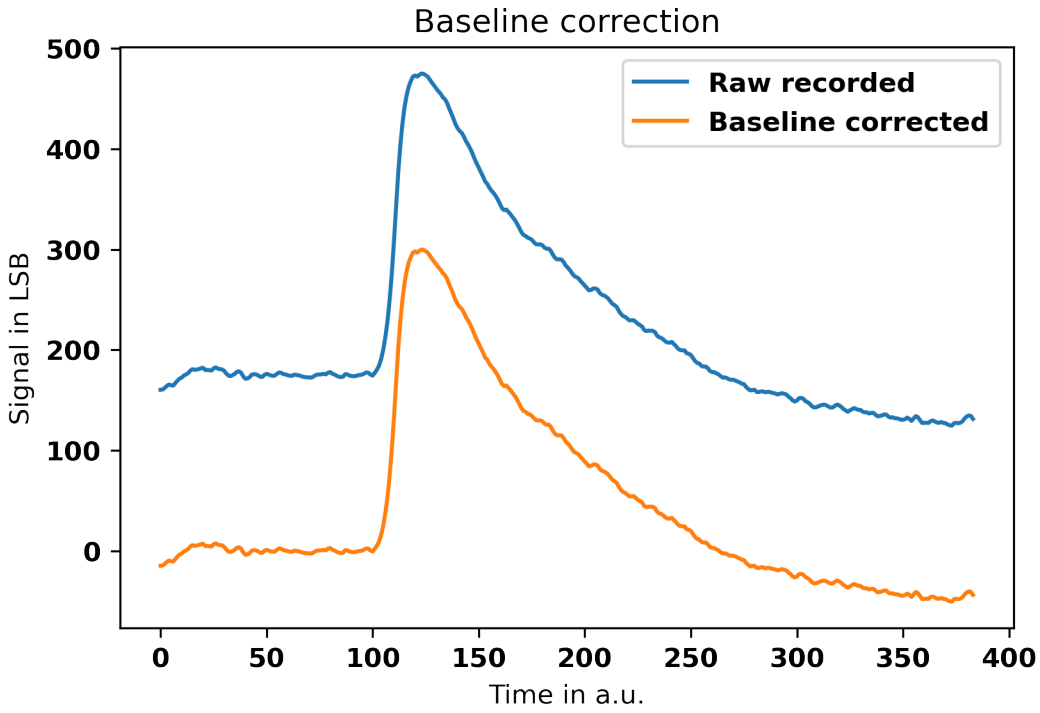

Figure 6.5: Baseline subtraction in a waveform of the PET scanner. The baseline is calculated as the mean of the first 100 samples and then subtracted from the waveform.

physical shape of the waveform. In the preamplifier the current produced in the photodiode is collected and charges a capacitor. The collected charge is the proportional to the voltage on the capacitor which is in turn digitized by an ADC. To reuse the capacitor for another measurement operation it has to be cleared of charges. This is often realized by a large resistor connecting the capacitor to ground. The resulting signal is the product of a fast limited exponential growth from charge collection and a slow exponential decay by discharge through the large resistor. While handy for recording data, this hides the exact pulse height since the capacitor immediately starts discharging and some charge has already left the capacitor when the voltage reaches its peak. The correction for this feature of the preamplifier can be realized with a pole-zero correction. Mathematically , this correction multiplies the poles in the transfer function of the preamplifier with zeros to cancel them out. Physically, it restores the limited exponential growth shape of the

photodiode pulse charging the capacitor. As the amplifier itself can introduce even more poles in the transfer function, a double pole zero correction (two consecutive corrections) is used. In order to correctly do this, the time constant of the preamplifier has to be determined. A simple way to do this is based on a template pulse shape for the photodiodes. To produce the template 500 pulses in a calibration measurement are randomly selected. They only need to be higher than 500 LSB which is much higher than the noise level of about 25 LSB. This is done to ensure that the pulses are not dominated by noise. All selected pulses are normalised to be 1.0 at their peak. Then each all waveforms are added and the result is again normalized to be 1.0 at its peak. The correct time constants are then determined by using the built-in minimizer in the Python scipy.optimize module. A wrapper method accepting two time constants as parameter is defined. This function applies two pole zero corrections to the template function. It then returns the standard deviation of the last 150 samples of the result. This part of the template initially contains the exponential decay. For a good pole zero correction this part should be flat and the standard deviation minimal. The template and the template with the result of the minimizer applied can be seen in figure 6.6. The y scale is the same, showing that the actual amplitude of the pulse is larger than what is recorded. This approach was chosen over an analog design since the analog design would have to be iterated for every channel of the PET scanner, while this digital version had to be implemented only once but could be applied to all the channels directly. After the pole zero correction, a triangular filter with rise and fall times of 20 samples is applied. An example can be seen in figure 6.7. Finally, 3 moving average filters with a width of 10 samples are applied to the waveform. An example can be seen in figure 6.8. The integral light intensity in the waveform is then given by the height of the moving average filtered waveform. The energy of an event occuring in a scintillator block is given as the sum of the intensities of the four single channels. For an ideal setup, the amount of light detected would be the same for an energy deposition independet of whether the interaction happened in a corner of the scintillator block or in the middle (locations looking at the block from inside the detector ring). In a real world situation however the light detection efficiency is greatly reduced on the sides and in the corners of the crystal, making the energy calibration of one detector block location dependent. In clinical environments this is combatted by using a wide energy window of $200 - 600$ keV which includes all of the γs from the annihilations. In order to increase the spatial resolution efforts were made to produce an energy calibration for every single pseudo-pixel in every crystal block. This procedure is described with pictures from scintillator blocks 0 and 2 which are the worst and the best performing block respectively.

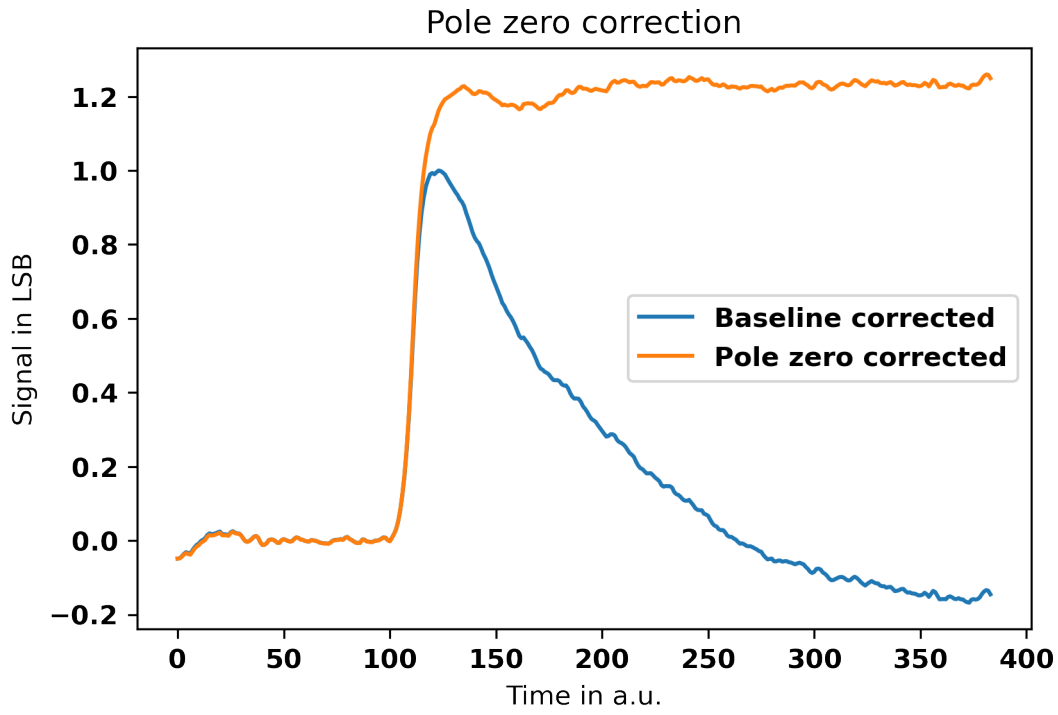

Figure 6.6: Pulse of an APD pulse and the result of a pole-zero correction applied. The pole-zero corrected waveform has the physical shape of a current pulse charging a capacitor, as is the case in the preamplifier.

The calibration starts with the data taking, 10 minutes of flood measurement from a ^{22}Na source with an activity of about 33 kBq. The single intensities and the total energies are determined for every event as described above and the xy position is calculated for every event as in equation 5.3. For a first check the coordinates are histogrammed in 2D which should clearly show the pixel positions. This can be seen in figure 6.9. As is clearly visible the pixel positions are only visible for sort of a cross-shaped region of the scintillator crystal, sparing the corners. This is due to the low light detection efficiency there, as low light intensities (in the photodetectors other than those in the hit corner) are drowned in the noise of the photodetectors. This washes out the total light spectrum as well as the pixel edges and the 511 keV can not be clearly determined. Using such a flood map , the positions of the pixels in the histogram were determined by a two-stage approach. First a pre-selection of events was made for every pixel using the method ginput (graphical input) from the Python module matplotlib. The Python method allows the user to select a pair of x and y coordinates by clicking a point in a Python figure, multiple pairs from one "clicking session" can be stored in a list. So for every 10 minute measurement of a detector

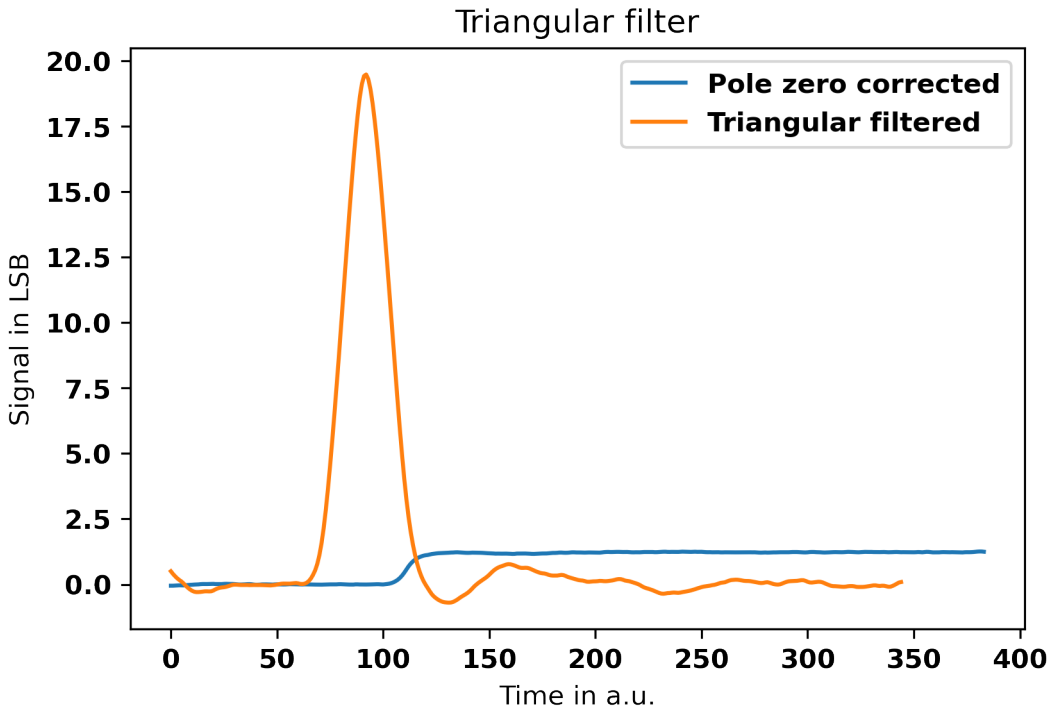

Figure 6.7: Application of a triangular filter with rise and fall time of 20 samples on a pole zero corrected pulse from the PET scanner.

block, the flood image was produced and with a fixed scheme every pixel was clicked on by eye. The used scheme was starting on the left bottom corner pixel and then go upwards column by column. The resulting list is then reshaped to 15 by 15 pairs of x and y coordinates in arbitrary units. For every pair of coordinates events with any energy in a generous radius around them are selected. The coordinates of the pixels are then refined by calculating them as the mean of the x and y coordinates of the selected events. A gaussian fit is applied for the refined x and y coordinates to determine the respective effective pixel size. One pair of fits for a pixel is shown exemplary in figure 6.14. The effective size of a pixel was then set as an ellipsis with the equation

$$\frac{x^2}{(3\sigma_x)^2} + \frac{y^2}{(3\sigma_y)^2} = 1. \tag{6.5}$$

When looking at a pixel all events falling into the ellipsis around the pixel center are considered. With these events energy spectra for every pixel can be generated. In figure 6.15 the spectral fits of the 511 keV for every pixel are shown. The gradual decrease in energy resolution for pixels towards the edges and it being worst in the corners as "double edges" can be seen by eye. A

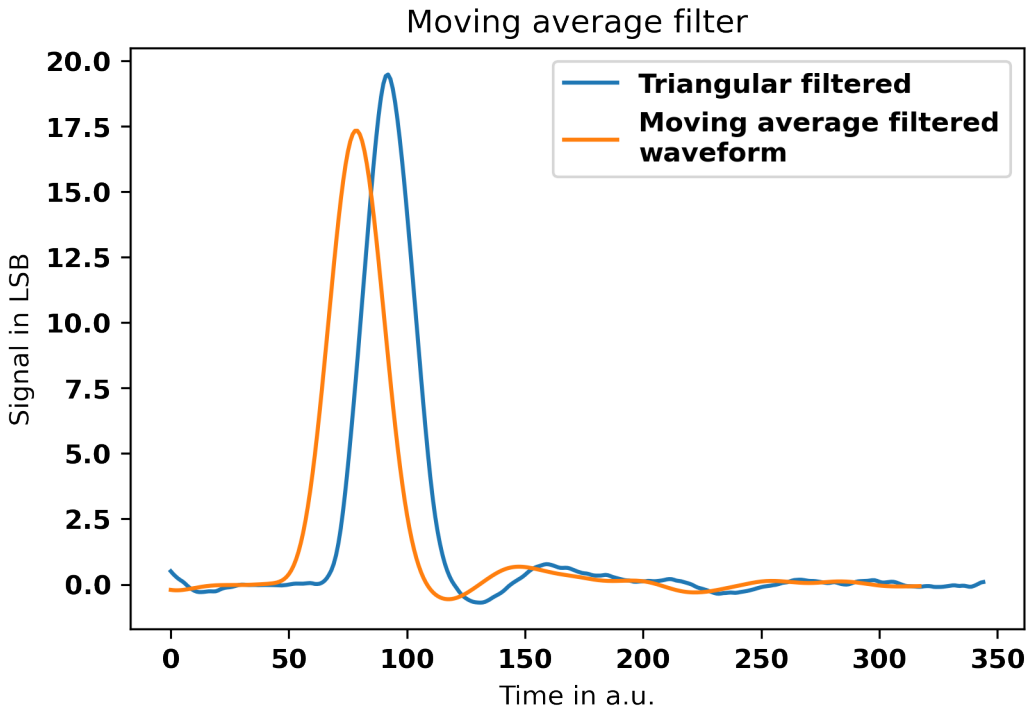

Figure 6.8: Application of 3 moving average filters with a width of 10 samples each on a triangular filtered pulse from the PET scanner.

histogram of all the obtained energy resolutions is shown in figure 6.10. This method of energy calibration for the individual pixels proved to be somewhat precise, for some pixels even besting the around 12 % FWHM energy resolution for the same PET scanner with decicated readout and data processing in the work regarding its construction [19]. Despite its advantages it proved to be inconvenient since the starting parameters for the fit of every pixel have to fine-tuned in order for the fit to converge. This holds up also for the simplest useful model consisting of a gaussian line distribution and and a linear background. To overcome this weakness, a trade-off between number of parameters and goodness of energy resolution was used. Instead of selecting events for a pixel specifically and then fitting the respective energies, the energies were radially grouped by distance from the origin and then the respective energies were fitted. This variant of slicing a detector block is sketched in figure 6.11. Since the scintillator blocks are designed as symmetric as possible this yields a good approximation for the energetic region of interest for pixels in this distance from the origin. Each block is dissected into 10 regions of different distances, reducing the number of fits that have to be performed and fine-tuned from $15 \times 15 = 225$ to only 10 fits

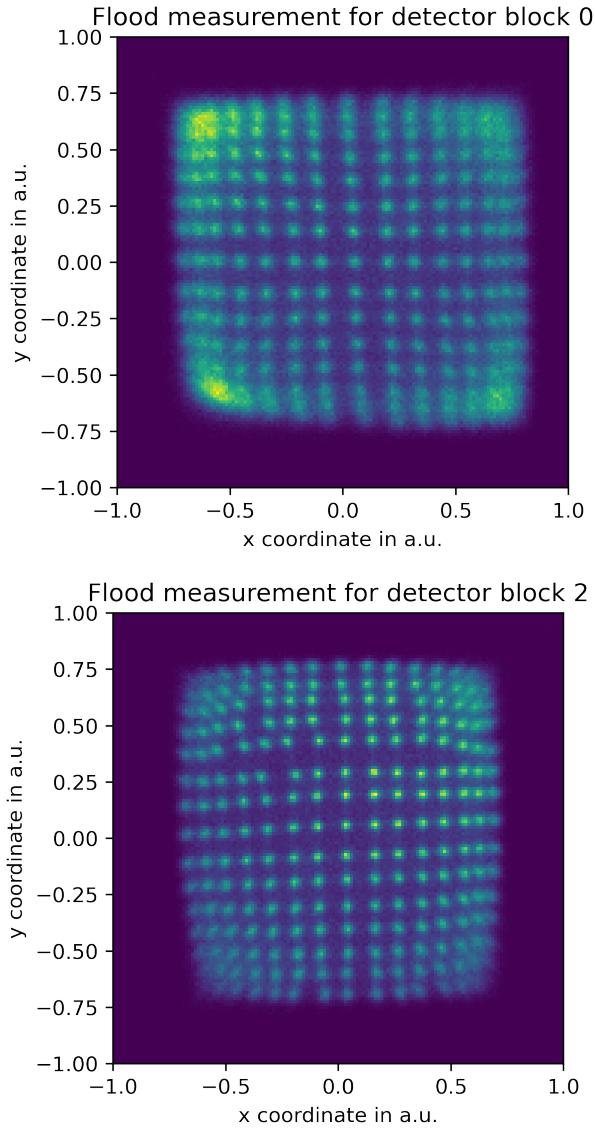

Figure 6.9: Top: Flood measurement of a ^{22}Na source for detector block 0, the worst performing one. Bottom: Flood measurement of a ^{22}Na source for detector block 2, the best performing one.

or by a factor of $\frac{225}{10} = 22.5$. A selection of these fits can be seen in figure 6.12. The resolution of the slices is shown in figure 6.13. The energy resolution of the inner rings resides around 10.3 %, therefore being comparable to that using the "single pixel" approach. Due to the increased simplicity this "radial distance" approach was used for the energy cuts. For a given pixel it was determined to which slice of radial distance it belonged and the respective limits for the energy

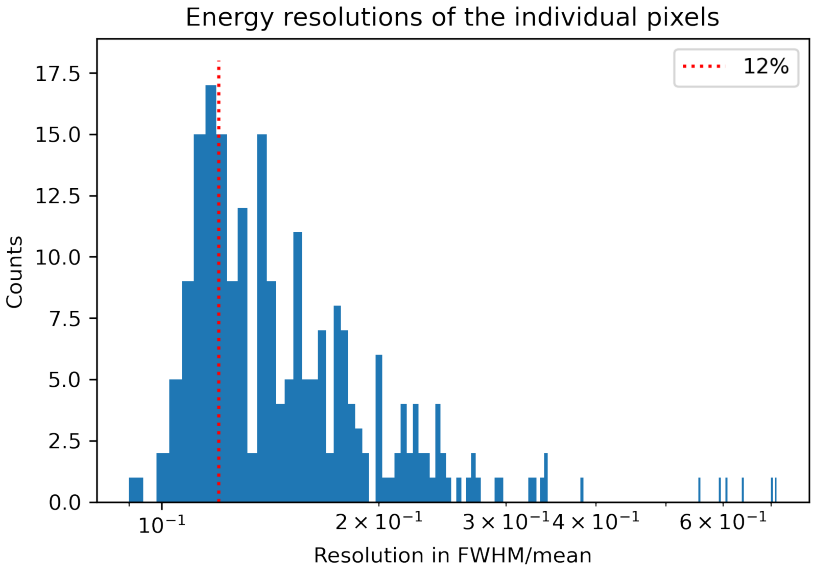

Figure 6.10: Histogram of the resolutions in FWHM/mean obtained for all pixels of detector block 14. The dotted line indicates the resolution of 12 % obtained with commercial readout and data processing.

were applied.

The arrays of pixel positions and limits together form a look-up-table (LUT) for every detector block. For every pair of arbitrary x and y coordinates the distance relative to the closest pixel is determined. If the pair is close enough, the X and Y ID of the pixel are returned, (0,0) being the bottom left, (0,14) the top left, (14,0) the bottom right and (14,14) being the top right pixels in the shown flood maps. The event is then mapped onto the physical coordinates of the determined pixel relative to the center pixel.

To finally confirm the correct operation of the scanner, a ^{22}Na source (β^+ decay) was placed inside of the PET scanner and an attempt was made to reconstruct its position. To compare the reconstruction with the real world, it is necessary to convert the IDs of a hit pixel into 3-dimensional coordinates. This is done by a two-stage strategy. The method converting the pixel ID into its 3D coordinates takes as arguments the number of the detector block in which the pixel resides and the X and Y ID of the pixel. The number of the detector block is used to select the center coordinates of the respective block surface from a LUT for the 16 detector blocks. The X and Y IDs are used to select the coordinates of the pixel relative to the block center from the aforementioned LUTs for the respective detector block. The total coordinates are then given

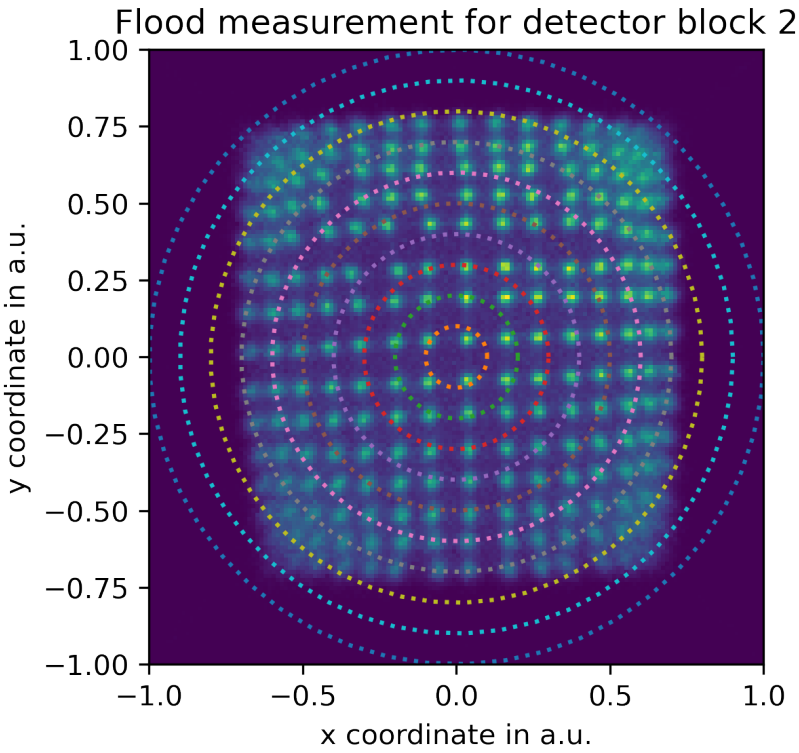

Figure 6.11: Slicing of a detector block into 10 regions of radial distances instead of pixel by pixel. This approach drastically reduces the number of necessary fits to determine the limits of integral light being considered an energy of 511 keV.

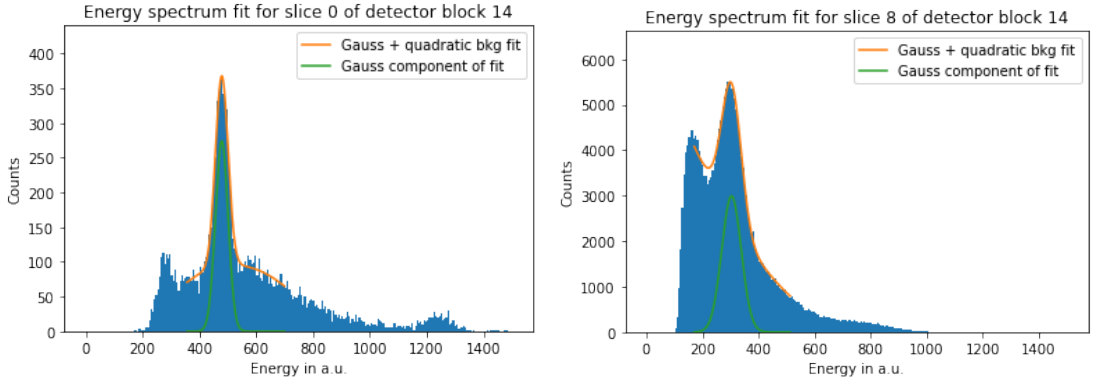

Figure 6.12: Left: Fit of the energy spectrum for the innermost radial slice, containing the most central pixels. Right: Fit of the energy spectrum for an intermediate radial slice, containing some of the outer and edge pixels.

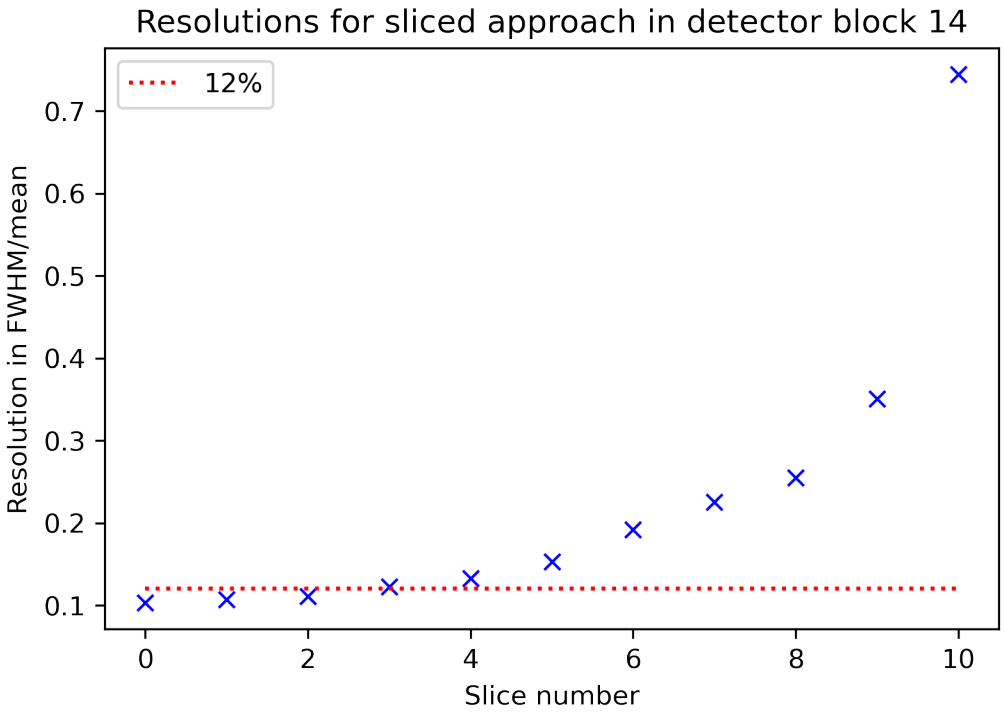

Figure 6.13: Energy resolutions in FWHM/mean obtained for the 10 radial slices of detector block 14. The dotted line indicates the resolution of 12 % obtained with commercial readout and data processing.

as the sum of the detector block center and the relative coordinates of the pixel:

$$\vec{r}_{\text{global}}(n, x_{\text{arb}}, y_{\text{arb}}) = \vec{R}_{\text{block center}}(n) + \vec{r}_{\text{pixel relative}}(n, x_{\text{arb}}, y_{\text{arb}}) \tag{6.6}$$

$$= \text{LUT}_{\text{block center}}[n] + \text{LUT}_{\text{pixel}}[n, \text{ID X } (x_{\text{arb}}), \text{ID Y } (y_{\text{arb}})], \tag{6.7}$$

with the arbitrary x_{arb} and y_{arb}, the hit detector block n, the LUT of the block surface centers $\text{LUT}_{\text{block center}}$, the LUT of the relative pixel coordinates $\text{LUT}_{\text{pixel}}$.

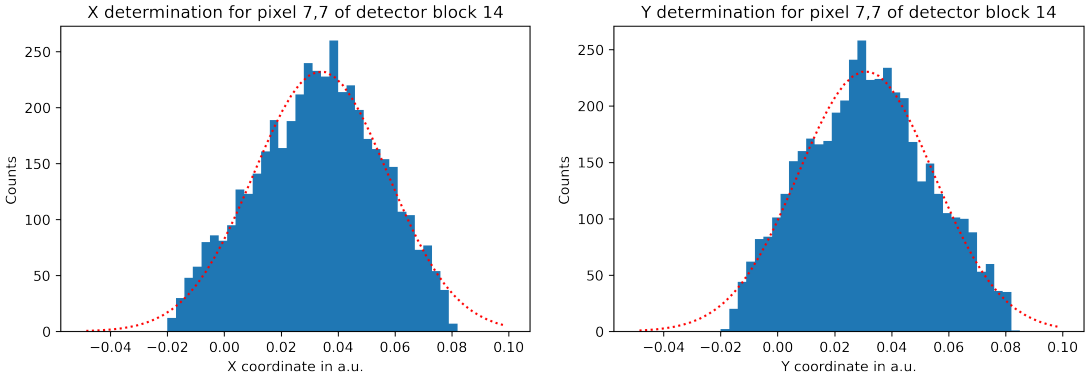

Figure 6.14: Left: Gaussian fit of the x coordinates of events close to the central pixel of detector block 1. Right: Gaussian fit of the y coordinates of events close to the central pixel of detector block 1.

The result of one of these placements can be seen in figure 6.16. As can be seen in the figure, the spatial reconstruction inside the PET scanner works well and it can be concluded that the PET scanner works as intended.

6.2 The HPGe detector

The detector used in this proof-of-principle was already characterized in previous works regarding multiple characteristics. Due to the already well known characteristics it is a promising target for further investigations, improving the understanding of the interdependence of factors like its shape, size, pulse formation and more. Because of the excessive descriptions available here only a short summary will be presented, based on one the pulse shape characterization that can be found in [36]. The used detector is an Inverted Coaxial Point Contact HPGe detector, the shape the LEGEND collaboration chose as detector design going forward. Its dimensions are collected in table 6.1. A picture of the detector in a cryostat attached to a 30 l Dewar can be seen in

figure 6.17. For the usage of the detector in the setup, an energy calibration had to be carried

Height	67 mm
Diameter	76 mm
p+ Diameter	5 mm
Inner/Outer groove diameter	26/32 mm
Bore hole diameter	10 mm
Bore hole height	39 mm
n+ thickness	1.5 mm
n+ thickness bottom	0.7 mm
Depletion voltage	3200 V

Table 6.1: Basic parameters of the used detector. Taken from [36].

out in order to ensure the desired performance of the detector as well as for event selection. The calibration was carried out using a 232 Th source with an activity of about 37 kBq. The source consists of old incandescent mantles from a time when these still contained significant amounts of thorium. It was used beforehand in lab courses and is therefore enclosed in a plastic container with a sealable tube to extract the ^{220}Rn produced along the decay chain. The radon was only used in the lab course and is not a calibration source used in this work. Instead the γ lines of ^{228}Ac, ^{212}Pb and ^{208}Tl, listed in the order they are produced along the decay chain. The literature values for the energies of these γ lines are collected in table 6.2. To determine

Table 6.2: Literature values of the γ lines used for calibration of the HPGe detector. Taken from

^{228}Ac	911.204 keV
^{228}Ac	968.971 keV
^{212}Pb	238.633 keV
^{208}Tl	583.187 keV
^{208}Tl	2614.511 keV

the energy in each pulse of the HPGe detectors, the waveforms were subjected to several filters. First the baseline of the recorded waveform was restored to 0 by calculating the linear function

$$f(t) = m \cdot t + c \tag{6.8}$$

with the slope m and an additive constant c describing the baseline of the waveform. To calculate the slope, two mean values of first and second 16 values of the baseline were calculated:

$$y_1 = \frac{\sum_{i=1}^{i=16} f(t_i)}{16} \text{ and } y_2 = \frac{\sum_{i=17}^{i=32} f(t_i)}{16} \tag{6.9}$$

with $f(t_i)$ being the i-th sample in the waveform and arbitrarily $t_i = i$. The slope m is then calculated as

$$m = \frac{y_2 - y_1}{16}. \tag{6.10}$$

The additive constant c is then given by

$$f(t_8) = y_1 = m \cdot 8 + c \Longleftrightarrow c = y_1 - m \cdot 8. \tag{6.11}$$

The waveform with restored baseline y_{bl} is then given as

$$y_{\mathrm{bl}}(t_i) = y(t_i) - m \cdot t_i - c. \tag{6.12}$$

An example of this transformation is shown in figure 6.18. A pole zero correction is then carried out for the pulses of the HPGe detector as they are for the pules of the PET scanner. The time constant is again determined by using a minimizer to optimize a template pulse. The template is again made from 500 pulses in a calibration measurement. The only selection criteria is to be higher than 500 LSB so the pulses are not dominated by noise. The result of a pole zero correction carried out on a HPGe pulse template can be seen in figure 6.19. The timing constants determined this way are used to correct every waveform. Finally this step shaped waveforms are convolved with a trapezoidal filter with rising and falling widths of 40 samples and a flat top of 15 samples. A visualization is shown in figure 6.20. Finally 3 moving average filters with a width of 20 samples each are applied. This is visualized in figure 6.21 The energy in a.u. contained in the waveform is then determined as the height of the result of the moving average filtering. The result of a flood measurement of 10 min with the described source can be seen in figure 6.22. To calibrate the energy, all given literature lines are fitted. To identify the lines, a rough calibration is carried out first. The highest occuring line in the spectrum is the 2614 keV line of ^{208}Tl. The position of the line in the spectrum $E_{\mathrm{Tl,\ uncal}}$ is determined and all energies E are then roughly calibrated by

$$[!htb]E_{\mathrm{rough\ cal}} = E\frac{2614\,\mathrm{keV}}{E_{\mathrm{Tl,\ uncal}}}. \tag{6.13}$$

This way all lines are close to their expected positions in the spectum. The result of this rough calibration with the positions of all used lines indicated can be seen in figure 6.23. A small window of 50 keV around each listed γ line is fitted with a function $gamma\_line(E)$ describing

the line itself and approximates its background:

$$\text{gamma\_line}(E) = g(E,a,m,s) + h \cdot s \cdot g(E,1,m,s) \cdot d(E,m,s,t) \cdot (1 - t^2 \cdot d(E,m,s,t)^2) + c \quad (6.14)$$

with the gaussian distribution

$$g(E,a,m,s) = \frac{a}{\sqrt{2\pi} \cdot s} \exp(-\frac{(m-E)^2}{2 \cdot s^2} \quad (6.15)$$

as well as an exponential lower tail described by the latter part using the function

$$d(E,m,s,t) = \frac{1}{s + t \cdot \frac{x-E}{s}}. \quad (6.16)$$

The parameter m is the mean of the gaussian distribution, a is the amount of events contained in the distribution and s is its sigma. h is the height and t is the decay constant of the exponential tail. c describes the approximately constant background. The description of the exponential tail is directly taken from [5]. The results of the fits are shown in figure 6.24. For the mean values derived from the fits and the respective literature values a linear relation

$$E_{\text{cal}}(E_{\text{rough cal}}, m_{\text{cal}}, c_{\text{cal}}) = m_{\text{cal}} \cdot E_{\text{rough cal}} + c_{\text{cal}} \quad (6.17)$$

between these two sets is fitted to calibrate the energies in a more precise way. The result of this linear fit can be seen in figure 6.25. With the result of this linear fit the calibrated energy values E_{cal} can be calculated for the entire measurement. The final result of the calibration can be seen in figure 6.26. The positions of the γ lines used for calibration are indicated. For a somewhat complete characterization similar to those used for LEGEND-200, the A/E value of the detector has to be calculated in calibrated as well. To calculate the current amplitude of a waveform, the baseline is subtracted as described for the energy calculation. In a next step the waveform is upsampled using linear interpolation from the 16 ns sampling period of the FADC to a period of 1 ns. The waveform is then smoothed by applying 3 moving averages of a length of 30 samples each. Finally the derivative is calculated as the difference between neighbouring samples divided by the new period. The amplitude of the resulting derivative is used as current amplitude. The current amplitude is divided by the respective energy of the event. The result is visualized as a 2d histogram of energy and uncalibrated A/E value in figure 6.27. To calibrate the A/E, the line is sliced into 9 energy intervals with a width of 100 keV each. The interval

1500 − 1600 keV containing the double escape peak of the ^{208}Tl line is excluded, resulting in only 9 intervals considered. For each interval the A/E spectrum is fitted with a function made of a gaussian distribution and an exponential tail:

$$A/E(E) = g(E, a, m, s) + j(E, m, f, l, d, t) \tag{6.18}$$

with the empiric function describing the tail

$$j(E, m, f, l, d, t) = m \cdot \frac{\exp(f \cdot (E - l)) + d}{\exp(t \cdot (E - l)) + l} \tag{6.19}$$

taken again from [5]. The results of these fits can be seen in figure 6.28. With the means of the A/E distributions determined a linear relation

$$\text{linear}_{\text{A/E uncal}}(E) = m_{\text{A/E uncal}} \cdot E + c_{\text{A/E uncal}} \tag{6.20}$$

can be fitted. The result of this fit can be seen in figure 6.28. To calibrate the A/E values with this linear relation, they are divided by the function:

$$A/E_{\text{cal}} = \frac{A/E_{\text{uncal}}}{\text{linear}_{\text{A/E uncal}}(E)}. \tag{6.21}$$

With this correction a completely calibrated 2D histogram of energies and A/E values can be produced. The result is shown in figure 6.29. The line representing the Compton continuum is now centered around 1, as desired. In total, regarding energy and A/E calibration, it can be concluded that the HPGe detector works as expected.

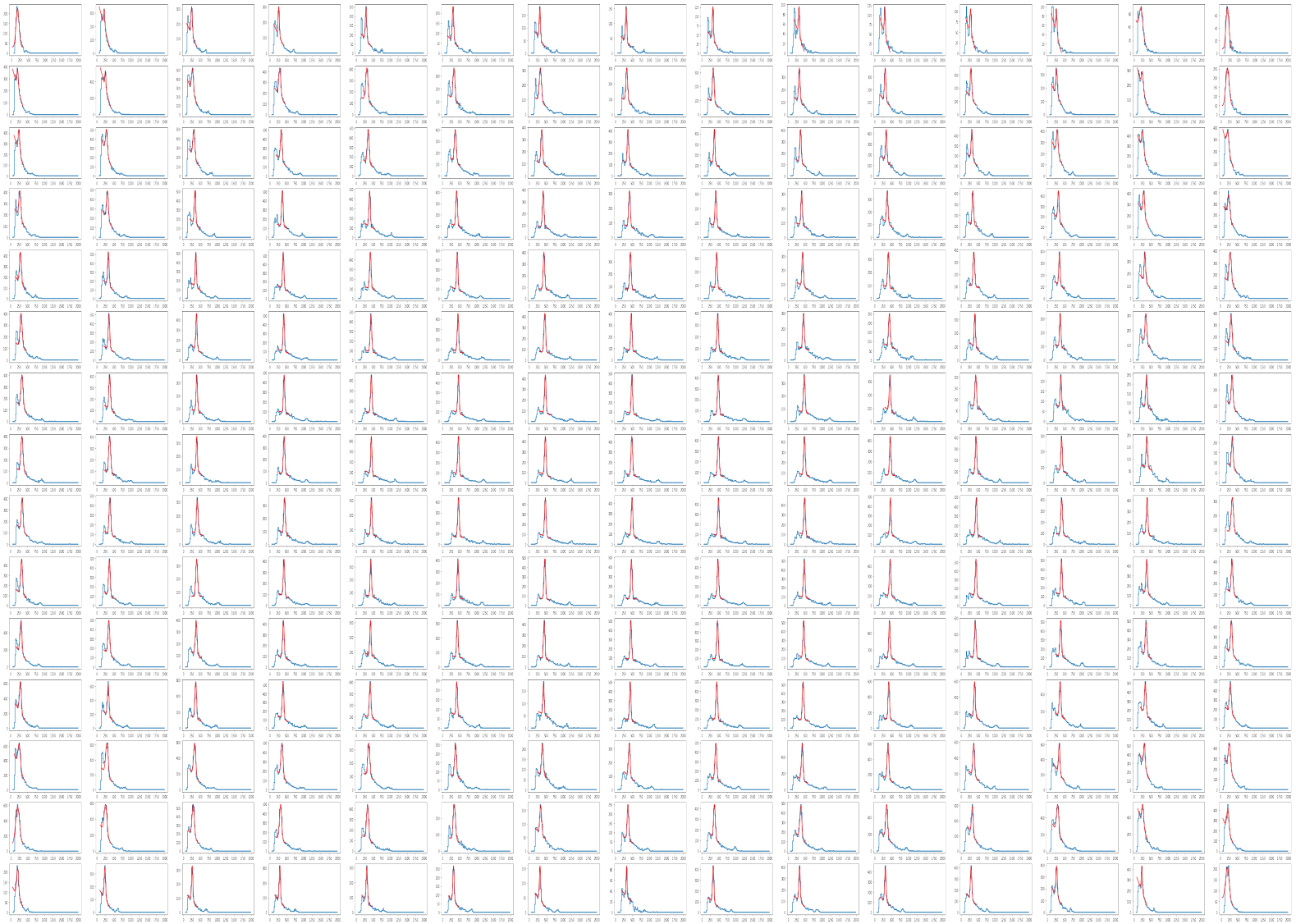

Figure 6.15: Fits of the energy spectrum for every pixel of detector block 14. The pixels in a cross shaped region sparing the corners have good spectral shape and energy resolution. The corners work not as well.

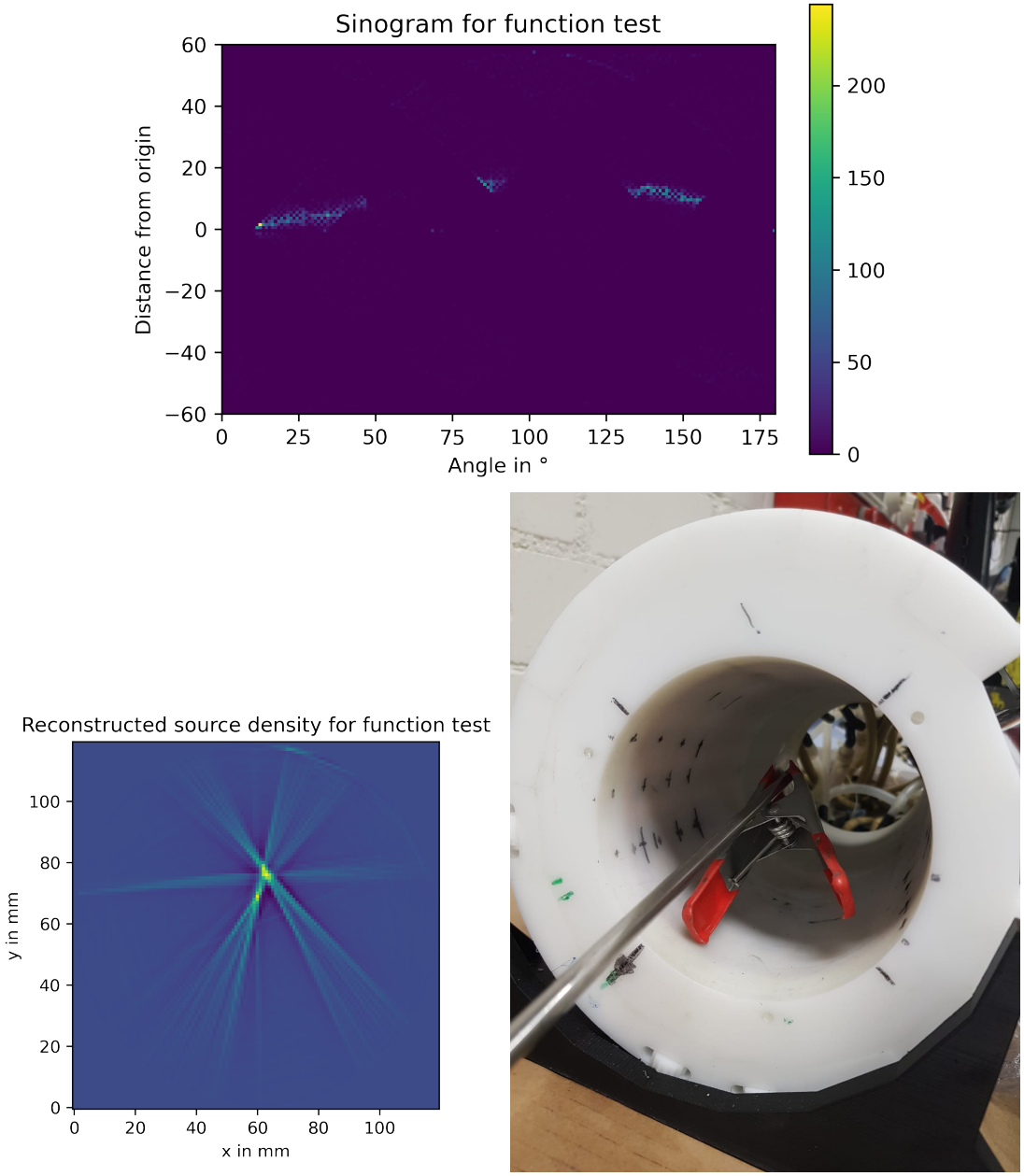

Figure 6.16: Top: Sinogram produced from a measurement with a ^{22}Na source placed in the PET scanner. Bottom left: Reconstructed source distribution inside of the PET scanner. Bottom right: Picture of the source placement inside of the PET scanner.

Figure 6.17: Picture of the used HPGe detector. It is mounted in an ORTEC PopTop cryostat and attached to a 30 l Dewar.

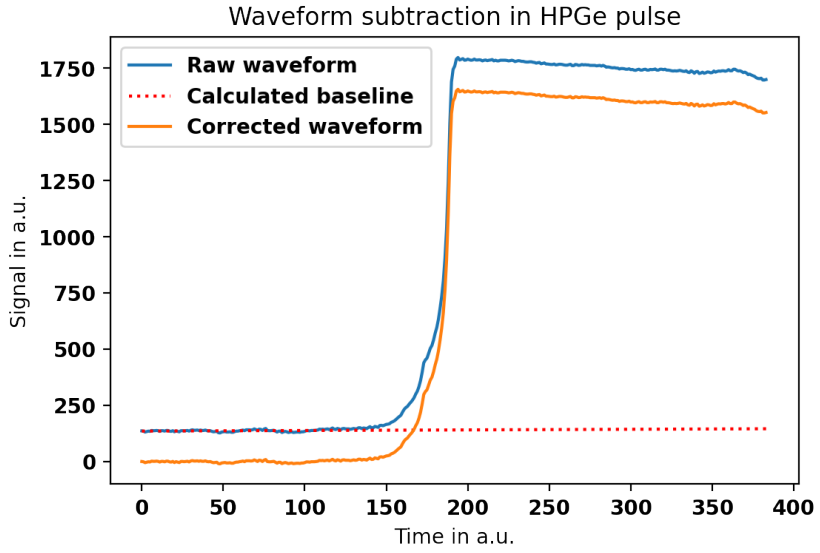

Figure 6.18: Visualization of the baseline restoration for a waveform. In blue: Waveform as recorded by the FADC with a baseline located around 120. The calculated linear function is drawn in red. In orange: Same waveform with the calculated linear function subtracted.

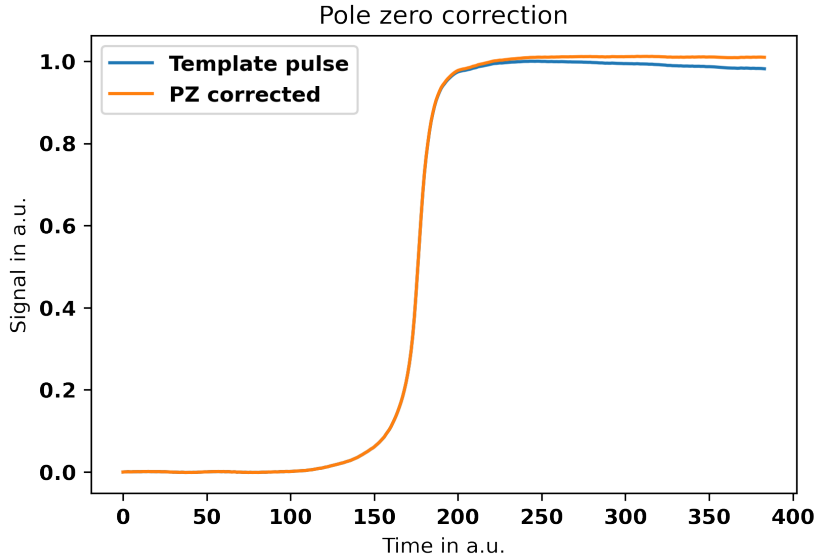

Figure 6.19: Pole zero correction of the template waveform. In blue: Template waveform produced from 500 waveforms not dominated by noise. In orange: Template waveform with pole zero correction according to minimizer results applied.

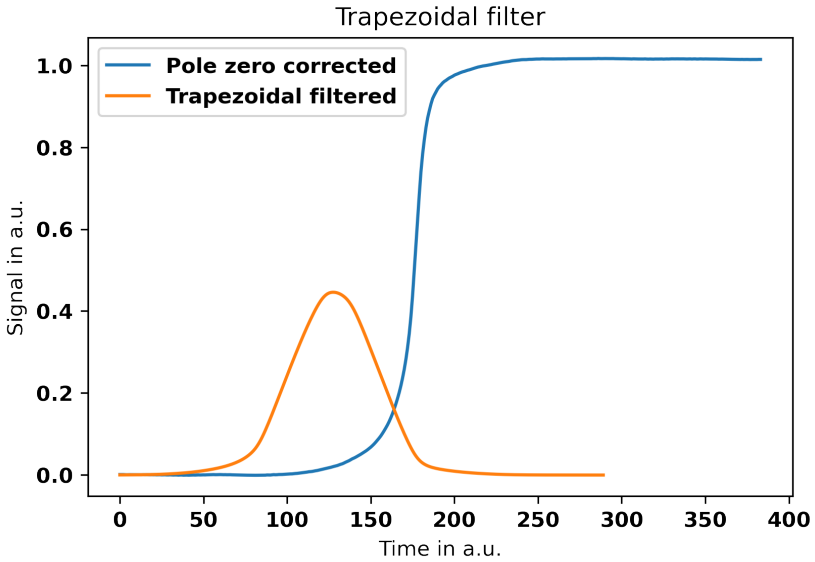

Figure 6.20: Visualization of a trapezoidal filter with rising and falling edge of 40 samples and a flat top of 15 samples applied to a pole zero corrected waveform. In blue one can see the pole zero corrected waveform and in red the same waveform with a trapezoidal filter applied.

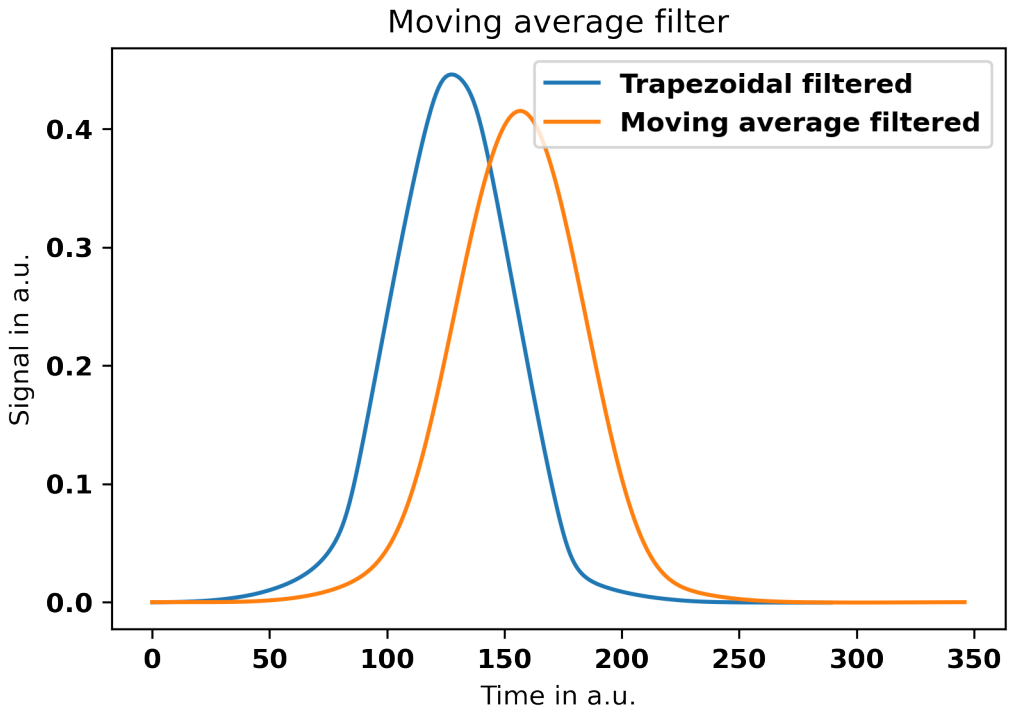

Figure 6.21: Visualization of 3 moving average filters with a width of 20 samples applied to a trapezoidal filtered waveform. In blue one can see the trapezoidal filtered waveform and in orange the moving average filtered waveform.

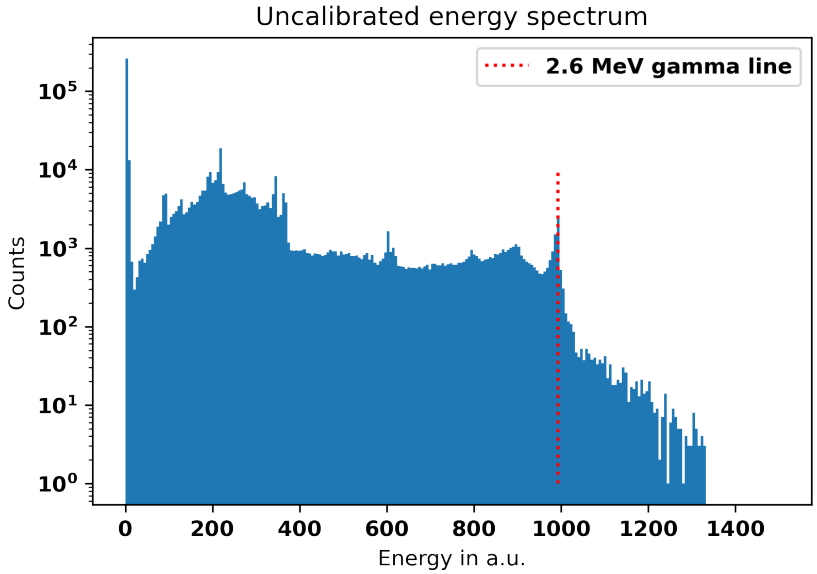

Figure 6.22: Uncalibrated result of a calibration measurement, carried out as 10 min of flood measurement with the described ^{232}Th source.

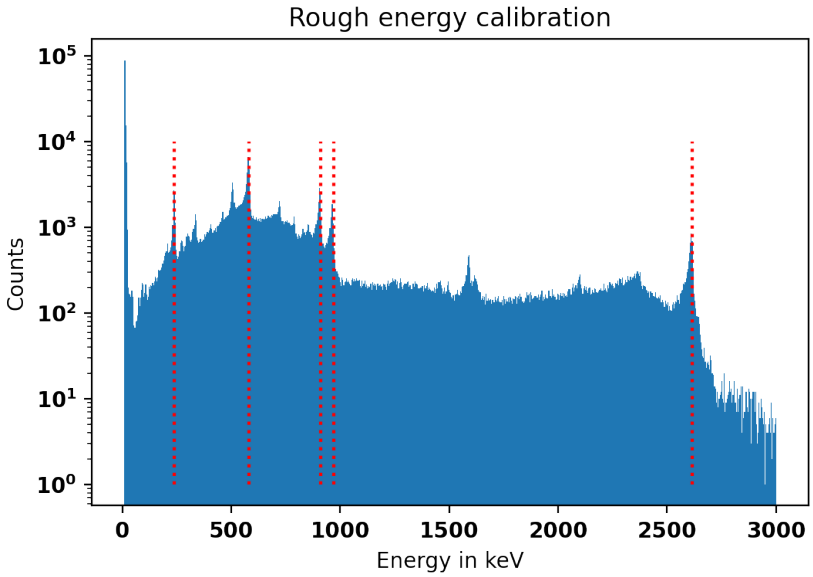

Figure 6.23: Roughly calibrated energy spectrum with the positions of the used lines indicated.

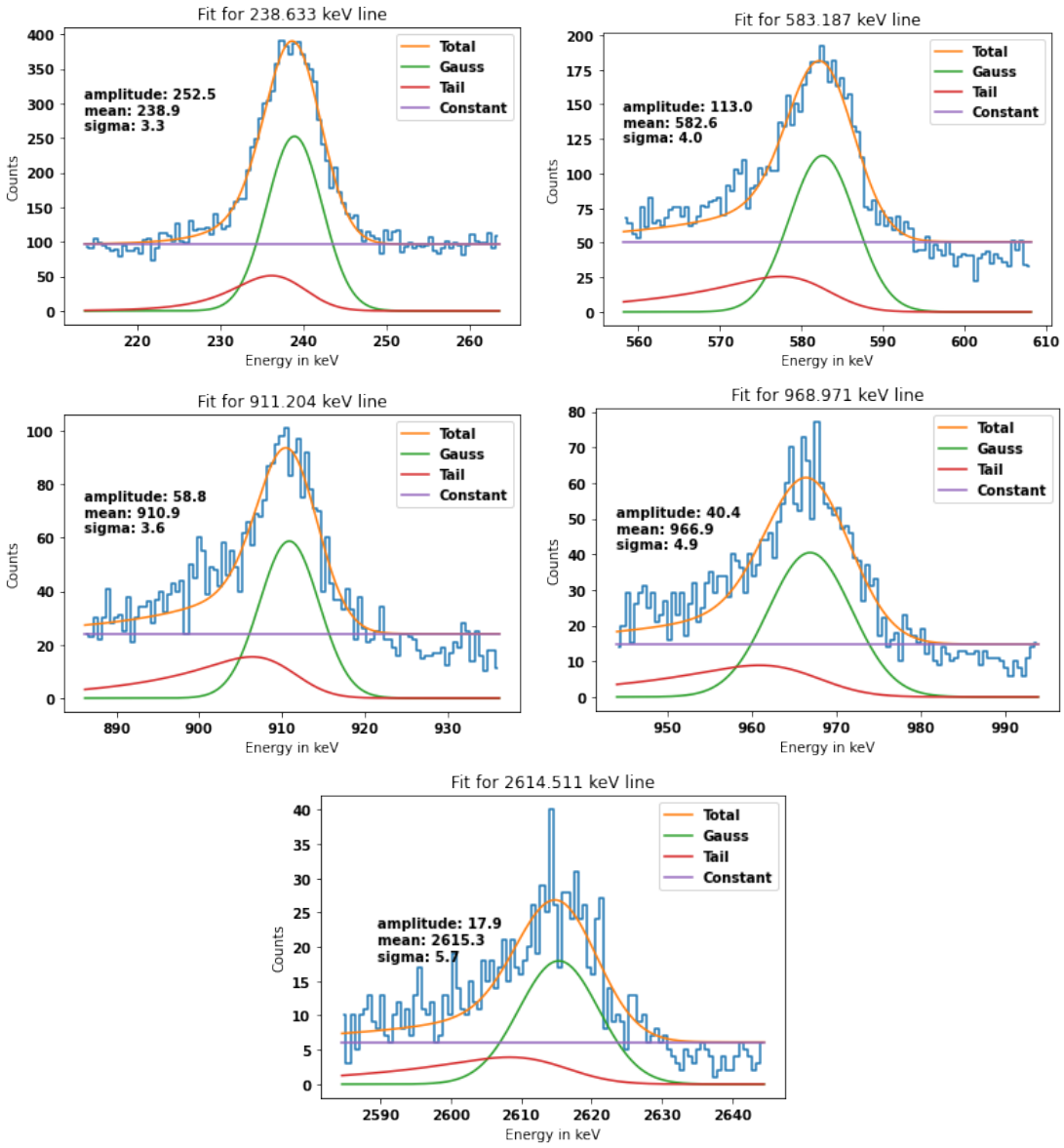

Figure 6.24: Results of the fits of the γ lines. Top left: Fit for the 911.204 keV line. Top right: Fit for the 968.971 keV line. Middle left: Fit for the 238.633 keV line. Middle right: Fit for the 583.187 keV line. Bottom: Fit for the 2614.511 keV line.

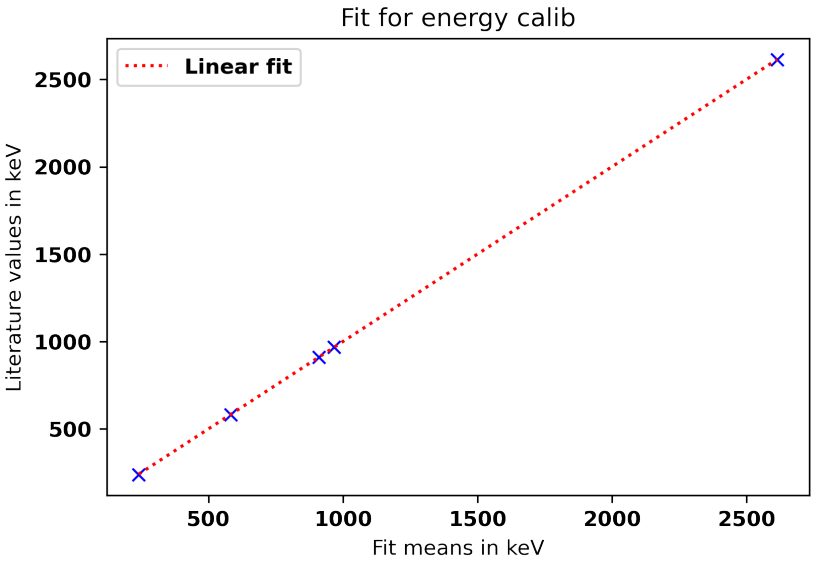

Figure 6.25: Linear fit between the means derived from fitting the γ lines and their literature values.

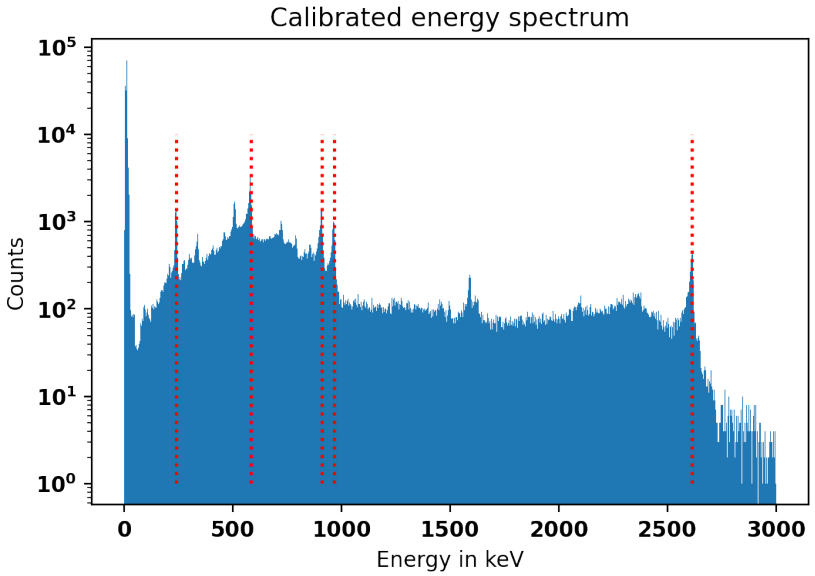

Figure 6.26: Final result of the calibration measurement. The positions of the γ lines used for calibration are indicated.

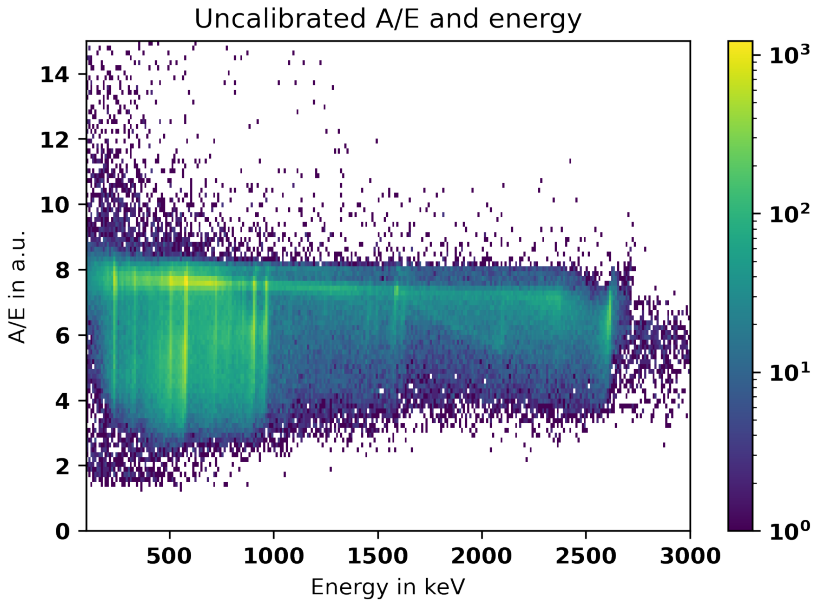

Figure 6.27: 2D histogram showing the calibrated energies and the uncalibrated A/E values. The clear horizontal line contains SSEs from the Compton continuum and several γ lines. The events trailing towards lower A/E values indicate MSEs, e.g. multi Compton scatter events of the γ lines.

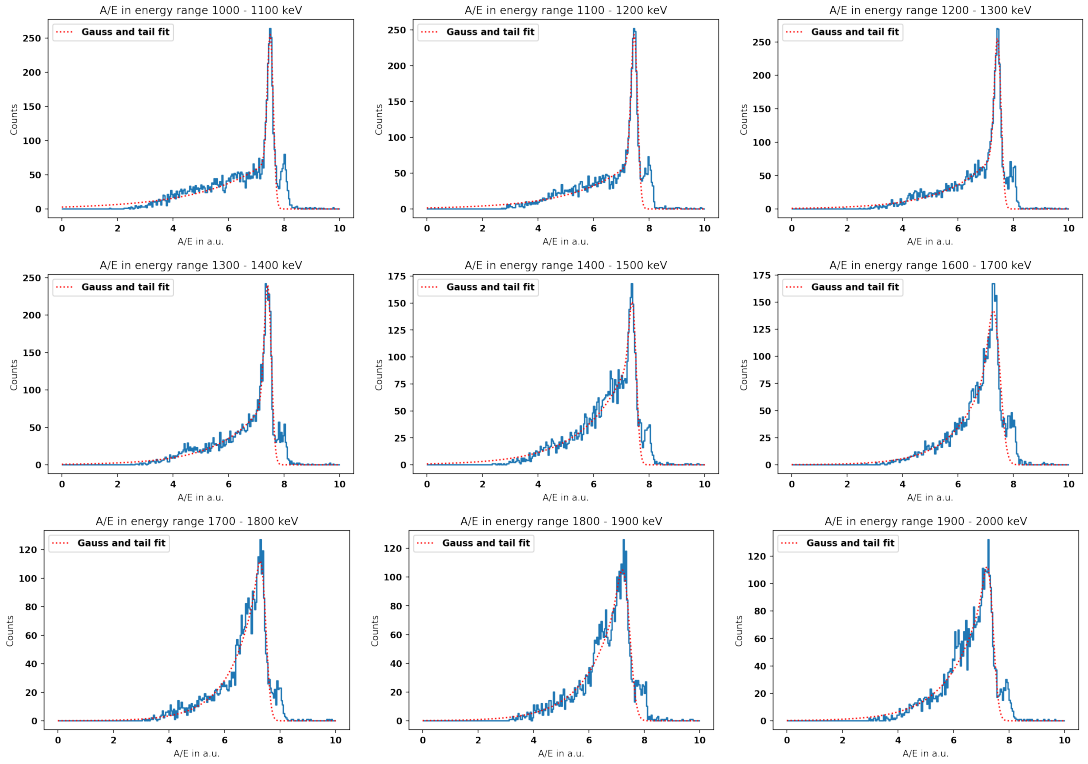

Figure 6.28: Results of the fits of the A/E distribution in intervals along the Compton continuum. Top left: Fit result for the interval 1000 − 1100 keV. Top right: Fit result for the interval 1100 − 1200 keV. Second from top left: Fit result for the interval 1200 − 1300 keV. Second from top right: Fit result for the interval 1300 − 1400 keV. Third from top left: Fit result for the interval 1400 − 1500 keV. Third from top Right: Fit result for the interval 1600 − 1700 keV. Fourth from top left: Fit result for the interval 1700 − 1800 keV. Fourth from top right: Fit result for the interval 1800 − 1900 keV. Bottom: Fit result for the interval 1900 − 2000 keV.

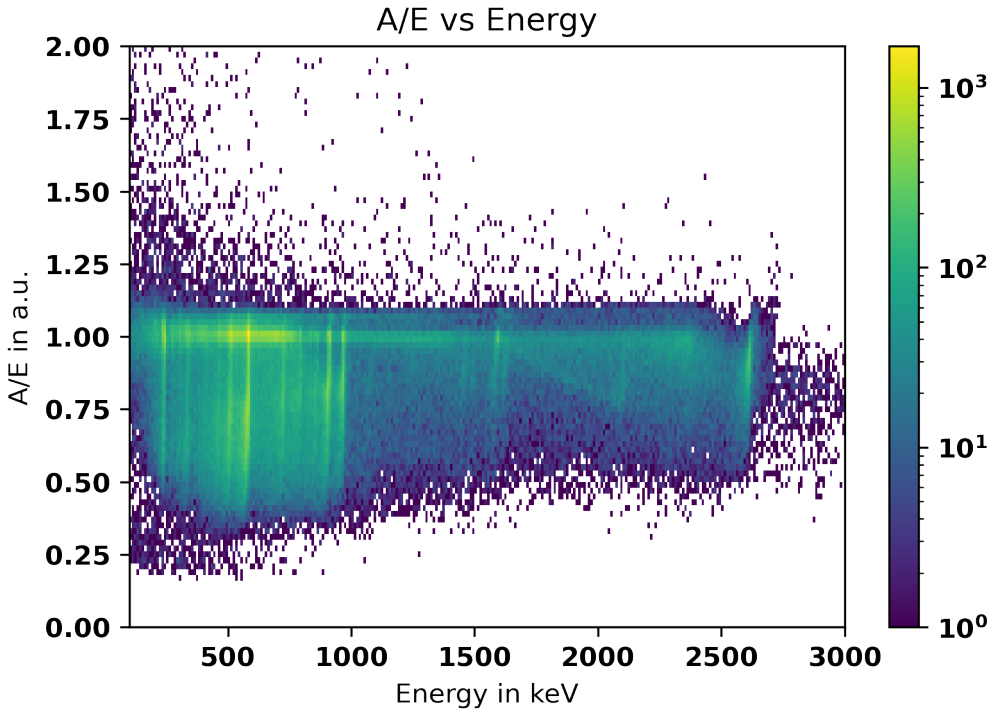

Figure 6.29: A/E corrected for its energy dependence and energies. The line in the 2D histogram is centered around 1 as desired. The distribution shows no abnormalities.

7

Proof of concept for the test stand

"A man's worth is no greater than his ambitions."

- Marcus Aurelius, *Roman leader*

The approach chosen to make a clear proof of concept for the test stand was to do an actual measurement. The following sections will describe the trigger logic, the physical setup, event selection for a measurement and finally the result for this measurement regarding the proof of concept.

7.1 Trigger logic

The 16 detector blocks with for 4 outputs each of the PET scanner were initially connected to the 64 channels of a CAEN V1740D flash analog to digital converter (FADC). It has a sampling frequency of 65 MHz (or sampling period of 16 ns) and a resolution of 12 bit for its input range

of 2 Vpp. The post trigger is set to 67 % of a waveform made of 384 samples.
Over the course of calibration measurements it was realised that the detector block numbered 8 did not produce any signal. The ICs still obtainable commercially on the preamplifier electronics PCB were exchanged, but to no effect. Due to this result the detector block was deemed defective beyond repair and the input channels 32, 33, 34 and 35 not used. The corresponding inputs were instead used for the HPGe detector. It was plugged into the first channel reserved for detector block 8, namely channel 32.
For acquisition of events for the proof of concept, the FADC was used with a majority level. Due to the architecture of the FADC its channels are grouped into 8 channels processed by the same FPGA (field programmable gate array) respectively. The majority level takes into account the number of these subgroups producing a trigger, regardless of how many channels in a subgroup triggered. The trigger contribution of individual channels in a subgroup can be disabled. All channels are enabled for triggering except for those of block 8. All the channels are read out, independent of their trigger setting. The majority threshold level is set to $n = 1$ within $k = 3$ samples, which means the FADC is read out if at least $n + 1 = 2$ of the enabled subgroups produce a trigger signal within $k = 3$ consecutive samples (48 ns).
An event that is saved therefore occurs when at least 2 of the detector blocks trigger within 48 ns. For such events produced by a double escape event in the HPGe detector, an event in the HPGe detector has to occur in delayed coincidence (the pulse formation in the HPGe is slower). The length of the recorded waveforms was chosen long enough to include the beginning of a HPGe pulse in delayed coincidence. This was checked by illuminating the HPGe detector inside of the PET scanner with a ^{232}Th source. The double escape events produced in the HPGe detector can be triggered on using the PET. To prove that indeed coincidences do happen, for the HPGe waveforms recorded the beginning of the pulse relative to the PET trigger is determined by the crossing of a simple threshold well above the noise. The distribution of the starts of events randomly occuring in the waveform should be flat, as the probability for every point in time is the same. If there are events happening in coincidence with the PET scanner, their start time should be more or less the same in every such event and a line at some point in the HPGe pulse arrival time should form. The result of such a measurement with a duration of 12 h is shown in figure 7.1. One can clearly see the flat distribution of background events with some structure on top of it. This structure diverts from the pure line distribution due to several effects. The most prominent effect likely are events occuring close to the readout point contact, coming from γs entering the detector through the bore-hole. Since a large part of the signal formation happens

close to the point contact, such events have a very sharp rise time. This causes the rising flank of the signal to cross the threshold relatively earlier than for events coming from the bulk of the detector. Events starting in the bulk begin with a relatively small current when the charges are still far away from the point contact. A contribution for the later side of the line are MSE-like events, i.e. events with to or more steps in its waveform due to multiple charge clouds in the detector. The first step can be below the threshold used to define the start of the pulse, but a subsequent step can exceed the threshold which shifts the arrival time to the back. Factoring in these effects the distribution is as expected and coincidence measurements between the PET scanner and the HPGe detector can indeed be performed.

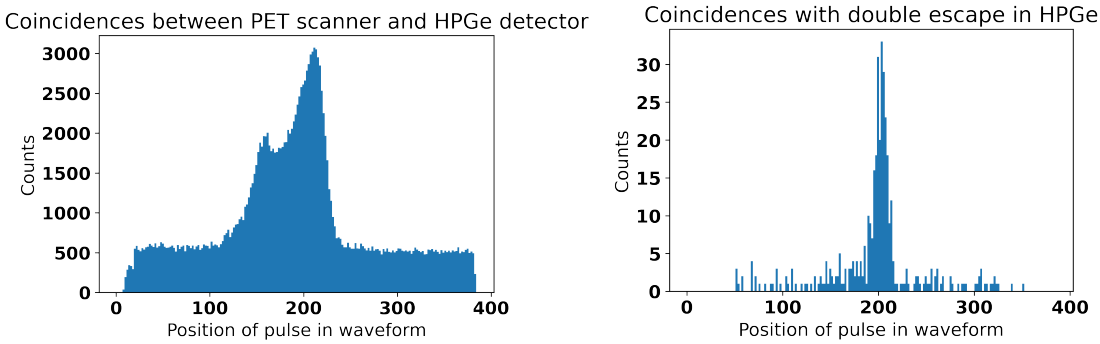

Figure 7.1: Spectrum of the arrival times of HPGe pulses arriving when the PET triggers in multiple detector blocks. Top: Spectrum of arrival times from all events. As expected there is a flat distribution of arrival times from random coincidences. Additionally there is a line with a soft step in the distribution stemming from real coincidences arriving at a somewhat constant point in time relative to the event in the PET. The additional step in the line stems from MSE waveforms, i.e. waveforms with a step. For a lower first part of the waveform, the first part can lie below the threshold and only second step moves above it. This shifts the location of the line to the back as the second step naturally occurs later in time than the first. Bottom: Arrival time of HPGe pulses with an energy of $(1592.5 \pm 10)\,\mathrm{keV}$, the energy of a desired double escape event. A clear line with almost no background is visible.

7.2 Physical setup

One of the most important aspects to guarantee reproducible spatial scans of a HPGe detector is its reproducible placement inside the PET scanner. For this purpose a centering ring for the HPGe detector placing it in the center of the PET scanner was designed and produced using a 3D printer. The centering ring has a length of 15 cm and is made from PLA since that was the most commonly available material for the used 3D printer. The ring is mounted on the

aluminium endcap of the HPGe detector, both aligned to end simultaneously. The centering ring has markings on the outside, in order to measure how far the detector has been inserted into the PET scanner. A picture of the centering ring on its own as well as the ring mounted on the HPGe detector can be seen in figure 7.2. Additionally a collimator for the ^{232}Th source was produced. It is a simple prototype allowing only one setup, but for the proof of concept the design is sufficient. It is a disk perfectly fitting into the PET scanner made of 15 mm of lead. It has one off-axis hole with a diameter of 5 mm. The hole cannot be in the middle of the disk as this position coincides with the roughly 40 mm deep borehole in the HPGe detector. This would mean the HPGe detector would have to be inserted much further for the volume of interaction to be inside the PET scanner, which is feasible but requires a reconstruction of the current mounting of the PET scanner. A picture of the collimator on its own as well as inserted into the PET scanner can be seen in figure 7.3. For the performed measurement the collimator is inserted into the PET scanner in a way that its edge is 90 mm from the front of the PET scanner. The hole in the collimator is located on the vertical line through the symmetry axis of the PET scanner. The HPGe detector is then inserted from the front until it touches the collimator. From the back of the PET scanner the Th source is put in front of the hole in the detector. A picture as well as a sketch of this setup can be seen in figure 7.4. This setup allows for significantly higher γ flux in the HPGe detector on the axis of the hole in the collimator. In the analysis only events with coincident energy depositions of 1592 keV in the HPGe detector and 511 keV in two different detector blocks of the PET scanner are considered. If the setup works as intended events meeting these requirements should form a clear distribution around the hole in the collimator in the reconstructed PET image.

7.3 Event selection

The measurement considered here was carried out with the described experimental setup and the trigger conditions tested in the previous section. The duration of the measurement was 14, h. Since all events are triggered by the PET scanner (signalling at least some energy distribution) the HPGe detector was considered to be a much stricter cut since energy depositions in it are not neccessary to trigger. For each event recorded, the energy in the HPGe waveform and the start of the pulse in the waveform were determined as described in the HPGe calibration and the trigger logic respectively. A 2D histogram is formed from the pulse arrival time and the energy in the HPGe waveforms. For desired double escape events in the HPGe detector in coincidence with

Figure 7.2: Left: Centering ring for the HPGe detector. It perfectly fits the outside of the HPGe detector and the inside of the PET scanner. It is made from PLA in a 3D printer and has markings on the outside indicating how far the HPGe detector was inserted into the PET scanner. Right: Centering ring mounted onto HPGe detector.

the PET scanner a small island limited in arrival time and energy around 1592 keV is expected. The result is shown in figure 7.5. As expected an island has formed in the desired region. All events with times around 25 samples of its time mean and energies around 10 keV around its energy mean were considered going forward.

For the events selected meeting the criteria in the HPGe detector it was checked whether they met the criteria for the PET scanner. For every event the energy in every detector block was determined as described in the calibration of the PET scanner. An effective multiplicity was calculated as the sum of detector blocks in a event meeting the energy boundaries determined

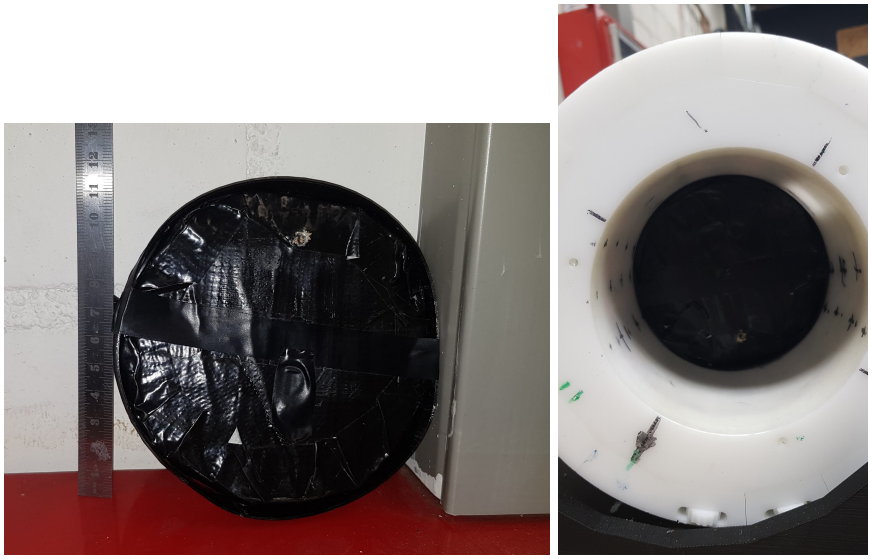

Figure 7.3: Left: Circular collimator used for the measurement. It is made of lead with a thickness of 15 mm and has a hole with a diameter of 5 mm about 30 mm from the outer edge. Right: Collimator placed in the PET scanner.

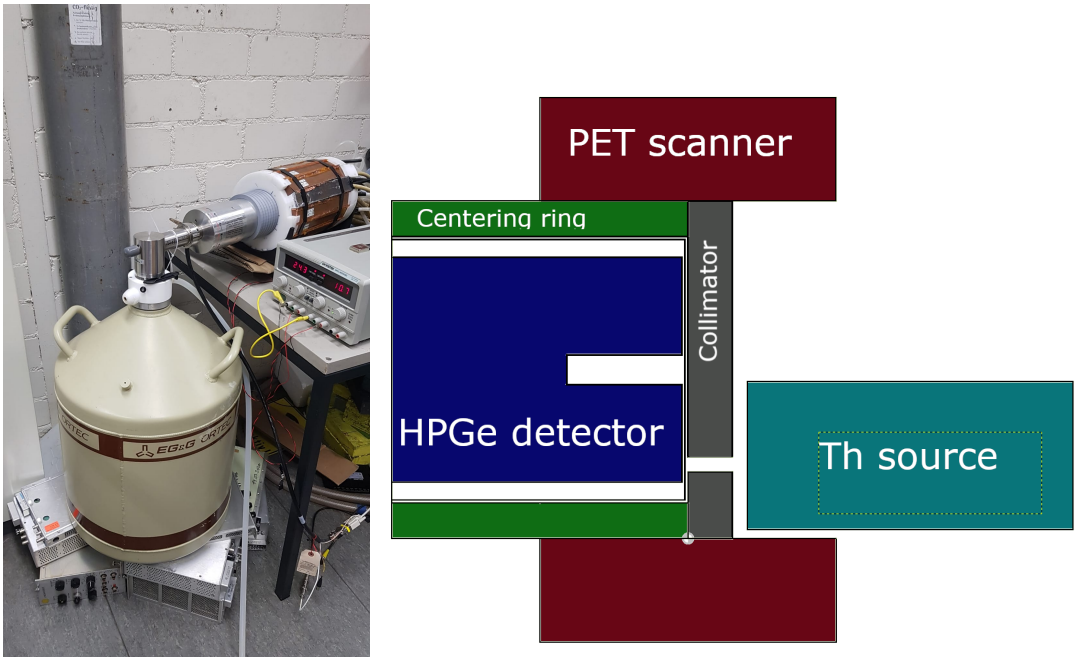

Figure 7.4: Measurement setup for the proof of concept. Left: Picture of the assembly. Right: Sketch of the relative positions of the components.

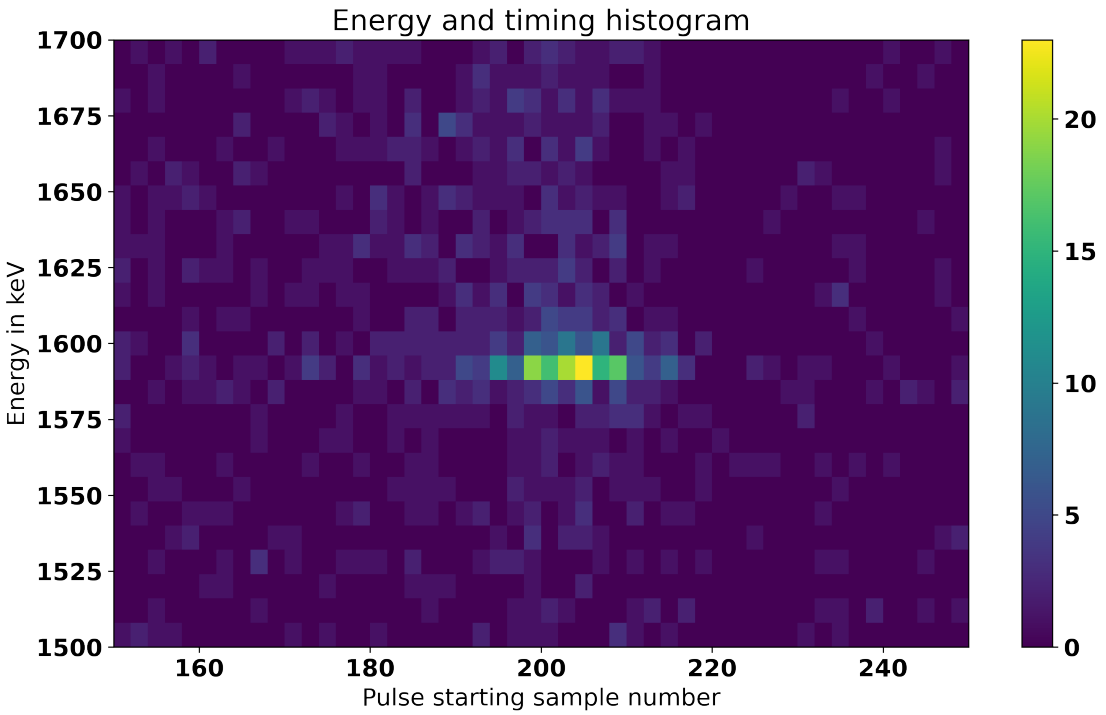

Figure 7.5: 2D histogram of pulse arrival time and pulse energy for HPGe waveforms recorded after PET scanner triggers. An island limited in time and energy at around 1592 keV can be seen. Desirable events are located in this island.

in the PET scanner calibration. If this effective multiplicity was equal to 2, the arbitrary x and y coordinates for these blocks were calculated and designated to pixel indices as described in the calibration of the PET scanner. The result was considered the final dataset of the measurement and fed into the image reconstruction script used in the PET scanners calibration. The distribution of hit detector blocks in this dataset is shown in figure 7.6.

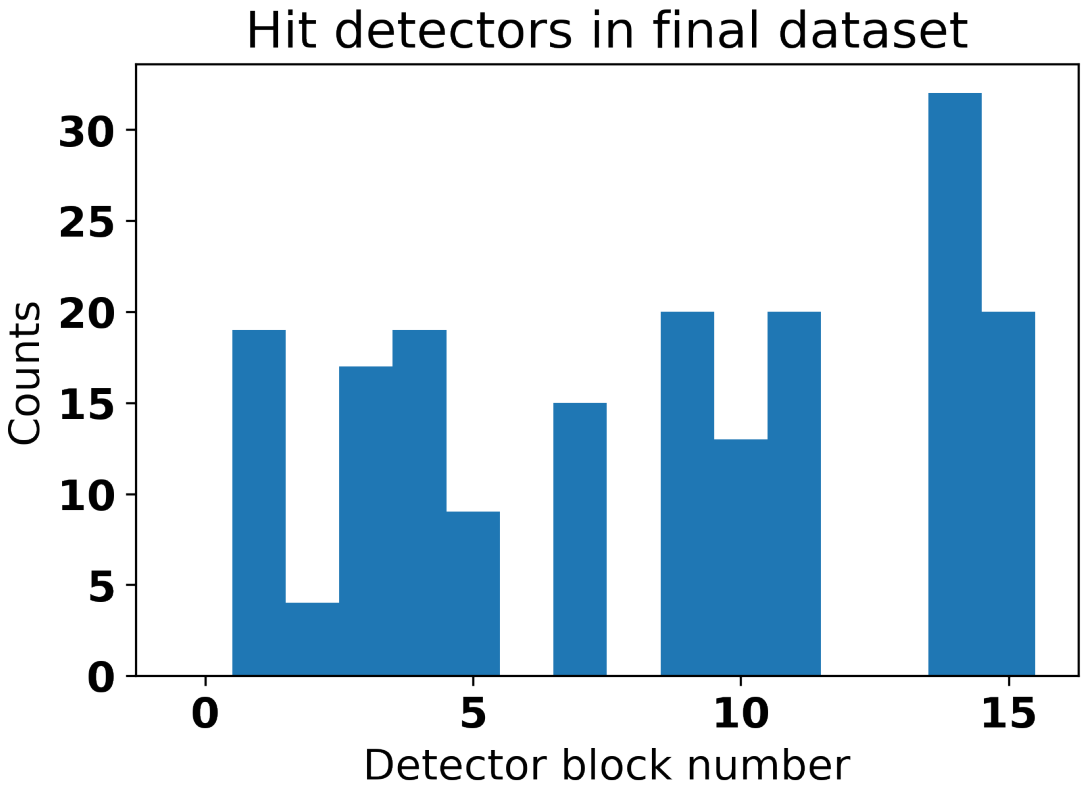

Figure 7.6: Hit detector blocks in the final dataset. The gaps are due to broken or effectively unusable detector blocks.

7.4 Result of the measurement

Using the image reconstruction script used for the calibration of the PET scanner, a sinogram can be produced from the final dataset. The sinogram is shown in figure 7.7. In the sinogram a smeared sinusoidal line can be observed, as would be expected for a small extended source (almost point-like). Using the inverse Radon transform the source density distribution for this

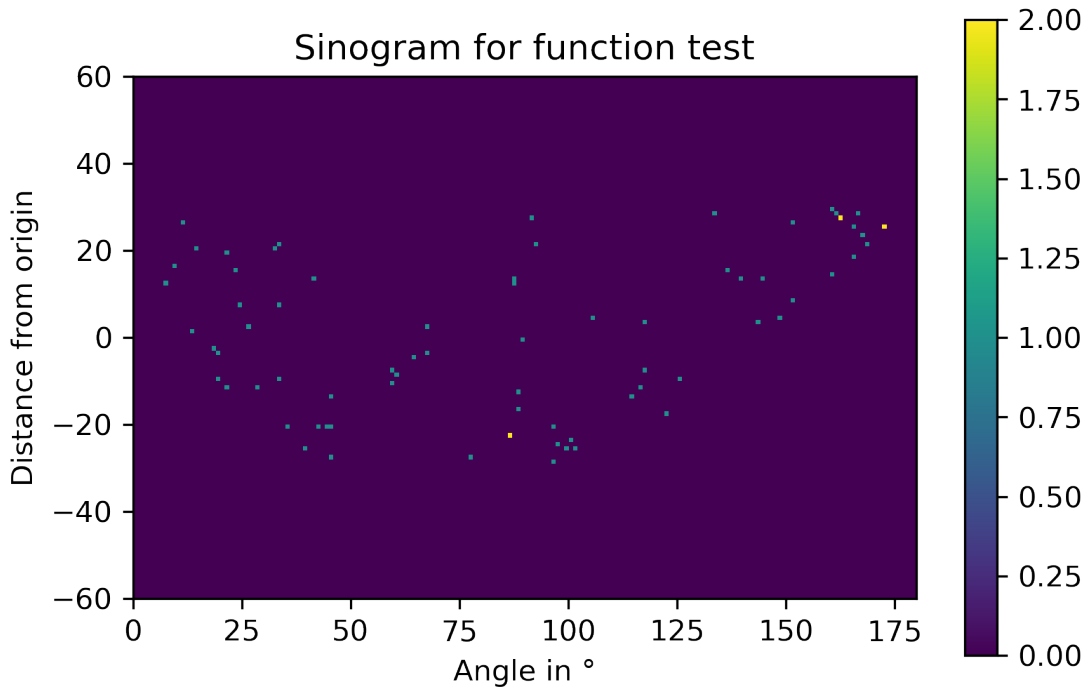

Figure 7.7: Sinogram produced from the final dataset. A smeared sinusoidal line in the sinogram can be observed, as would be the case for a small extended source.

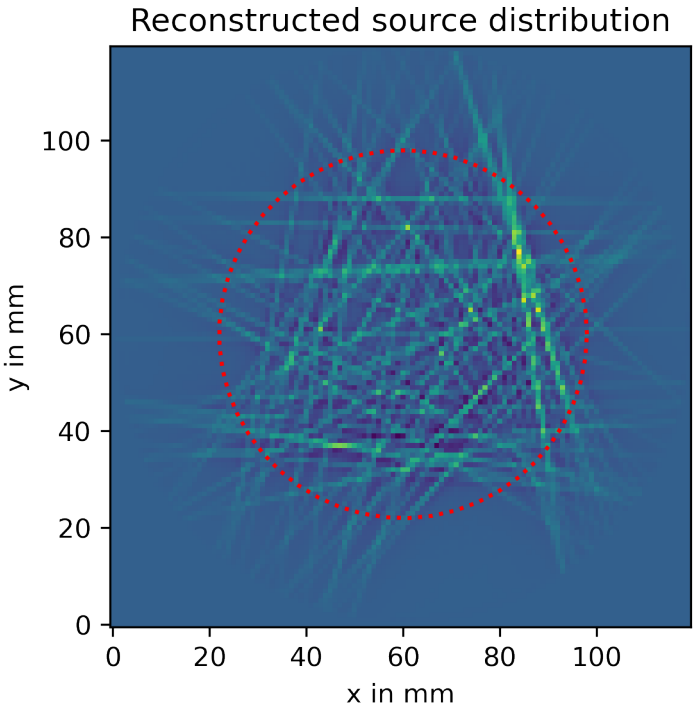

Figure 7.8: Reconstructed source density of the measurement. A diffuse background with a clear accumulation in the top right can be observed.

sinogram can be calculated. The result for the produced sinogram can be seen in figure 7.8. It does show some random backgrounds, but also a clearly defined extended source. This is exactly the signature that was expected for the setup if it was working as extended. The diffuse background probably stems from the used Th source producing random coincidences in random detector blocks. It has a relatively bright gamma line at 583 keV which can mimic the 511 keV line that the PET scanner is sensitive to. This is especially true if the gamma hits a block not perpendicular to the surface, like the gammas coming from the source placed outside of the detector ring. This background could be mitigated somewhat easily with a source producing only a desired high energy line. The production and test of such a source is however beyond the scope of this work. It can be concluded that the measurement method for producing SSEs in HPGe detectors with known locations works as intended.

8

The muon cherenkov veto for LEGEND-200

"I'm so fast that last night I turned off the light switch in my hotel room and was in bed before the room was dark."

- Muhammad Ali, *Boxer*

The LEGEND-200 experiment re-uses some of the GERDA setup, including the muon Cherenkov veto, which was initially designed and constructed by the University of Tübingen [30, 22]. Every description of GERDA hardware in this chapter comes from the work carried out for the setup of GERDA.
The muon veto was refurbished and new hardware compatible with the new LEGEND-200 electronics was installed. The placement of some of the PMTs inside of the water tank was changed. Sequentially multiple measurements were carried out to ensure that the new configuration of the muon veto works as expected. The scope and details of this work will be covered in the following sections.

8.1 Removal of the spectroscopy oil from the PMT encapsulations

After the end of measurements for GERDA the water tank containing the muon veto was drained for inspection. During this drainage two of the PMTs imploded and the capsules broke. This situation raised concerns about the integrity of the PMT capsules on one hand and the containment of the spectroscopy oil in the PMT capsules on the other hand. Regarding the capsule integrity the thin PET covers were replaced by thicker acrylic caps. In order to do that the glue sealing of the PET caps had to be removed. Since the spectroscopy oil is located above the place of that sealings the oil was necessarily drained in the process.

The spectroscopy oil was introduced into the capsules in the first place to smooth out the transition of the refractive index from water to PET cap to PMT. Without the oil the space between the PET window closing the capsule and the PMT would be filled by air with refractive index $n_{\text{air}} \approx 1$, being in stark contrast to the refractive index of PET $n_{\text{PET}} \approx 1.61$ and water $n_{\text{water}} \approx 1.34$ [35]. The refractive index of the spectroscopy oil is $n_{\text{oil}} \approx 1.47$ [6] and therefore closer in refractive index than water. Without the oil the amount of light reaching the PMT was estimated to be a factor of ~ 3 lower, the rest would be reflected at the boundaries. The oil therefore increased the data quality significantly. The decision to not refill the oil after draining it from the capsules was still made because of concerns about the enviorenmental impact should it leak into the water and also because the filling ports for the oil were sealed when encapsulating the PMTs for GERDA. A cross section of the original GERDA PMT encapsulations can be seen in figure 8.1. The process of the oil drainage and placement of the new caps is shown sequentially in figure 8.2.

The first step was to drain the PMTs by loosening the screws of the flange holding down the PET window. For these screws threads are cut directly into the steel capsule. After loosening the screws the silicon sealing glue the PET window the capsule was broken by slightly lifting the PET window. A bucket was placed closely under the PMT to catch the oil. The bucket was then emptied into waste disposal containers outside of the water tank. The screws were only loosened and not fully removed in this step to keep the PET window on the PMT as long as possible in order to keep it as clean as possible. As a next step the screws were then fully removed and the ring flange taken off. Then the PMT window was also removed, leaving only the blank PMT. To minimize contaminations of the PMTs and the water tank in general everyone involved wore a single-use cleanroom suit and overshoes as well as a FFP2 mask and a polycarbonate face shield.

The blank PMT was then covered with its new acrylic cap with a rubber sealing between steel capsule and acrylic cap. To improve the tightness even further the connection between capsule and cap was lined with a broad butyl tape that also covers the screw holes on top and bottom of the flange. This butyl tape is further secured by putting quarter ring flanges first on the top and screwing them down. The screws thereby pierce the butyl tape, inserting butyl into the thread to provide further sealing there as well. The screws are rated for a torque of 11 Nm but are secured with a torque of 10 Nm in order to be safe to not break them. Since all the metal appliances are made from stainless steel, removing broken off screws required carefull drilling and bits made from cobalt steel. Despite all efforts some of the screws broke inside of the threads. In these cases the holes where entirely drilled through, removing the screw and the thread. If still movable (once the butyl entered the thread the screws were very secure) the quarter rings were placed so that the middle one of the three holes along its length would be on the drilled out hole of the capsule. If one of the edge holes was aligned with the drilled out one, the tightening of the screw required two people to hold the parts in place since there was no thread anymore to screw the parts in place. After securing the quarter rings from the top, quarter rings were put onto the screws also from the bottom of the flange. These were screwed on with nuts, also with a torque of 10 Nm. The quarter ring was initially chosen for the bottom part of the PMT-acrylic connection because a full ring can not be attached from the bottom due to the high voltage cable being fixed between PMT and outside of the water tank. Since the quarter ring outline could also be packed quite tightly on the metal sheet when manufacturing them, it was decided to use the quarter rings also on the top of the connection to save materials and cost. Finally the foil attached to the acrylic to protect it from scratches was removed.

8.2 Remote control for PMT calibration

With the transition from GERDA to LEGEND much of the existing electronics was switched for newer and more reliable versions. This includes the electronics for the calibration of the muon veto PMTs. For the calibration in GERDA 5 ultra violet LEDs were coupled to optical fibers and fed into the water tank. In the water tank 5 diffusor balls are distributed throughout the water tank to spread the incoming light into the entire available solid angle. A sketch of one of the diffusor balls can be seen in figure 8.3. These diffusor balls were driven by a Digital-to-Analog Converter (DAC) and a pulser generating square pulses (logic signals). These outputs control the 5 LEDs for the diffusor balls via the Printed Circuit Boards (PCB) the LEDs are connected

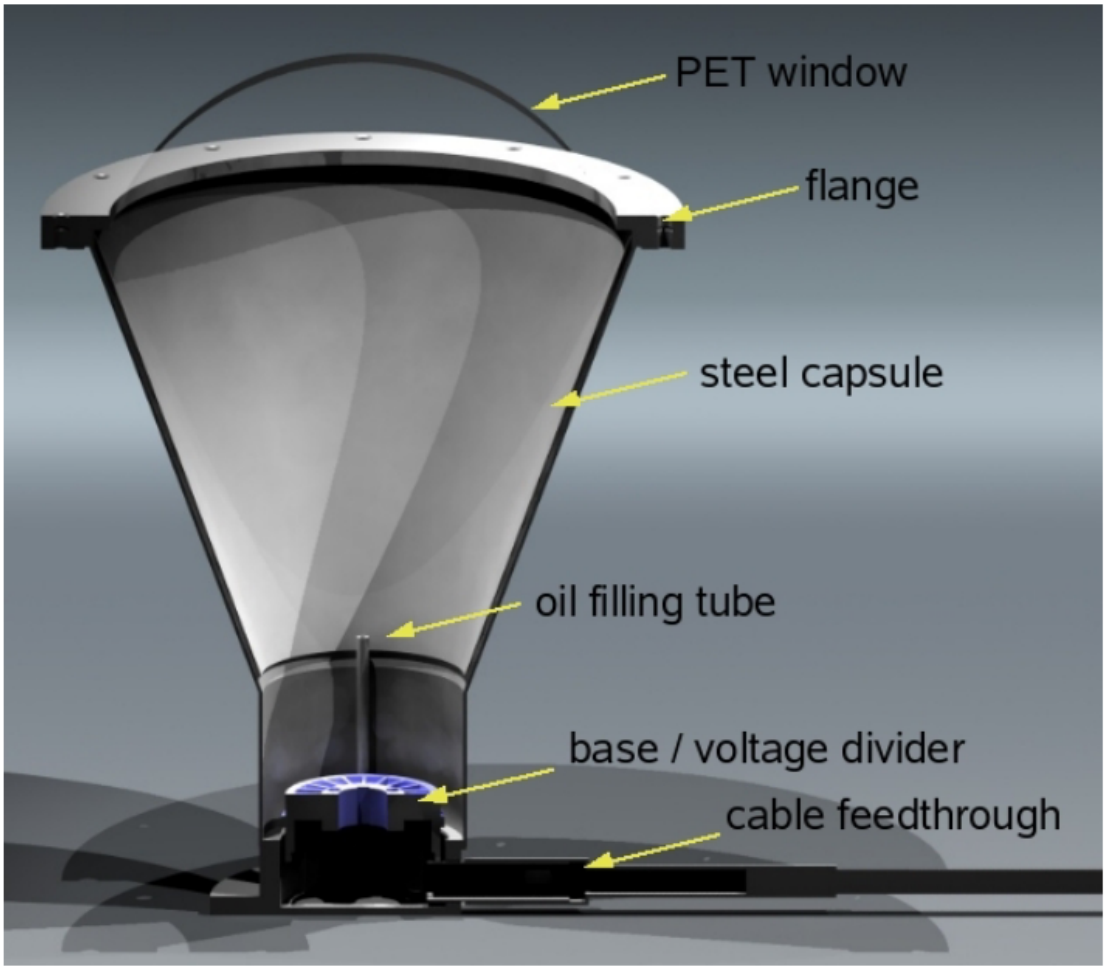

Figure 8.1: Cross section of the original GERDA PMT encapsulations. Taken from [22].

to. A wiring diagram and a picture of one of these PCBs can be seen in figure 8.4. While no logic signal is currently applied the "main capacitor" C_2 is charged by the power supply from the DAC and separated from the LED, respectively connected via transistors T_1 and T_2. When the logic signal is applied, both transistors switch, disconnecting C_2 from the power supply and connecting it to the UV LED and the inductivity L_1. The charge on the capacitor flows through the LED, lighting it up only as long as sufficient current flows. The amount of light depends on the charge on the capacitor which is proportional to the voltage applied by the DAC. The duration of this current flow can be changed by the inductivity wired in parallel to the LED, either improving the current flow or hindering it and therefore changing its duration. In the

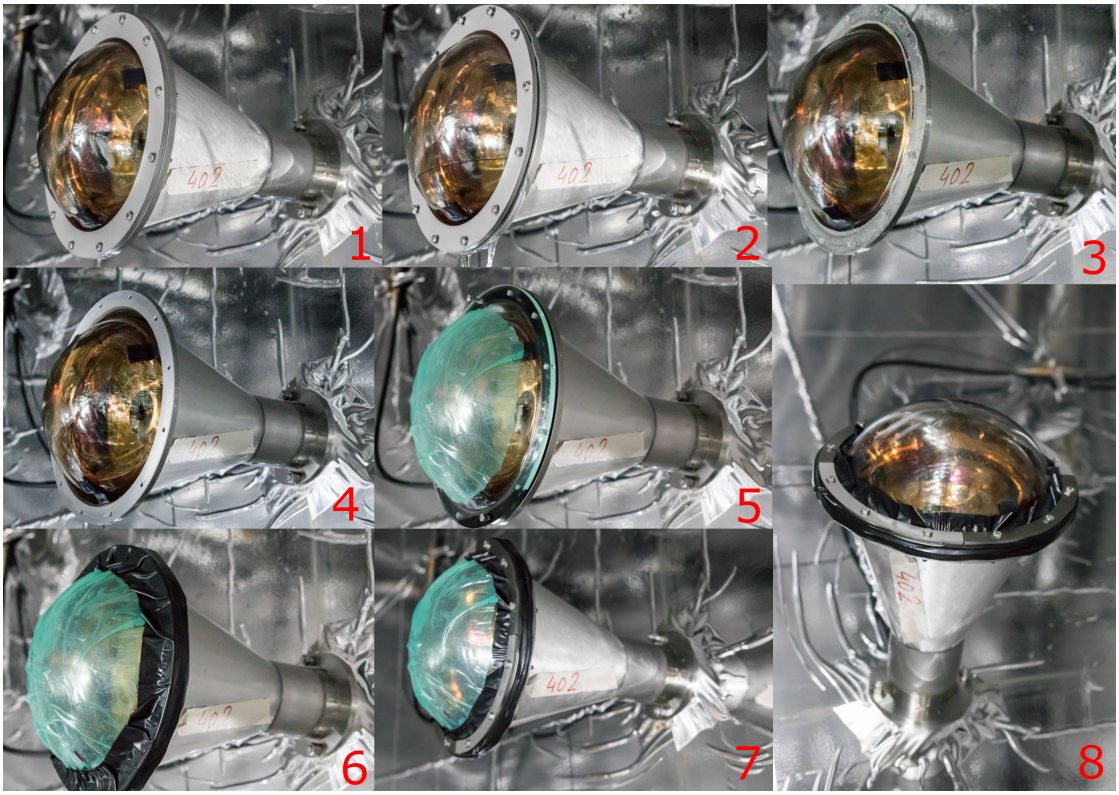

Figure 8.2: Oil removal sequence for a single PMT. 1) The initial state of the PMT with a thin PET window glued on with silicone and secured with a screwed-on metal ring. 2) The screws are loosened to remove the cap and drain the oil. The oil was catched in a bucket and the bucket emptied into waste disposal outside of the water tank. 3) The holding ring is removed, the PMT is only covered by the PET window with broken sealing. 4) The PET window is also removed, the PMT is bare. 5) The new thick acrylic cap is placed with a rubber sealing inbetween PMT capsule and acrylic covering. 6) The connection between PMT and acrylic cap is covered in butyl tape. The tape also covers the the threads on the bottom of the PMT so that when it is pierced for screwing everything down part of the butyl will enter the threads and provide sealing there. 7) New quarter rings for pressing everything together are screwed in, in contrast to the inital setting also on the bottom of the connection. 8) Finished PMT with protection foil of the acrylic peeled off.

GERDA setup (and therefore also LEGEND-200) the setup shown yields pulses with a length of $T_{\text{LED pulse}} \approx 20\,\text{ns}$. The pulse duration is independent of the duration and flank steepness of the logic signal as long as the logic signal is sufficiently long to discharge the capacitor through the LED. This relaxes the requirements towards input pulses significantly. For a calibration run of the muon veto the logic signal is connected to an auxiliary channel of the DAQ for the muon veto, which then works as a trigger for the entire system. Waveforms from all PMTs are stored

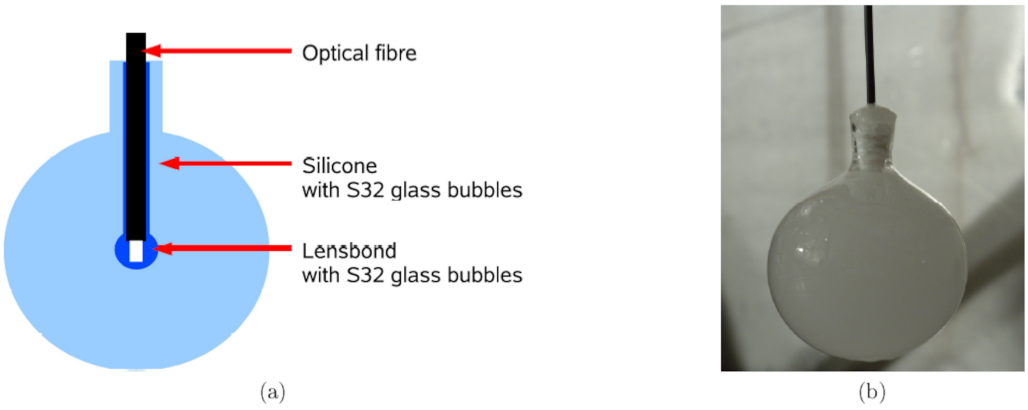

Figure 8.3: Diffusor ball used for PMT calibration. a) Sketch of a diffusor ball used in GERDA and migrated to LEGEND-200. b) Picture of a diffusor ball used in GERDA and migrated to LEGEND-200. Both taken from [22].

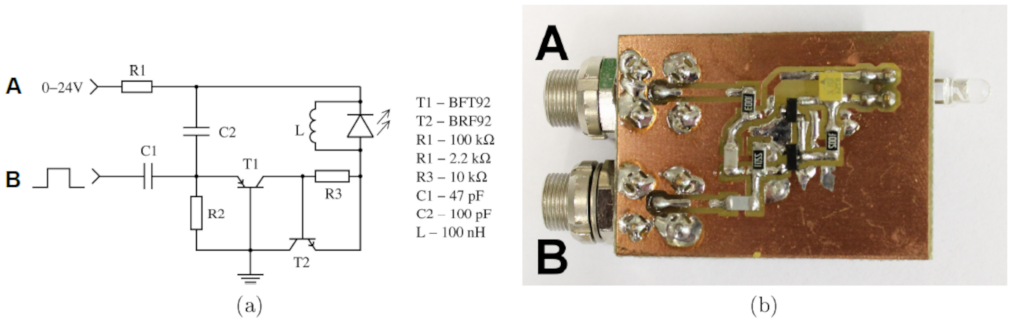

Figure 8.4: PCB used to drive the pulsing of the UV LEDs. a) Wiring diagram for the PCB used to drive the pulsing of the UV LEDs. b) Manufactured PCB used to drive the pulsing of the UV LEDs. Both taken from [30].

when a logic signal is applied to the auxiliary channel. DAC values for the diffusor balls are set so low that in every pulser event not every PMT gets hit by a photon. This way the charge histogram for every PMT will contain the pedestal from noise as well as the single photo electron (SPE) peak, giving information about both in one measurement.

The DAC and the pulser were both removed from the experimental setup, since the electronics crate they were placed in was removed. This resulted in the need for a smaller control setup, for convenience of interfacing with the master electronics also equipped with a LAN port. To realize this setup a Raspberry Pi 4 with 4 GB of RAM in combination with several Intergrated Circuits

(IC) was used. The Raspberry Pi itself is used as a pulser with the "pigpio" library for the Python programming language [21]. This enables the Raspberry to produce square pulses using its logic pins. This generates a pulse with a width of 1 μs which is then fed into a clock buffer to distribute the pulse to the PCBs. The clock buffer has an "activate" input terminal, only distributing the clock signal if that terminal is set to logic high. The outputs of clock buffer IC are fed into two quad operational amplifiers OPA4820ID to make sure to drive the currents necessary to switch the transistors in the driver PCB. Below output frequencies of 100 Hz instabilites in the pulse generation occured. Therefore the frequency was set to 100 Hz. Higher frequencies are possible, but the time for recharging the main capacitor between pulses must remain sufficient. For the DAC a digital potentiometer with a total resistance of 100 kΩ and resolution of 8 bits with a DC power supply with 12 V connected to its terminals. The wiper contact then allows to set voltages between 0 V and 12 V in $2^8 = 256$ steps. This means that there is also a relatively large resistance in series with the capacitor to be charged by this voltage. The capacity is $C = 100\,\mathrm{pF}$, the series resistance is in the worst case $R_{\text{series, max}} = R_{\text{pot}} + R_1 \approx 100\,\mathrm{k\Omega} + 100\,\mathrm{k\Omega} \approx 200\,\mathrm{k\Omega}$ (total potentiometer resistance and resistor on the PCB) and in the best case $R_{\text{series, min}} = R_1 = 100\,\mathrm{k\Omega}$ (no contribution from the potentiometer). The time constant τ_{charge} for the charging of the capacitor is then given as

$$\tau_{\text{charge, min}} = R_{\text{series, min}} \cdot C \approx 1\,\mu\mathrm{s} \text{ and } \tau_{\text{charge, max}} = R_{\text{series, max}} \cdot C \approx 2\,\mu\mathrm{s}. \tag{8.1}$$

With a period $T_{\text{pulser}} = 0.01\,\mathrm{s}$ and a duty cycle of $D = 1\,\%$ the time for the capacitor to recharge between pulses amounts to

$$t_{\text{recharging}} = (1 - D) \cdot T_{\text{pulser}} = 0.0099\,\mathrm{s} = 9900\,\mu\mathrm{s} \gg \tau_{\text{max}}. \tag{8.2}$$

So the time for recharging is much larger than the charging time constant and the capacitor gets fully charged between two subsequent pulses. The power dissipation P_{diss} of running the voltage U to ground through R_{pot} can be calculated as

$$P_{\text{diss}} = U \cdot R_{\text{pot}} = \frac{U^2}{R_{\text{pot}}} \approx 1.44\,\mathrm{mW} \quad \text{and therefore} \tag{8.3}$$

$$P_{\text{tot}} = 5 \cdot P_{\text{diss}} \approx 7.2\,\mathrm{mW}, \tag{8.4}$$

so not significantly contributing to the power draw that mostly comes from the 15 W of the Raspberry Pi power supply.

A wiring diagram for the new calibration control for the muon veto can be seen in figure 8.5. A picture of the elements of the control and the finished control can be seen in figure 8.6.

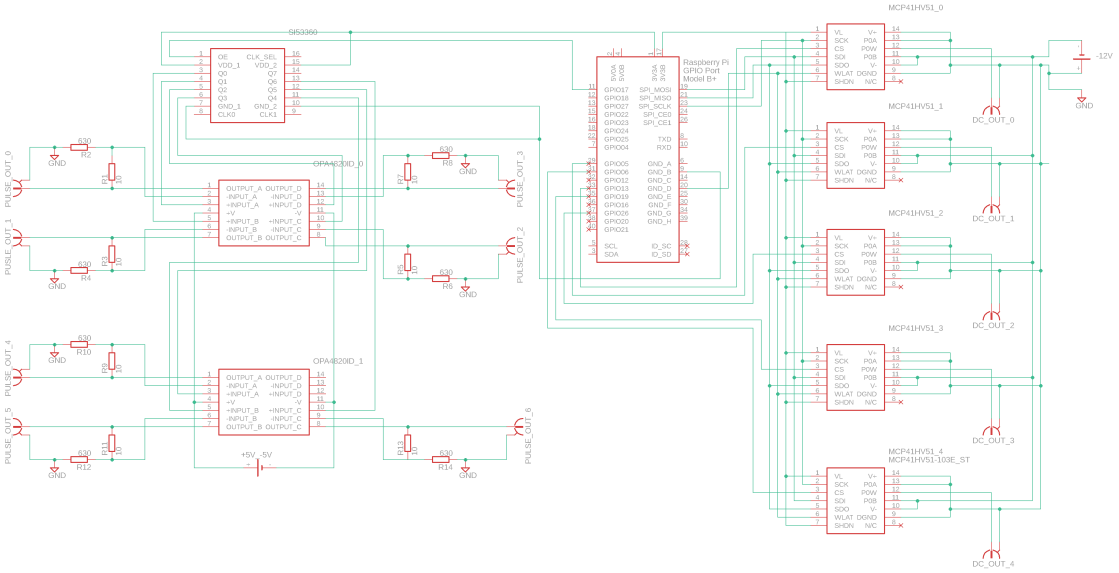

Figure 8.5: Wiring diagram of the new calibration control electronics. All connections from the Raspberry Pi are done with breadboard plugs in order to increase flexibility for maintenance directly in the tunnel at LNGS. Connections from the circuit boards are soldered for increased stability. For operation the pulse is generated by the Raspberry Pi on its GPIO pin 04 and the "ENABLE" port on the clock buffer SI53360 is pulled to "logic high" from its usual "logic low" state to enable the buffer. The pulse is fed into the clock buffer to get 8 outputs in phase. These multiplied pulses are then fed into two OPA4820ID quad operational amplifiers with a gain g of $g \sim 1$. The operational amplifiers make sure that the pulses can drive enough current to switch the transistors on the PCB of the LED. After operation pulse generation on the Raspberry Pi is stopped and the "ENABLE" port is again pulled to its usual "logic low." Power to the clock buffer is supplied by one of the 3.3 V ports on the Raspberry Pi. Power to the operational amplifiers is provided by a $+5\,\mathrm{V} - 5\,\mathrm{V}$ power suplly which is in turn powered by the power supply of the voltage applied to the potentiometers.
The digital potentiometers are daisy chained to the designated SPI pins of the Raspberry Pi. Only the chip select ($\bar{CS}$) is connected for each output individually to the GPIO pins 13, 05, 26, 19 and 06. For operation (i.e. to control a single potentiometer) the respective $\bar{CS}$ pin is pulled to "logic low" from its normal "logic high" state in order to make the potentiometer listen to the SPI commands coming in. Then the SPI command is sent (in normal operation only "set resistance" commands) and the $\bar{CS}$ pin is pulled to "logic high" again. This results in a voltage between the potentiometer wiper and GND proportional to the resistance set between the two ports. The logic voltage to the potentiometers is supplied directly by one of the 3.3 V ports on the Raspberry Pi. The power supply and also voltage between the terminals of the potentiometers is provided by an external 12 V switching power supply.

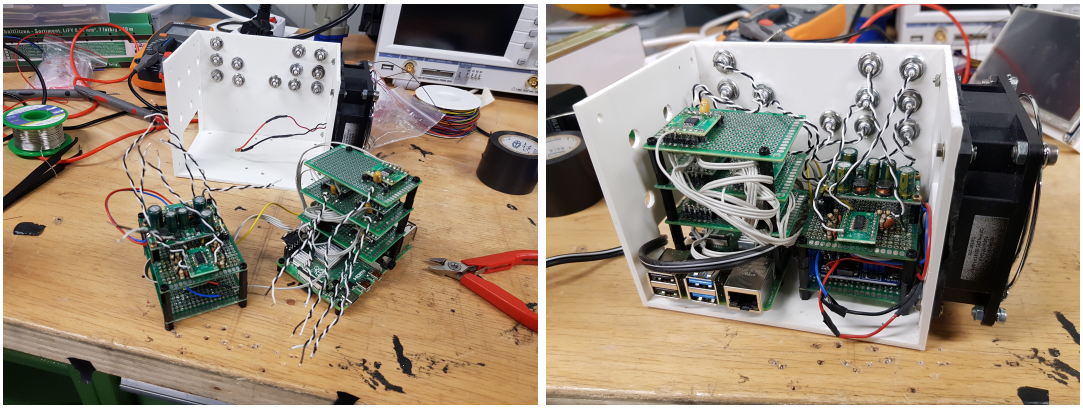

Figure 8.6: Left: Picture of the single components of the calibration control. On the left side of the picture the clock buffer including its power supply can be seen as stacked circuit boards. On the right side the 5 digital potentiometers on their circuit boards can be seen stacked onto the Raspberry Pi. In the background there is the 3D printed case for the pulser control with an opening for the power plug as well as the USB and HDMI ports of the Raspberry Pi on the left. On the side facing the camera the LEMO sockets for DC voltage out and square pulses output can be seen. The side on the right houses a fan to cool the entire system with air holes on the opposing side.
Right: The system mounted into the case. The closing lid of the case (not shown) houses a 5" TFT display connected to the Raspberry Pi for easier debugging and maintenace in-place.

8.3 Determination of new majority levels for the pillbox

After increasing the number of PMTs inside the pillbox, the rate in this crucial part of the muon veto showed a high excess when compared to GERDA. The PMTs on the floor and the wall of the water tank were in good agreement with the expectation from GERDA. The initial response to this excess in order to enable the including of the muon veto into the data stream and also the event building was to use a place holder trigger condition. Only the 4 PMTs which had been in the pillbox already for GERDA and were still working for generating a trigger from the pillbox. Still all the PMTs were read out in the event of a trigger. This condition reduced the rate to about 0.43 Hz which was low enough to not produce excessive amounts of data. In order to decide on a new trigger condition for the pillbox several runs of data taking ran during commissioning of LEGEND-200 were analysed. Due to the high density of data taking events for commissioning the entire LEGEND-200 system, it was not feasible to have muon veto-only runs with high enough statistics. Instead some the data recorded during the commissioning runs was masked with different trigger conditions so that only events fulfilling these conditions were

considered in their respective analysis. The data considered in the beginning is from the runs 015 to 017 of data taking period p02. After the realization that these runs are not suitable for this work, runs 018 and 019 from the same period were considered. The problem considering runs 015 to 017 can be seen in figure 8.7. The datasets contain disturbances with unclear sources, namely three time periods with very narrow bands of total light and a kink in minimum total light. While the exact sources remain unknown, these features coincide with commissioning work carried out in the cleanroom of LEGEND-200. In contrast to that no such disturbances can be seen in the data for runs 018 and 019 as can be seen in figure 8.8.

During the analysis the only parameter changed for the masking process was the majority level for the pillbox PMTs. In the DAQ the necessary level was set to 3 out of 4 GERDA PMTs for the pillbox, for the wall PMTs the majority level was set to 4 out of 20 PMTs and for the bottom to 4 out of 23 PMTs. This analysis can give a good estimate on what fraction of the recorded data is physics and therefore assist in the selection of a new majority level condition for the pillbox.

The motivation to change the trigger conditions of the muon veto arises already if one considers the total amount of light produced in the individual events of the muon veto. Two histograms for the data of run 018 and 019 can be seen in figure 8.9. One contains all the events recorded in run 018 and 019 and the other the subset of these events which are considered to be muons. The conditions to be a muon are either a total multiplicity of at least 10 PMTs or total light of at least 30 p.e. or both. These conditions are set in this way to cut the low multiplicity bump out of all events recorded. This is visualized in figure 8.10. The low multiplicity bump is clearly visible as region with large excess of counts in the bottom left, enclosed by a box marking the conditions an event has to fulfill to be considered a muon. The basis for the following analysis is that the place holder trigger condition for the muon veto is very loose. Selecting a subset fulfilling more stringent trigger conditions therefore only makes a small error in estimating the new possible trigger conditions. Additionally, the effect of random coincidences becomes increasingly less important for higher majority levels. For a majority level of 3 out of 10 pillbox PMTs the rate of random coincidences $R_{\text{rand, 3/10}}$ can be estimated to

$$R_{\text{rand, 3/10}} = \binom{10}{3} \cdot R_{\text{dark}}^3 \cdot t_{\text{coinc}}^2 \approx 93\,\text{mHz} \tag{8.5}$$

with a dark count rate $R_{\text{dark}} = 6000\,\text{Hz}$ and a coincidence window of $t_{\text{coinc}} = 60\,\text{ns}$. This rate is comparable to the rate of the muon veto with place holder trigger conditions. The random rate

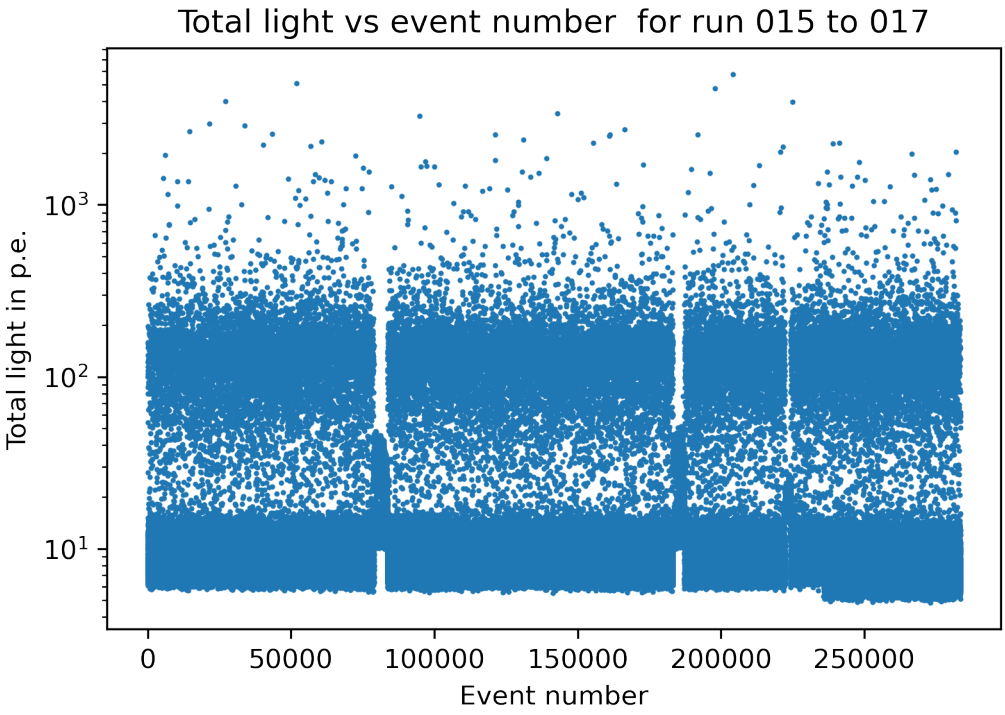

Figure 8.7: Integral light of the individual events plotted as a function of the event number for runs 015 to 017. Three periods with a very narrow band of integral light can be observed as well as a step in minimum integral light around event number 230000. The exact reasons for these periods and the step are unclear, but they coincide with commissioning work carried out in the cleanroom of the LEGEND-200 experiment.

$R_{\text{rand, 4/10}}$ for a majority level of 4 out of 10 pillbox PMTs is only

$$R_{\text{rand, 4/10}} = \binom{10}{4} \cdot R_{\text{dark}}^4 \cdot t_{\text{coinc}}^3 \approx 0.059\,\text{mHz}. \tag{8.6}$$

This rate decreases further for higher majority levels and can therefore be neglected for sufficient majority levels.

For the exploration of other majority levels only the fraction meeting these conditions of the total recorded events was considered ("fake data"). The amount of muons and the spectral shape of the total amount of light was then compared to the muons of the entire dataset. Also the rate for the individual PMTs was estimated as the number of fake triggers of the PMT dividided by the total duration of data taking. This was carried out for majority levels of 5, 6, 7, 8, 9 and 10 out of 10 pillbox PMTs. The results can be seen in figures 8.11, 8.12, 8.13, 8.14, 8.15 and 8.16.

For every majority level considered some events that were still recorded with the low level would

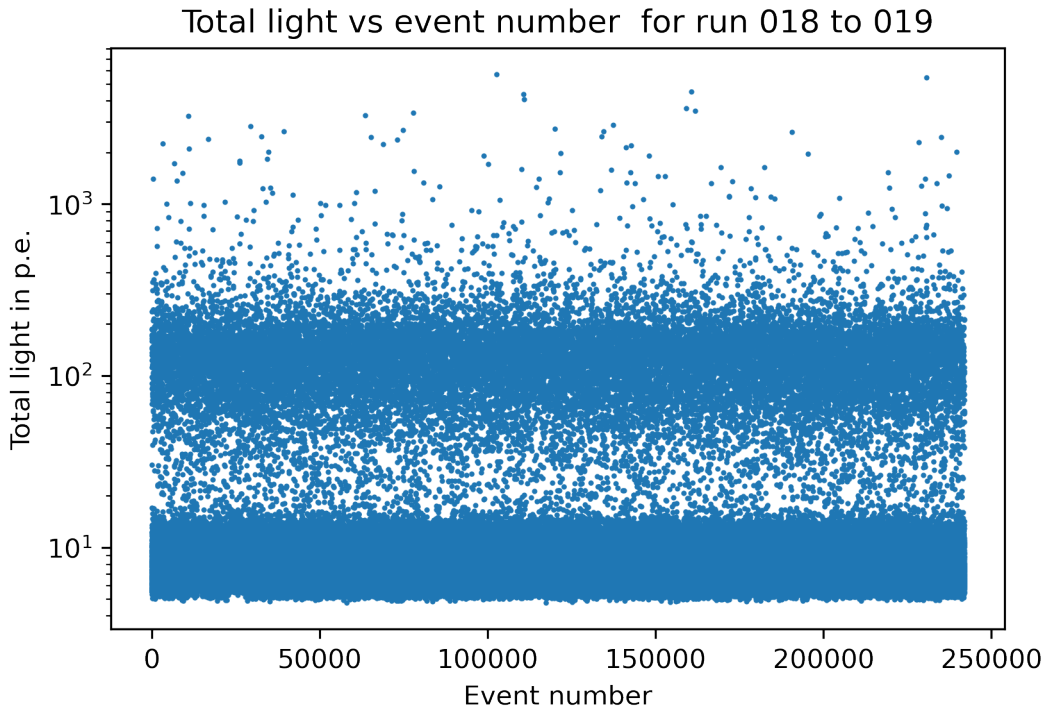

Figure 8.8: Integral light of the individual events plotted as a function of the event number for runs 018 and 019. This data does not show similar features to run 015 to 017 but appears stable.

not have been recorded. For majority levels of 5 and 6 out of 10 this concerns only two events very close to the border of even being a muon. Therefore these majority levels can be labeled safe. For higher majority levels the amount of muons not recorded increases, therefore these levels were considered not safe enough. The decision between the majority levels of 5 and 6 was made based on the individual rates of the PMTs. For a majority level of 5 out of 10 the PMTs relevant for trigger generation are clearly visible still, due to combinatorics. For a majority level of 6 the dominance of the trigger generating PMTs is reduced and the rate for the PMTs lies around 40 mHz. Therefore the decision was made to set the majority level to 6 out of 10 PMTs and continue data taking with this condition. This data was taken in run 020, for which several key characteristics were produced. The visualization of total multiplicity and total light can be seen in figure 8.17. The total light as a function of the event number can be seen in figure 8.18. The individual PMT rates can be seen in 8.19. The DAQ trigger rate of the muon veto system is reduced to 62.4 mHz [10]. Total multiplicity and amount of light look as expected from run 018 and 019, only the low multiplicity bump is less prominent (as intended). No disturbances as

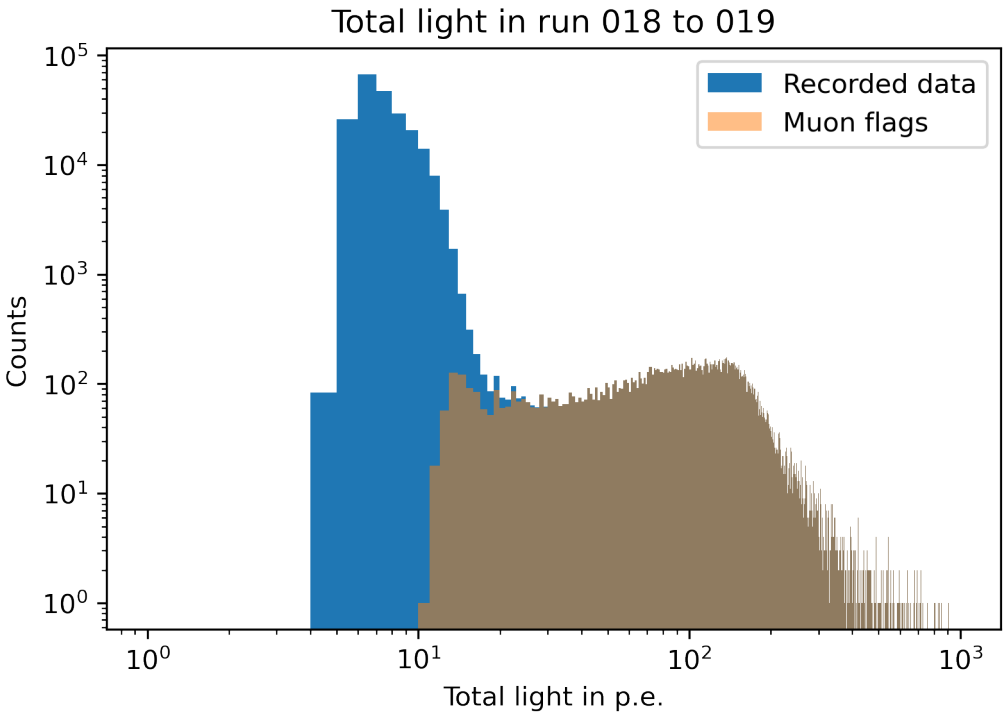

Figure 8.9: Histograms of the total recorded events of run 018 and 019 and the events of that which are considered to be muons. The condition to be considered a muon is a total multiplicity of at least 10 PMTs or a total light of at least 30 photo electrons. A surplus of events with very low light can be clearly seen around 10 p.e. which stems from the low multiplicity bump.

in runs 015 to 017 can be observed in the same plot for run 020. The individual PMT rates are now comparable for every PMT in the muon veto, matching expectations from GERDA. Overall the results of the new majority level for the pillbox produce the desired results and will be used for the muon veto going forward.

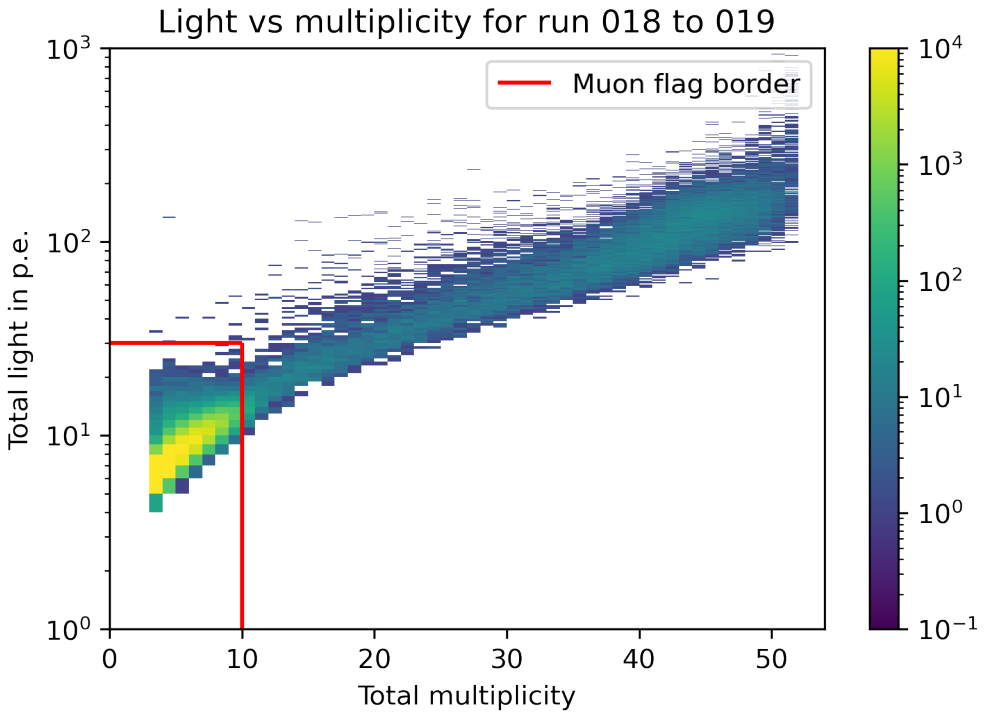

Figure 8.10: Visualisation of the muon conditions. Every event outside of the red box in the lower left is considered a muon. The box contains most of the events stemming from the low multiplicity bump which is clearly visible as region with a large excess of counts.

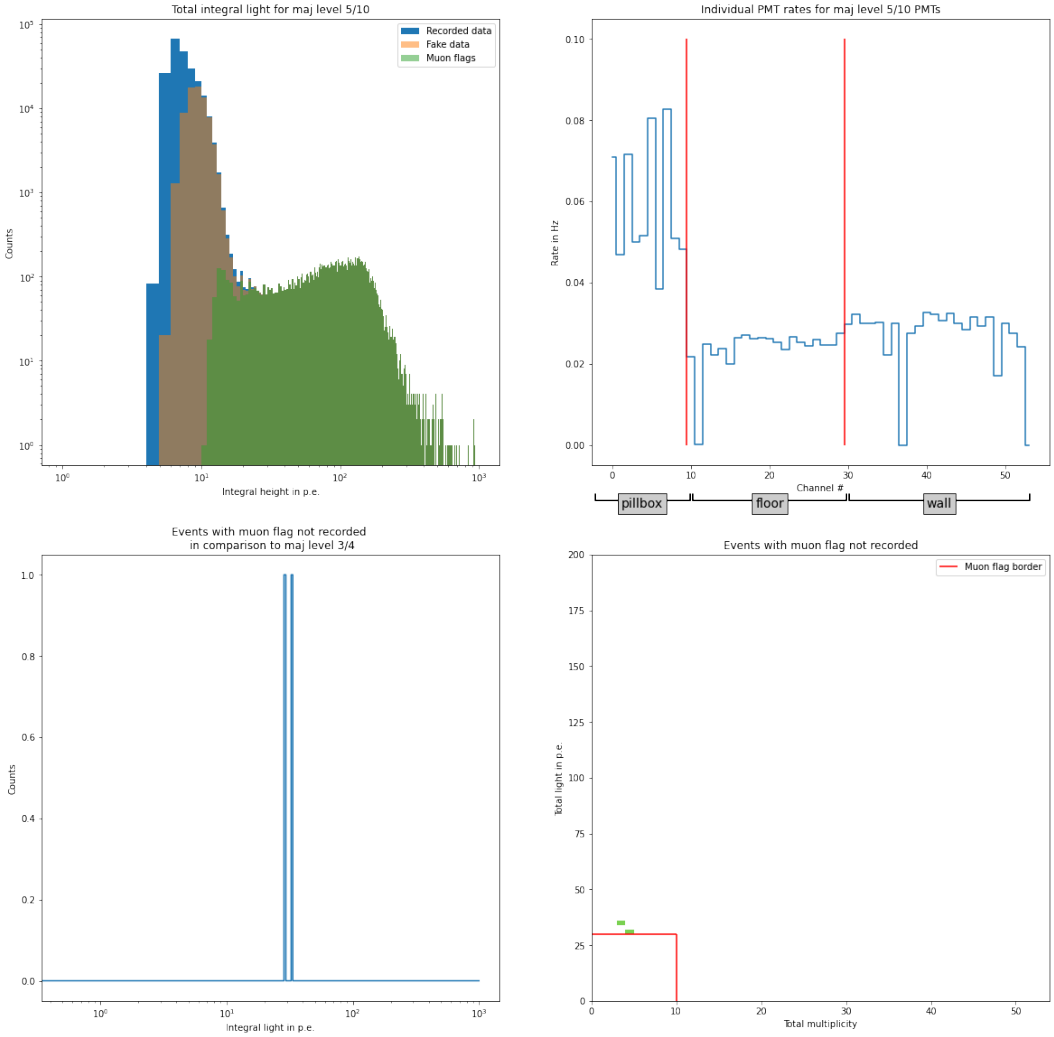

Figure 8.11: Results of the analysis for a majority level of 5 out of 10 pillbox PMTs. Top left: Histograms of all recorded data (blue), the subset of data fulfilling a more strict trigger condition (orange) and the events flagged as muons (green). The spectral shape of the muons is conserved. Bottom left: Difference between the histogram of muons in the recorded data and the muons in the data fulfilling the more strict trigger conditions. Only 2 events flagged as muons in the total recorded data would not have been recorded. Top right: Trigger rate in the individual PMTs if only the events fulfilling the more strict trigger conditions were recorded. The surface on which the PMTs are mounted is indicated on the bottom. A strong excess in the pillbox can still be observed. Bottom right: Total PMT multiplicity and integral light for all the events that would not have been recorded with more strict trigger conditions. In red the region in which events are not considered muons is shown. The events that would not have been recorded are very close to the border and therefore are not considered problematic. The rate of fake data for this majority level was calculated to $R_{5/10} \approx 123.5\,\mathrm{mHz}$.

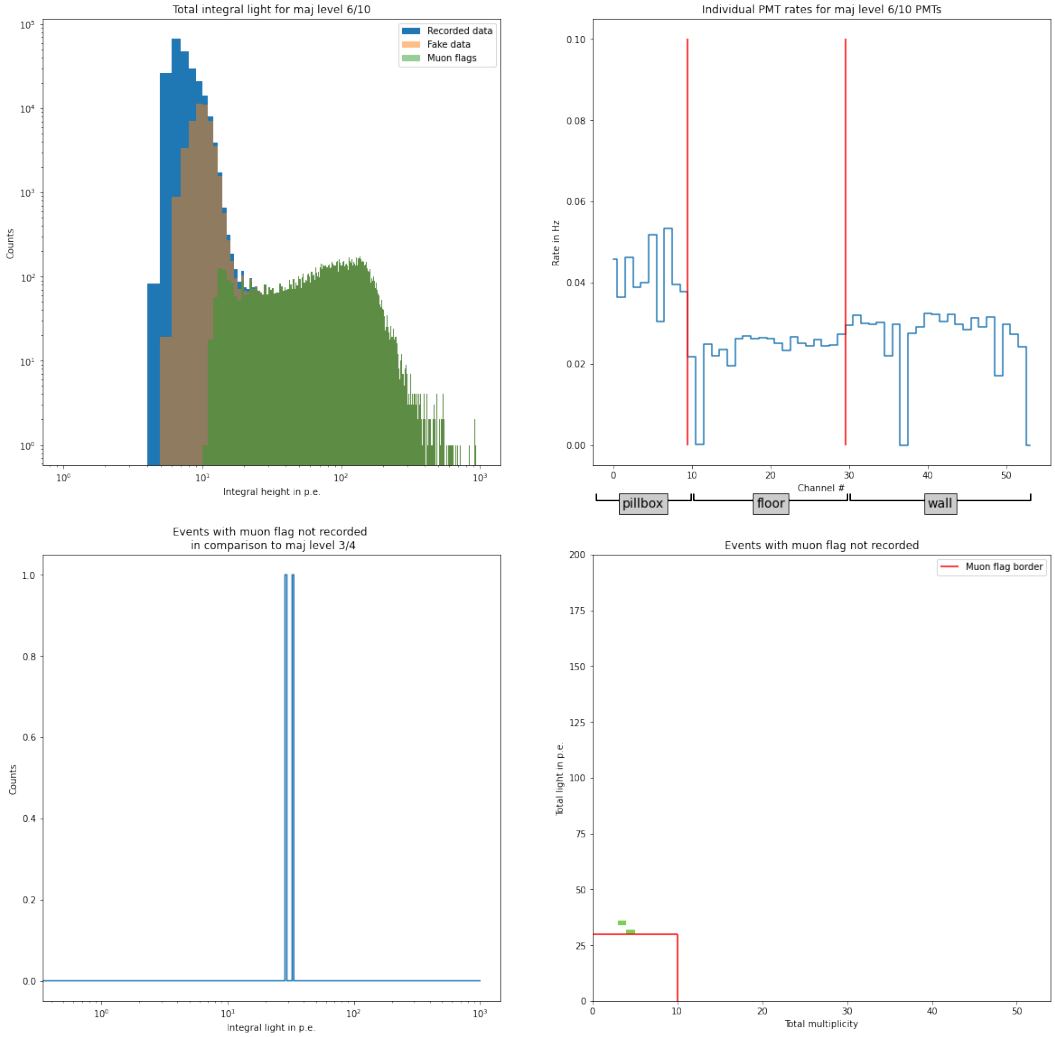

Figure 8.12: Results of the analysis for a majority level of 6 out of 10 pillbox PMTs. Top left: Histograms of all recorded data (blue), the subset of data fulfilling a more strict trigger condition (orange) and the events flagged as muons (green). The spectral shape of the muons is conserved. Bottom left: Difference between the histogram of muons in the recorded data and the muons in the data fulfilling the more strict trigger conditions. Only 2 events flagged as muons in the total recorded data would not have been recorded. Top right: Trigger rate in the individual PMTs if only the events fulfilling the more strict trigger conditions were recorded. The surface on which the PMTs are mounted is indicated on the bottom. A strong excess in the pillbox can still be observed. Bottom right: Total PMT multiplicity and integral light for all the events that would not have been recorded with more strict trigger conditions. In red the region in which events are not considered muons is shown. The events that would not have been recorded are very close to the border and therefore are not considered problematic. The rate of fake data for this majority level was calculated to $R_{6/10} \approx 89.1\,\mathrm{mHz}$.

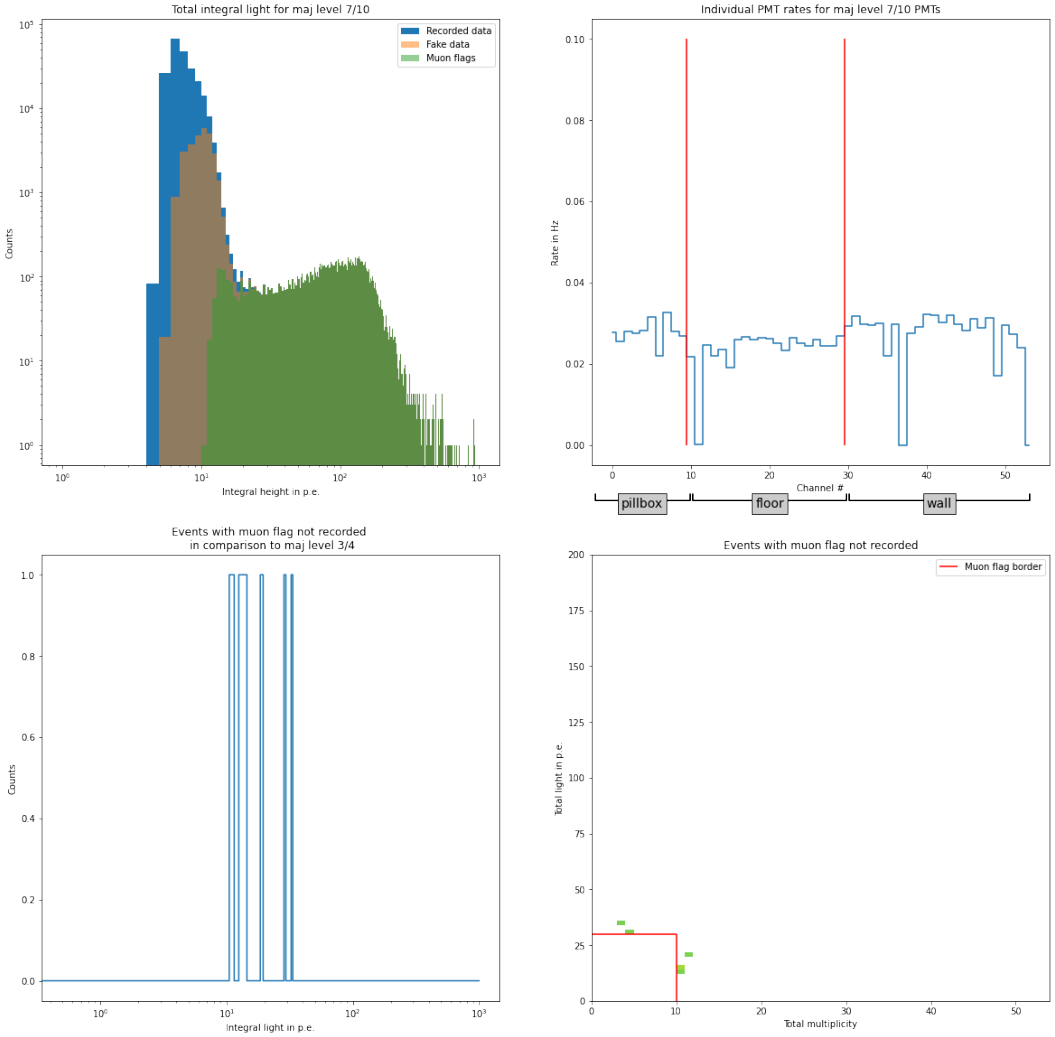

Figure 8.13: Results of the analysis for a majority level of 7 out of 10 pillbox PMTs. Top left: Histograms of all recorded data (blue), the subset of data fulfilling a more strict trigger condition (orange) and the events flagged as muons (green). The spectral shape of the muons is conserved. Bottom left: Difference between the histogram of muons in the recorded data and the muons in the data fulfilling the more strict trigger conditions. 8 events flagged as muons in the total recorded data would not have been recorded. Top right: Trigger rate in the individual PMTs if only the events fulfilling the more strict trigger conditions were recorded. The surface on which the PMTs are mounted is indicated on the bottom. No excess in the pillbox can be observed. Bottom right: Total PMT multiplicity and integral light for all the events that would not have been recorded with more strict trigger conditions. In red the region in which events are not considered muons is shown. The events that would not have been recorded are straying further from the border than for less strict conditions. To stay as conservative as possible these are considered dangerous. The rate of fake data for this majority level was calculated to $R_{7/10} \approx 65.3\,\mathrm{mHz}$.

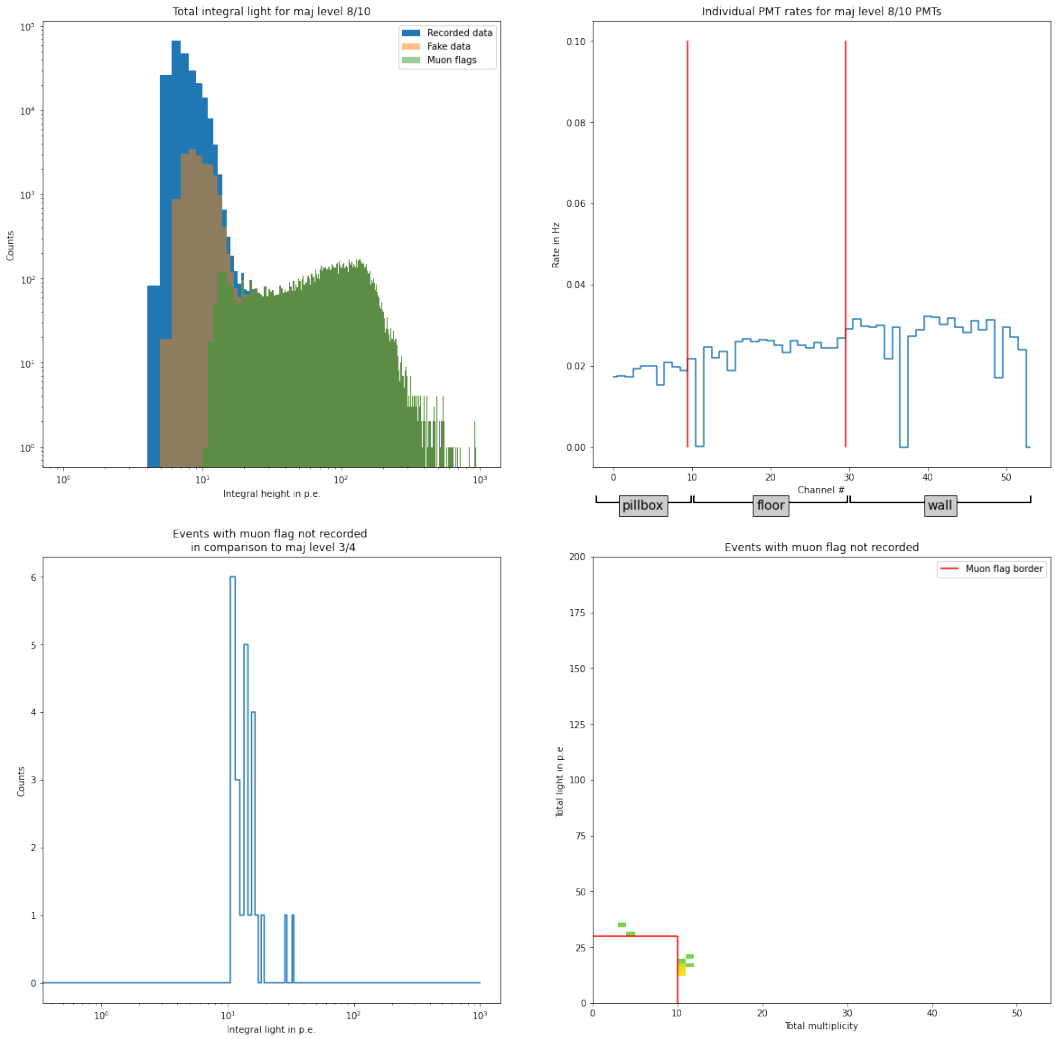

Figure 8.14: Results of the analysis for a majority level of 8 out of 10 pillbox PMTs. Top left: Histograms of all recorded data (blue), the subset of data fulfilling a more strict trigger condition (orange) and the events flagged as muons (green). The spectral shape of the muons is conserved. Bottom left: Difference between the histogram of muons in the recorded data and the muons in the data fulfilling the more strict trigger conditions. 24 events flagged as muons in the total recorded data would not have been recorded. Top right: Trigger rate in the individual PMTs if only the events fulfilling the more strict trigger conditions were recorded. The surface on which the PMTs are mounted is indicated on the bottom. A decrease in rate in the pillbox relative to the other volumes can be observed. Bottom right: Total PMT multiplicity and integral light for all the events that would not have been recorded with more strict trigger conditions. In red the region in which events are not considered muons is shown. The events that would not have been recorded are straying further from the border than for less strict conditions. To stay as conservative as possible these are considered dangerous. The rate of fake data for this majority level was calculated to $R_{8/10} \approx 52.3\,\mathrm{mHz}$.

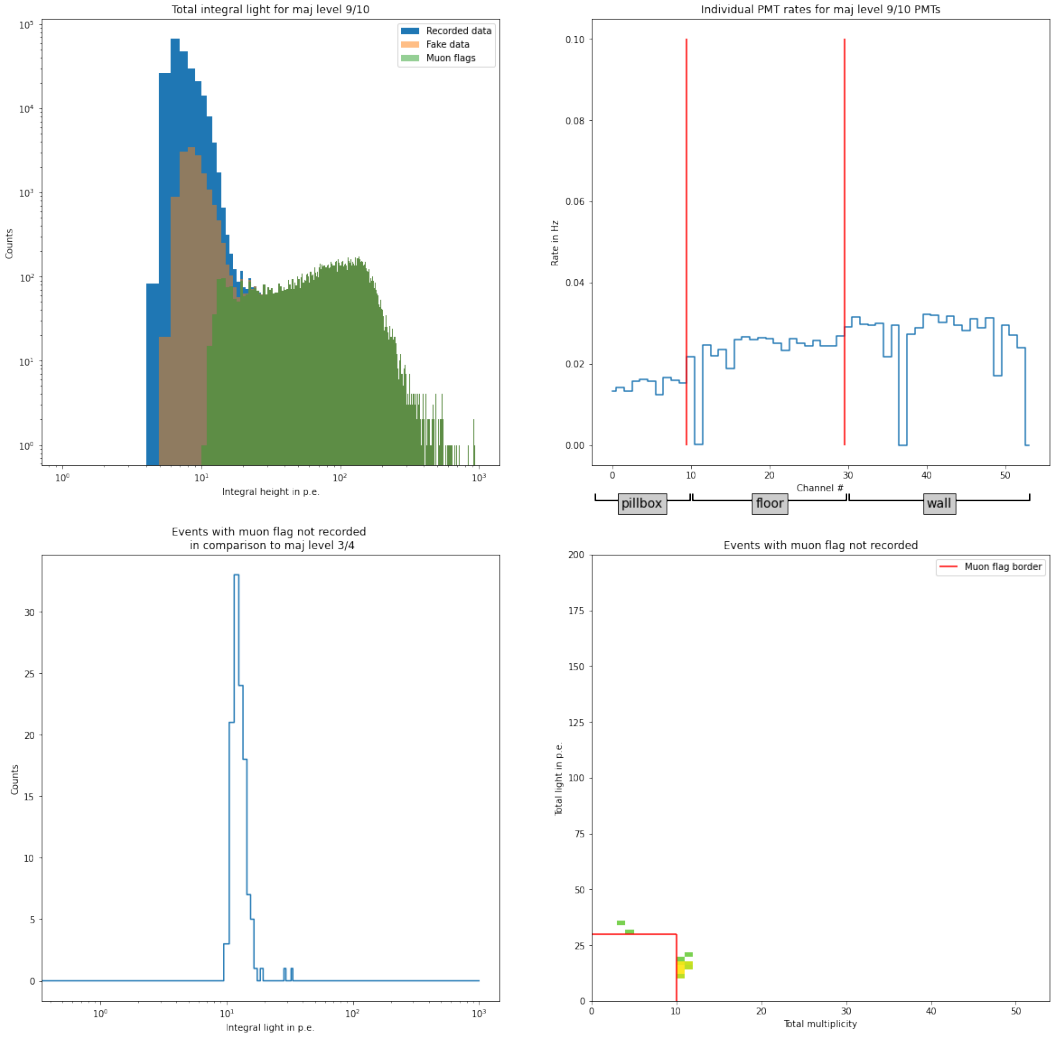

Figure 8.15: Results of the analysis for a majority level of 9 out of 10 pillbox PMTs. Top left: Histograms of all recorded data (blue), the subset of data fulfilling a more strict trigger condition (orange) and the events flagged as muons (green). The spectral shape of the muons is conserved. Bottom left: Difference between the histogram of muons in the recorded data and the muons in the data fulfilling the more strict trigger conditions. 113 events flagged as muons in the total recorded data would not have been recorded. Top right: Trigger rate in the individual PMTs if only the events fulfilling the more strict trigger conditions were recorded. The surface on which the PMTs are mounted is indicated on the bottom. A decrease in rate in the pillbox relative to the other volumes can be observed. Bottom right: Total PMT multiplicity and integral light for all the events that would not have been recorded with more strict trigger conditions. In red the region in which events are not considered muons is shown. The events that would not have been recorded are straying further from the border than for less strict conditions. To stay as conservative as possible these are considered dangerous. The rate of fake data for this majority level was calculated to $R_{9/10} \approx 47.6\,\mathrm{mHz}$.

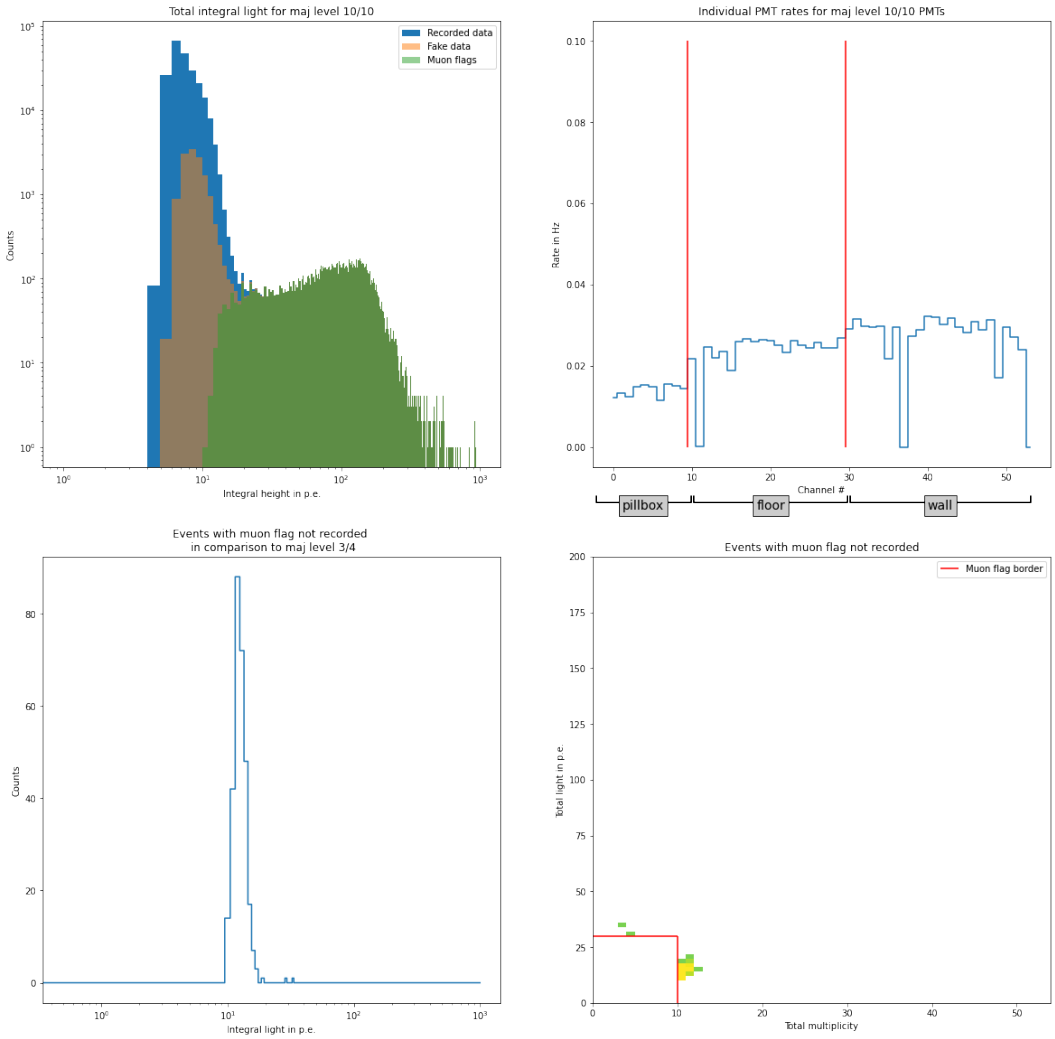

Figure 8.16: Results of the analysis for a majority level of 10 out of 10 pillbox PMTs. Top left: Histograms of all recorded data (blue), the subset of data fulfilling a more strict trigger condition (orange) and the events flagged as muons (green). The spectral shape of the muons is conserved. Bottom left: Difference between the histogram of muons in the recorded data and the muons in the data fulfilling the more strict trigger conditions. 291 events flagged as muons in the total recorded data would not have been recorded. Top right: Trigger rate in the individual PMTs if only the events fulfilling the more strict trigger conditions were recorded. The surface on which the PMTs are mounted is indicated on the bottom. A decrease in rate in the pillbox relative to the other volumes can be observed. Bottom right: Total PMT multiplicity and integral light for all the events that would not have been recorded with more strict trigger conditions. In red the region in which events are not considered muons is shown. The events that would not have been recorded are straying further from the border than for less strict conditions. To stay as conservative as possible these are considered dangerous. The rate of fake data for this majority level was calculated to $R_{10/10} \approx 46.5\,\mathrm{mHz}$.

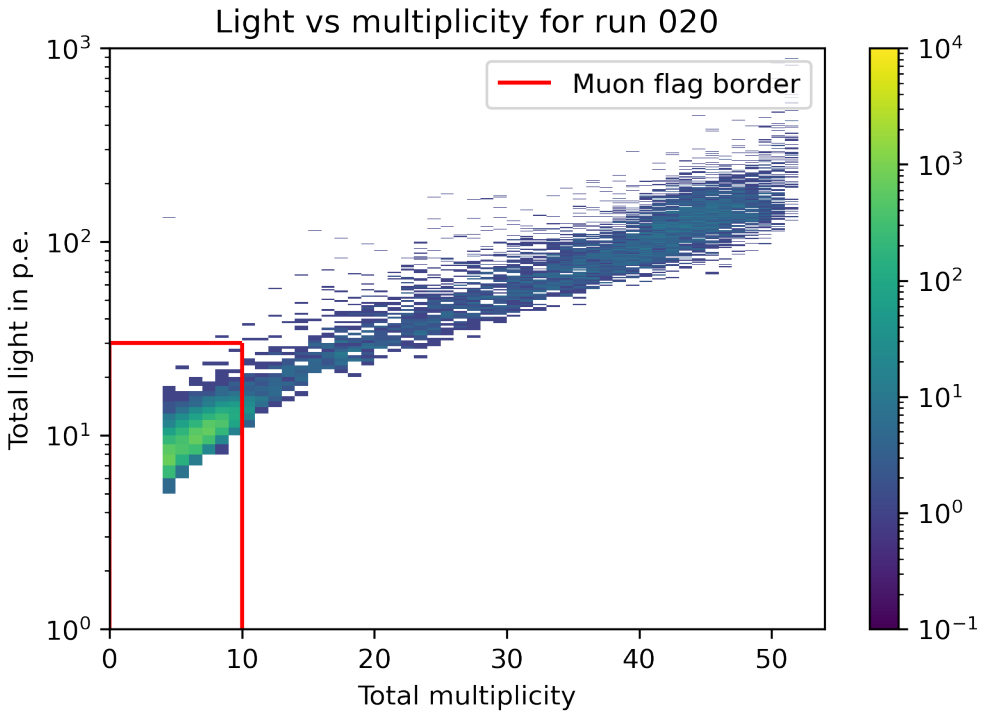

Figure 8.17: Visualisation of total multiplicity and total light for run 020. The low multiplicity bump is less prominent compared to run 018 to 019.

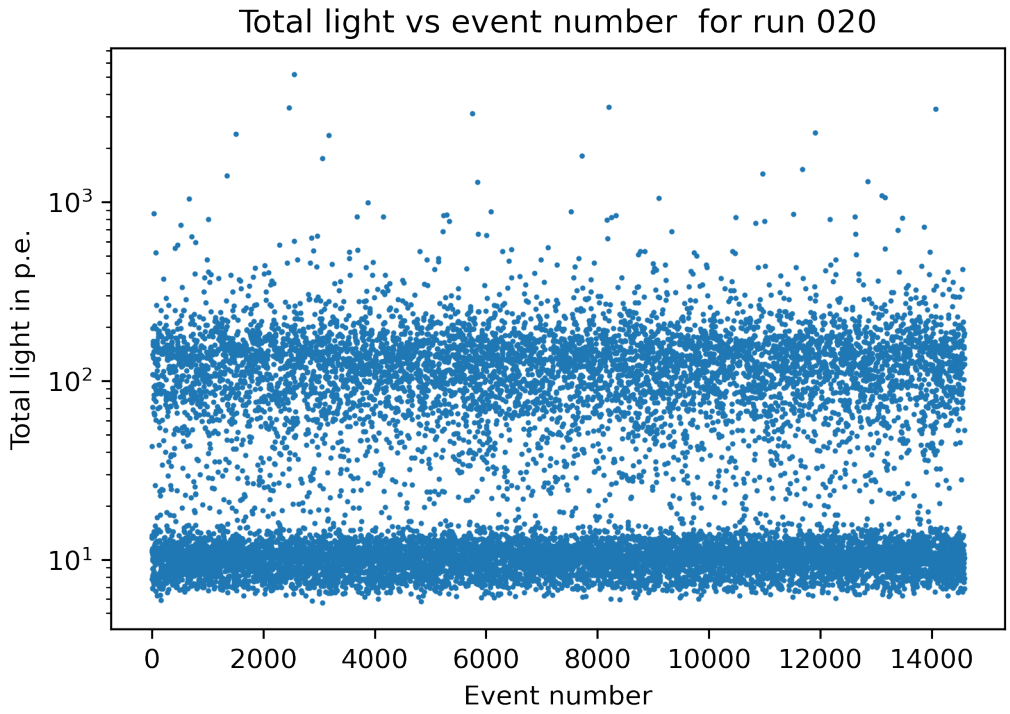

Figure 8.18: Total light as a function of the event number. No features comparable to the same data for run 015 to 017 is obersable, the veto operated in stable conditions.

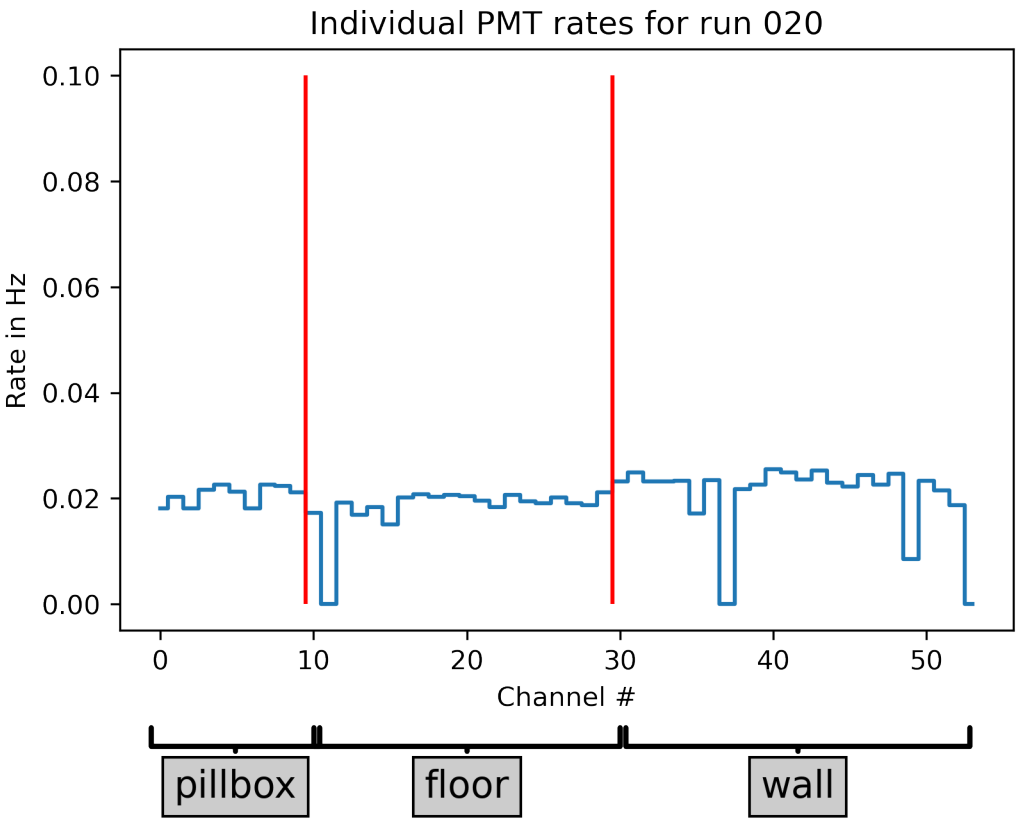

Figure 8.19: Individual rates for the PMTs in run 020. The rates are estimated as number of triggers in the PMT divided by the total duration of data taking.

9

Summary and conclusion

"Ich hab 10 Jahre geblutet, gönn' mir 5 Sekunden Flex."

- Döll, *German rapper*

Over the course of this work the pulse processing and image reconstruction of a PET scanner was implemented and validated. The pixel determination has to be done by hand for every pixel, as in many systems commercially available. The best energy resolutions achieved in this work rival the energy resolutions achieved in a PET scanner with commercial readout and data processing. A inverted coaxial shaped HPGe detector was calibrated and characterized on a very fundamental level. The energy resolution of the detector was satisfactory with being on the order of several ‰. The A/E distribution of the detector has shown no anormal features when compared to other detectors of the same kind. Both the PET scanner and the HPGe detector were later on combined in a test stand for HPGe detectors. The coincidence between both components was validated and they were arranged relative to each other and the source

in a reproducible way. A measurement with this setup was performed which could validate the proof of concept for the test stand. It is feasible to record HPGe waveforms of SSEs with known locations. The statistics are however not satisfactory for granular scans of detectors. To overcome this limitation a high activity of the source is needed since the usable solid angle is small for a collimator with only a small hole. The energy of usable γs has to be comparable to the 2614 keV or higher in order to allow for a high fraction of pair production events. Most isotopes with such high events have either low specific activity (the source becomes too big for collimator holes) or many other lower energy γ lines (producing a lot of background or pile-ups) or both. One method to be explored in future work should therefore be the production of radioacitve isotopes with high activity and best case only a single high energy γ line. This can potentially speed up scans of a detector significantly and in the long run validate pulse shape simulations which become increasingly important for reducing backgrounds in germanium based neutrinoless double beta decay events.

As an additional way to reduce the background in LEGEND-200 several commissioning activities were carried out. Together with other people of the University of Tübingen the spectroscopy oil in the PMT encapsulations of the PMTs in the Cherenkov muon veto was removed due to environmental concerns. Some of the PMTs were relocated to the critical veto volume called the pillbox. Additionally a new remote control for the existing calibration setup of the muon veto was produced and tested. Finally the trigger conditions for the pillbox were updated since it became too sensitive with all the PMTs relocated there. The collection of this commissioning work ensures (among other work) the functionality of the cherenkov muon veto for LEGEND-200.

Danksagung

Ich bedanke mich bei Prof. Josef Jochum für die Gelegenheit diese Arbeit bei ihm durchzuführen. Er stand mir stets mit hilfreichen Ratschlägen oder aufbauenden Worten zur Seite und brachte mir immer großes Verständnis entgegen.
Ich bedanke mich bei Prof. Tobias Lachenmaier für die Zweitbetreuung.
Ich bedanke mich bei Gaby Behring für eine unglaubliche Verwaltung.
Ich bedanke mich bei meiner Mutter Brigitte Rauscher für das Gefühl in Ordnung zu sein und geliebt zu werden. Auch für jeden Kampf den sie für mich gefochten hat und alle Arbeit die sie mir abgenommen hat.
Ich bedanke mich bei meinem Vater Frank Rauscher für lehrreiche Arbeitseinsätze und dadurch meine Charakterbildung.
Ich bedanke mich bei meiner Partnerin Gina Grünauer für nicht weniger als die Rettung meiner Zukunft und die Schenkung eines neuen Zuhauses.
Ich bedanke mich bei Marlene Topka für Unterstützung in meiner dunkelsten Zeit.
Ich bedanke mich bei Ivana Nikolac für gegenseitigen emotionalen Support.
Ich bedanke mich bei meiner Schwester Jana Rauscher für das normal sein in dieser Familie.
Ich bedanke mich bei meinem Bruder Johannes Rauscher für gegenseitige Akzeptanz.
Ich bedanke mich bei meinem Schwager in spe Sebastian Staneker für sein Interesse an YouTubern.
Ich bedanke mich bei Büsra Hess für eine sehr gute Betreuung.
Ich bedanke mich bei Tobias Heinz für das Ertragen meiner Mitbewohnerschaft.
Ich bedanke mich bei Tobias Sterr für stets anregende Gespräche.
Ich bedanke mich bei Marc Breisch als Stimme der Vernunft.
Ich bedanke mich bei Ann-Kathrin Schütz für das gemeinsame Leiden.
Ich bedanke mich bei Katharina Kilgus für eine gemeinsame unnötige Italien-Reise.

Ich bedanke mich bei Jessica Eck für seltene aber gute Gespräche.

Ich bedanke mich bei Benedict Kaiser für komplett unsinnige Gespräche.

Ich bedanke mich bei Sarah Kuckuck für's gemeinsam seltsam sein.

Ich bedanke mich bei Torsten Hehl für sehr lehrreiche Unterhaltungen.

Ich bedanke mich bei Heiko Salzmann für viele Unterhaltungen oberhalb Zimmerlautstärke.

Ich bedanke mich bei Konrad Gülicher für Terminator 2.

Ich bedanke mich bei Leo Schröppel für GNTM.

Ich bedanke mich bei Jana Fischer für ihren Spott.

Ich bedanke mich bei Florian Oberle (und Konrad) für das Bestehen meiner Analysis-Module.

Ich bedanke mich bei Georg Stadelmann für sein Ding.

Ich bedanke mich bei Fabian Leuschner als Beispiel für innere Ruhe in egal welcher Situation.

Bibliography

[1] Nuclear medicine pioneer, hal o. anger, 1920–2005. *Journal of Nuclear Medicine Technology*, 33(4):250–253, 2005.

[2] M. et al. Agostini. Results on $\beta\beta$ decay with emission of two neutrinos or majorons in ^{76}ge from gerda phase i. *The European Physical Journal C*, 75(9):416, Sep 2015.

[3] Matteo Agostini, M. Allardt, Erica Andreotti, A. Bakalyarov, M. Balata, I. Barabanov, M. Heider, Nuno Barros, L. Baudis, C. Bauer, N. Becerici-Schmidt, E. Bellotti, S. Belogurov, S. Belyaev, Giovanni Benato, Alessandro Bettini, Leonid Bezrukov, T. Bode, V. Brudanin, and G. Zuzel. Pulse shape discrimination for gerda phase i data. *European Physical Journal C*, 73:2583, 10 2013.

[4] Matteo Agostini, Giovanni Benato, and Jason A. Detwiler. Discovery probability of next-generation neutrinoless double-beta-decay experiments. *Physical Review D*, 96(5), sep 2017.

[5] Matteo Agostini, Jason Detwiler, Luigi Pertoldi, Ian Guinn, George Marshall, Valerio D'Andrea, Patrick Krause, Grace Song, Erin Engelhardt, Sam Borden, Rosanna Deckert, David Sweigart, Andreas Zschocke, Clint Wiseman, Tim Mathew, Yoann Kermaïdic, and Ben Shanks. pygama, March 2024.

[6] Sigma Aldrich. Infrared spectroscopy oil 161403-208l data sheet.

[7] Claude Amsler. *Nuclear and Particle Physics*. 2053-2563. IOP Publishing, 2015.

[8] M J Berger and Stephen M Seltzer. *Stopping powers and ranges of electrons and positrons*. US. Nat. Bureau Stand. Inst. Basic Stand., Washington, DC, 1982.

[9] Hans A Bethe, Julius Ashkin, et al. Experimental nuclear physics. *Wiley, New York*, 1953.

[10] Brady Bos. personal communication.

[11] C. L. Cowan, F. Reines, F. B. Harrison, H. W. Kruse, and A. D. McGuire. Detection of the free neutrino: a confirmation. *Science*, 124(3212):103–104, 1956.

[12] G. Danby, J-M. Gaillard, K. Goulianos, L. M. Lederman, N. Mistry, M. Schwartz, and J. Steinberger. Observation of high-energy neutrino reactions and the existence of two kinds of neutrinos. *Phys. Rev. Lett.*, 9:36–44, Jul 1962.

[13] Matlab & Simulink Mathworks Deutschland. The inverse radon transformation.

[14] Ivan Esteban, M.C. Gonzalez-Garcia, Michele Maltoni, Thomas Schwetz, and Albert Zhou. The fate of hints: updated global analysis of three-flavor neutrino oscillations. *Journal of High Energy Physics*, 2020(9), sep 2020.

[15] K. Kodama et al. Observation of tau neutrino interactions. *Physics Letters B*, 504(3):218–224, 2001.

[16] Andrea Giuliani and Alfredo Poves. Neutrinoless double-beta decay. *Advances in High Energy Physics*, 2012:857016, Dec 2012.

[17] V. Gribov and B. Pontecorvo. Neutrino astronomy and lepton charge. *Physics Letters B*, 28(7):493–496, 1969.

[18] Gina Grünauer. personal communication.

[19] Mosaddek Hossain. *Development and evaluation of a second generation MR compatible large field of view PET insert for simultaneous small animal PET/MR studies.* PhD thesis, 2015. Tübingen, Univ., Diss., 2015.

[20] F. Hueso-González, A.K. Biegun, P. Dendooven, W. Enghardt, F. Fiedler, C. Golnik, K. Heidel, T. Kormoll, J. Petzoldt, K.E. Römer, R. Schwengner, A. Wagner, and G. Pausch. Comparison of lso and bgo block detectors for prompt gamma imaging in ion beam therapy. *Journal of Instrumentation*, 10(09):P09015, sep 2015.

[21] https://github.com/joan2937/pigpio joan2937. pigpio, Mar 2023.

[22] Markus Knapp. *Design, Simulation und Aufbau des GERDA-Myonvetos.* Dissertation, Universität Tübingen, 2009.

[23] Ettore Majorana. Teoria simmetrica dell'elettrone e del positrone. *Il Nuovo Cimento (1924-1942)*, 14(4):171–184, Apr 1937.

[24] W. Mannhart and H. Vonach. Gamma-ray absorption coefficients for nai(tl). *Nuclear Instruments and Methods*, 134(2):347–351, 1976.

[25] Chuck Melcher. Scintillation crystal for pet. *Journal of nuclear medicine : official publication, Society of Nuclear Medicine*, 41:1051–5, 07 2000.

[26] Zaheer Mohammad and Jamal Abda. Positron interactions with some human body organs using monte carlo probability method. *Iraqi Journal of Physics*, 20:50–63, 09 2022.

[27] Bhaskar Mukherjee, Yaser Gholami, Uday Bhonsle, Reinhard Hentschel, and Joseph Khachan. A unique alpha dosimetry technique using gafchromic ebt3 (r) film and feasibility study for an activity calibrator for alpha-emitting radiopharmaceuticals. *The British journal of radiology*, 88:20150035, 10 2015.

[28] Raymond L. Murray and Keith E. Holbert. Chapter 5 - radiation and materials. In Raymond L. Murray and Keith E. Holbert, editors, *Nuclear Energy (Eighth Edition)*, pages 81–99. Butterworth-Heinemann, eighth edition edition, 2020.

[29] Wolfgang Pauli. Dear radioactive ladies and gentlemen. dec 1930.

[30] Florian Ritter. *Analysis of the GERDA Muon Veto - First Light*. Dissertation, Universität Tübingen, 2011.

[31] W. Shockley. Currents to conductors induced by a moving point charge. *Journal of Applied Physics*, 9(10):635–636, 1938.

[32] Stefaan Tavernier. *Detectors Based on Scintillation*, pages 167–208. Springer Berlin Heidelberg, Berlin, Heidelberg, 2010.

[33] Wikipedia. Homestake experiment — Wikipedia, the free encyclopedia. http://en.wikipedia.org/w/index.php?title=Homestake%20experiment&oldid=1140532287, 2023. [Online; accessed 23-February-2023].

[34] Wikipedia. Massenschwächungskoeffizient — wikipedia, die freie enzyklopädie, 2023. [Online; Stand 28. März 2023].

[35] Xiaoning Zhang, Jun Qiu, Xingcan Li, Junming Zhao, and Linhua Liu. Complex refractive indices measurements of polymers in visible and near-infrared bands. *Appl. Opt.*, 59(8):2337–2344, Mar 2020.

[36] Andreas Zschocke. *Analysis and evaluation of the pulse shape performance of an Inverted Coaxial HPGe detector for $0\nu\beta\beta$ Experiments.* PhD thesis, Tubingen U., 2021.

[37] Chao Zuo, Jiaji Li, Jiasong Sun, Yao Fan, Jialin Zhang, Linpeng Lu, Runnan Zhang, Bowen Wang, Lei HUANG, and Qian Chen. Transport of intensity equation: a tutorial. *Optics and Lasers in Engineering*, 135:106187, 06 2020.